Far Infrared Linear Response and Radio Frequency Nonlinear Response of Charge Density Wave Conductors and High T_c Superconductors

By

Mark Stephen Sherwin

A.B. (Harvard University) 1981

DISSERTATION

Submitted in partial satisfaction of the requirements for the degree of

DOCTOR OF PHILOSOPHY

in

PHYSICS

in the

GRADUATE DIVISION

OF THE

UNIVERSITY OF CALIFORNIA, BERKELEY

Approved: 5/20/88
Chair Date

..... 5/17/88

..... 5/20/88

.....

FAR-INFRARED LINEAR RESPONSE AND RADIO-FREQUENCY NONLINEAR RESPONSE OF CHARGE-DENSITY-WAVE CONDUCTORS AND HIGH-T_C SUPERCONDUCTORS

Mark Stephen Sherwin

Department of Physics

University of California, Berkeley

ABSTRACT

The far-infrared linear response of the charge-density-wave (CDW) conductor $(TaSe_4)_2I$ and polycrystalline samples of the high-T_c superconductors $LaSr_{1.85}Sr_{0.15}CuO_4$ and $La_{1.85}Ca_{0.15}CuO_4$ has been measured. The frequency and temperature range of the measurements is 8-350 cm^{-1} and 5 to 300K. At low temperatures in $(TaSe_4)_2I$, a mode with giant oscillator strength was found at 38 cm^{-1}. This giant FIR mode lies between the pinned mode and the Peierls gap, where significant oscillator strength is not expected in simple models of the CDW excitation spectrum. It is suggested that a giant FIR mode distinct from the pinned mode is a common feature of CDW conductors.

At low temperatures in the high-T_c superconductors, a reflectance edge was observed near $2.5k_BT_c$. The BCS-like temperature-dependence of the reflectance edge is suggestive of an energy-gap interpretation. However, a simple model shows that a BCS-like temperature dependence is also consistent with an interpretation of the reflectance edge as a

low-frequency plasmon. It is not yet possible to deduce the magnitude of the energy gap directly from the FIR spectra of polycrystalline sample.

The radio-frequency nonlinear response of the CDW conductor $NbSe_3$ has also been measured. In the presence of combined rf- and dc- electric fields, mode-locking occurs in $NbSe_3$. Complete mode-locking in conventional samples is found to dramatically suppress sliding CDW conduction fluctuations. The application of combined rf and dc electric fields to switching samples of $NbSe_3$ is found to induce a large amplitude "ac switching noise" for rf frequencies less than 1 MHz, and a period-doubling route to chaos for rf-frequencies greater than 1 MHz. The mode-locking behavior of switching and nonswitching $NbSe_3$ is analyzed in terms of simple differential equations and discrete mappings. A model of CDW elasticity is also presented. The model qualitatively reproduces all of the experimentally-observed anomalies which occur for dc-, ac- and combined ac- and dc- electric fields. It is suggested that, during mode-locking, the number of degrees of freedom active in CDW transport is reduced.

FAR-INFRARED LINEAR RESPONSE
AND RADIO-FREQUENCY NONLINEAR RESPONSE
OF
CHARGE-DENSITY-WAVE CONDUCTORS
AND HIGH-T_C SUPERCONDUCTORS

Mark Stephen Sherwin

To the memory of my grandmother,

Terese David

Table of Contents

Acknowledgments

It is difficult to acknowledge all of those whose intellectual, material and moral support have made this thesis possible. As my thesis adviser, Professor Alex Zettl always kept me supplied with a long list of clever experiments and ingenious methods of performing them. He also encouraged me in the pursuit of my own ideas. I was especially fortunate in addition to be able to tap the vast expertise of Professor Paul Richards. The first part of this thesis would have been impossible without his encyclopedic knowledge of far-infrared spectroscopy and his well-equipped laboratory. Professor Leo Falicov has given me invaluable direction and enthusiastic support since my arrival at Berkeley. Professors Carson Jeffries and Allan Kaufman introduced me to the field of nonlinear dynamics, which has so captured my interest. I thank Professor Michael Lieberman for serving on my thesis committee.

I enjoyed the company and assistance of a number of students and post-doctoral fellows. The experiments described in Chapter 7 were performed in collaboration with Rick Hall. Rick also provided invaluable help in editing the paper on which Chapter 7 is based. Some of the experiments in Chapter 4 were performed with Dr. Ulrich Walter. Drs. Roger Tobin and Robert MacMurray struggled with me through several computer crashes in the Richards lab. Professor Andrew Lange patiently answered many questions about far-infrared spectroscopy and kindly provided some crucial filters. I thank Dr. Lincoln Bourne, Bill Creagor, Mike Crommie, Storrs Hoen, Dr. Mike Hundley, Tom Kenny, Phil Parilla, Bob Phelps, and Karel Svoboda for making the laboratory a congenial and stimulating workplace. I enjoyed many stimulating discussions with Drs. Kurt Wiesenfeld and Jeff Lerner. In the machine shop, Mr. Frank Lopez patiently crafted a beautiful apparatus from my imperfect drawings.

Without the unswerving love and support my parents have always given me, I never would have reached the beginning of my Ph. D. Without family and friends to care for me

and make me laugh through difficult times, this endeavor would have seemed (and probably been) a much longer one. I will sorely miss Fatma Isikdag and Saul Perlmutter when I leave. Fortunately, Cathy Weinberger will be with me for the next stage. I cannot imagine the last five years, or the rest of my life, without her.

The high-T_c superconductor samples used in this research were kindly provided by Professor Angelica Stacy of the University of California at Berkeley.

During the last three years, I have been generously supported by an AT&T Bell Laboratories Ph. D. Scholarship. I also gratefully acknowledge receipt of a Ross M. Tucker A.I.M.E Electronic Materials Award. The research comprising this thesis was supported in part by NSF Grants DMR 84-00041 and 83-51678, and the Director, Office of Energy Research , Office of Basic Sciences, Materials Sciences Division of the U.S. Department of Energy, under Contract No. DE-AC03-76SF00098, with additional contributions from the Alfred P. Sloan Foundation, General Motors Research Corporation, AT&T Bell Laboratories, IBM Corporation, E.I. Dupont De Nemours and Co., and the University of California Campus Committee on Research.

Vita

May 9, 1959:	Born in New York, New York
June, 1981:	M. A. in Physics, Harvard University
September, 1981 to June, 1982:	Studied Nepalese folk music on Michael C. Rockefeller Memorial Scholarship.
September, 1982 to June, 1988:	Teaching and Research Assistant, Department of Physics, University of California at Berkeley

Publications

1. R. P. Hall, M. S. Sherwin and A. Zettl, "Negative differential resistance and instability in $NbSe_3$," Phys. Rev. Lett. **52**, 2293 (1984)

2. M. Sherwin, R. Hall and A. Zettl, "Chaotic A.C. conductivity in the charge density wave state of $(TaSe_4)_2I$", Phys. Rev. Lett. **53**, 1387 (1984)

3. R. P. Hall, M. S. Sherwin and A. Zettl, "Chaotic response of $NbSe_3$: evidence for a new charge density wave phase," Phys. Rev. B. **29**, 7076 (1984)

4. R. P. Hall, M. S. Sherwin and A. Zettl, "A. C. conductivity of $K_{0.3}MoO_3$," in Charge Density Waves in Solids, Springer Verlag Lecture Note Series in Physics, v. 217, Gy. Hutiray and J. Solyom, eds. (Springer Verlag, New York, 1985), p. 314

5. A. Zettl, M. Sherwin, and R. P. Hall, "Chaos in charge density wave systems". In Charge Density Waves in Solids, Springer Verlag Lecture Note Series in Physics, v. 217, Gy. Hutiray and J. Solyom, eds. (Springer Verlag, New York, 1985) p. 333

6. A. Zettl, M. S. Sherwin and R. P. Hall, "Chaotic response of driven charge density wave systems," Mol. Liq. Cryst. **121**(1-4):49-53 (1985)

7. R. P. Hall, M. S. Sherwin and A. Zettl, "Collective mode AC conduction in the Blue Bronze $K_{0.3}MoO_3$," Sol. St. Comm. **54**(8):683-687 (1985)

8. M. S. Sherwin and A. Zettl, "Complete charge density wave mode-locking and freeze-out of fluctuations in $NbSe_3$," Phys. Rev. B **32**, 5536 (1985)

9. L. C. Bourne, M. S. Sherwin and A. Zettl, "Elastic properties of charge density wave conductors: ac-dc coupling", Phys. Rev. Lett. **56**,1952-1955 (1986)

10. M. S. Sherwin and A. Zettl, "Model of charge density wave elasticity", Physica **23D**, 155 (1986)

11. A. Zettl, M. S. Sherwin, and R. P. Hall, "Dynamics of charge density wave conductors: broken coherence, chaos and noisy precursors". Physica **143B**, 69 (1986)

12. U. Walter, M. S. Sherwin, A. Stacy, P. L. Richards and A. Zettl, "Energy gap in the high Tc superconductor $La_{1.85}Sr_{0.15}CuO_4$", Phys. Rev. B **35** , 5327 (1987)

13. M. S. Sherwin, A. Zettl and P. L. Richards, "Complete excitation spectrum for a charge density wave system", Phys. Rev. B. **36** , 6708 (1987)

14. M. S. Sherwin, P. L. Richards and A. Zettl, "Temperature dependent far infrared reflectance of La-Sr-Cu-O and La-Ca-Cu-O: Bardeen-Cooper-Schrieffer electrodynamics but uncertain energy gap", Phys. Rev. B **37**, 1587 (1988)

15. M. S. Sherwin, R. P. Hall and A. Zettl, "Switching and Charge Density Wave Transport III: Dynamical Instabilities", submitted to Phys. Rev. B

Part 1: Far infrared linear response of charge density wave conductors and high T_c superconductors

1. Introduction

In most condensed matter systems, electrical conduction can be well described by a nearly-free-electron picture. In conventional metals and semiconductors, the charge carriers are successfully modeled as weakly interacting charged fermions. However, there are certain condensed matter systems in which strong correlations between the charge-carriers cause the nearly-free-electron picture to break down completely. Two such systems are charge-density-wave (CDW) conductors and superconductors. Well-above a transition temperature T_C, both CDW conductors and superconductors are metals in which the charge is carried by relatively weakly-correlated electrons. Below T_C in CDW conductors and in conventional Bardeen-Cooper-Schrieffer[1] (BCS) superconductors, the electrons become strongly-correlated in collective-mode ground states. In the superconducting ground state, electrons with opposite spin and momentum are correlated in Cooper pairs. In the CDW ground state, electrons and holes on opposite sides of the Fermi surface are correlated to cause a static modulation of the electronic density. At low temperatures in CDW conductors and high-T_c superconductors, an energy gap occurs at the Fermi surface. Energy gaps in conventional superconductors and CDW conductors are typically in the far- and near-infrared, respectively.

For frequencies less than the energy gap, there are great differences between the low- and high-temperature excitation spectra of CDW conductors[2] and conventional superconductors. At high temperatures, free carriers contribute nonzero frequency-dependent conductivity at frequencies from dc to the free-carrier relaxation rate. At low temperatures, the free-carrier contribution to the frequency-dependent conductivity is absent for frequencies less than the energy gap. A conductivity sum rule[3] requires the integral of the frequency-dependent conductivity (the total oscillator strength) to be a constant dependent only on the number of electrons in the conduction band, and hence independent of temperature. In a BCS superconductor, the oscillator strength removed from the free

carriers is shifted to a delta function at zero frequency. In a CDW conductor, the oscillator strength removed from the free carriers is shared between discrete modes in the energy gap and an enhancement of the conductivity continuum just above the energy gap.

Part 1 of this thesis is concerned with the linear response of CDW conductors and high-T_c superconductors to weak far-infrared radiation. CDW conductors have highly anisotropic conductivities. Thus it is necessary to use polarized radiation for any measurement of the linear response function. Chapter 2 describes an apparatus developed for FIR reflectance measurements. The apparatus enables the measurement of polarized reflectance and transmittance of a sample from room temperature to 5K.

Chapter 3 describes measurements of the FIR excitation spectrum of the CDW conductor $(TaSe_4)_2I$. By combining our measurements with the measurements of other groups at lower and higher frequencies, we have for the first time completed the excitation spectrum of a CDW conductor. In the classic picture of the CDW excitation spectrum proposed by Lee, Rice and Anderson (LRA)[4], a mode corresponding to translation of the CDW center of mass relative to the lattice is expected at very low frequencies. This "pinned" mode is expected to have a large oscillator strength. In the LRA picture, only relatively weak IR-active phonons are expected between the pinned mode and the gap. We have observed at low temperatures a giant FIR mode at 38 cm^{-1}. This mode has larger oscillator strength than any other mode in the energy gap, including the pinned mode. The giant FIR mode is clearly distinct from the pinned mode observed at 1.2 cm^{-1} and the energy gap at 2000 cm^{-1}. Two possible interpretations for the FIR mode are discussed.

Chapter 4 describes attempts to measure the energy gap of polycrystalline samples of the high-T_C superconductors $La_{1.85}Sr_{0.15}CuO_4$ and $La_{1.85}Ca_{1.85}CuO_4$. At low temperatures, a reflectance edge was observed at 60 cm^{-1}. The temperature-dependence of this edge fits the temperature dependence of the BCS gap. We and other groups initially interpreted the edge as an energy gap. However, an alternative interpretation[5] suggests that the reflectance edge is caused by a low-frequency plasmon. A simple model is solved in

Chapter 4, and the temperature-dependence of the reflectance edge is found to be consistent with the plasmon interpretation. We conclude that the magnitude of the energy gap cannot yet be deduced directly from the FIR spectra of polycrystalline samples.

Part 2 of this thesis is concerned with the nonlinear response of CDW conductors to combined strong radio-frequency and dc electric fields. An introduction to relevant experimental results and theoretical models is to be found in Chapter 5. Superconductors are not discussed in Part 2.

References

[1] J. Bardeen, L. N. Cooper and J. R. Schrieffer, Phys. Rev. **106**, 162 (1957)

[2] For a review of the excitation spectra of CDW conductors, see for example A. J. Berlinsky, Rep. Prog. Phys. **42**, 1243 (1979)

[3] R. A. Ferrell and R. E. Glover, III, Phys. Rev. **109**, 1398 (1958); M. Tinkham and R. A. Ferrell, Phys. Rev. Lett. **2**, 331 (1959)

[4] P. A. Lee, T. M. Rice and P. W. Anderson, Solid State Commun. 14,703 (1974)

[5] D. A. Bonn, J. E. Greedan, C. V. Stager, T Timusk, M. G. Doss, S. L. Herr, K. Kamaras, C. D. Porter, D. B. Tanner, J. M. Tarascon, W. R. McKinnon and L. H. Greene, Phys. Rev. B **36**,

2. Far infrared equipment

At far-infrared (FIR) frequencies, it is not possible to directly measure the dielectric response function of a material. The reflectance, transmittance or absorption must be measured. The dielectric response function is then deduced using linear response theory. Since CDW conductors have highly anisotropic conductivity, it is necessary to use polarized radiation in order to deduce their dielectric properties. This chapter describes the apparatus used to measure the polarized reflectance of the charge-density-wave conductor $(TaSe_4)_2I$ and the high-T_c superconductors $La_{1.85}(Sr)_{0.15}CuO_4$ and $La_{1.85}Ca_{0.15}CuO_4$. In section 2.1, the problems associated with polarizing radiation in light pipe optics are discussed. In section 2.2, a transmittance-reflectance apparatus ("the T-R apparatus") is described. Using the T-R apparatus, the polarized reflectance or transmittance of a sample may be measured as a function of temperature from 5K to 300K. In section 2.3, configurations of the spectrometer and detector that are useful with the T-R apparatus are discussed.

2.1. Polarization in light pipe optics

The polarizers used in these experiments are made of a grid of finely-spaced parallel wires. Radiation polarized (parallel/perpendicular) to the wires is (reflected/transmitted). An ideal polarized transmittance experiment is shown in Fig. 2-1a. Unpolarized radiation is polarized by the first wire grid polarizer. The polarized radiation impinges on a second polarizer that fills the entire beam. The transmitted radiation is then detected. Multiple reflections between the sample and polarizer do not occur in an ideal experiment. When the polarizers are crossed, as in Fig. 2-1a, all the radiation reaching the second polarizer is reflected back and transmitted away from the detector by the first polarizer. No radiation reaches the detector.

Far-infrared radiation is typically guided by light-pipe optics. If care is not taken, a polarized transmittance or reflectance experiment in a light-pipe optical system will be far

from ideal. Consider the transmittance experiment shown in Fig. 2-1b. In this case, the second polarizer fills only about 10% of the area of the light pipe. The path of a typical ray is shown inside the light pipe. After being polarized by the first polarizer, the ray may bounce off the light pipe wall, possibly suffering a change of polarization.(In the f/1.5 optics used for my experiments, a typical ray will bounce off the walls of the 1-cm light pipe once every few centimeters.) On reaching the second polarizer oriented perpendicular to the first one, part of the depolarized ray will be transmitted and reach the detector. The remainder will bounce around in the cavity formed by the two polarizers, causing yet more radiation to reach the detector. The problem may be exacerbated by the highly reflective metal used to block the light pipe. However, some radiation would reach the detector even if the second polarizer filled the light pipe.

Fig. 2-2 shows experimental data for a configuration like that in Fig. 2-b. The transmitted intensity in the 50-300 cm^{-1} band for crossed and parallel polarizers is plotted as a function of the distance d between polarizers. For $d \approx 0$ (polarizers touching), the crossed polarizer configuration transmits less than 10% as much as the parallel polarizer configuration. However, the transmittance in the (crossed,parallel) polarizer configuration (increases,decreases) rapidly as the distance d is increased. For a separation of only 2 cm (only twice the diameter of the light pipe), the polarization state of the radiation is already uselessly scrambled.

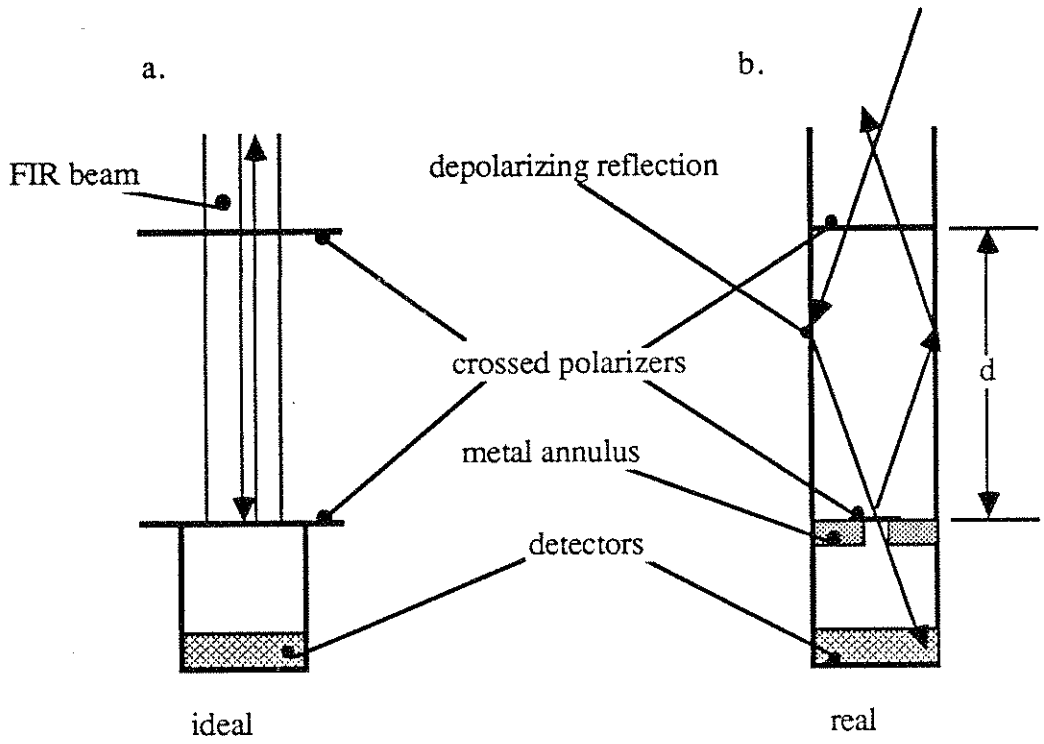

Fig. 2-1: (a) Ideal transmission experiment through crossed polarizers. The arrows represent light rays. The second polarizer reflects all rays. The reflected rays are perfectly transmitted away from the detector by the first polarizer. No radiation reaches the detector.
(b) Light pipe transmission experiment through crossed wire grid polarizers. The distance between polarizers is d. If d is large enough, a typical ray reflects off the walls of the light pipe between the two polarizers. The reflection changes the polarization state of certain rays. Thus, even for crossed polarizers, some radiation will reach the detector.

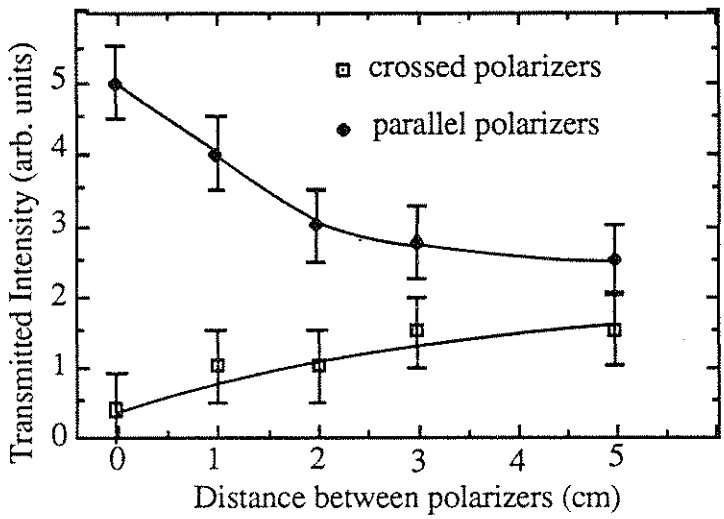

Fig. 2-2: Intensity of radiation reaching a pyroelectric detector vs. distance d between crossed and parallel polarizers. The experimental configuration was like that in Fig. 2-1b. The inner diameter of the circular polished brass light pipe was 1 cm. The wire-grid polarizers were manufactured for the Richards group by Hughes Corporation. Even for d=2 cm , the polarization was severely degraded.

2.2. The Transmittance-Reflectance Apparatus

2.2.1. Optics

The polarization problem for a light-pipe transmittance experiment is easily solved by minimizing the distance between the sample and polarizer. However, the same solution is not viable in a reflectance experiment. If the polarizer is directly on top of the sample, then the reflected radiation reaching the detector will have a large (>50%) background component due to the reflectance off the polarizer itself.

A solution to the polarization problem for reflectance is shown in the diagram of the T-R apparatus, Fig. 2-3. The polarizer is placed about 1 cm above the sample. A septum prevents light reflected off the polarizer from reaching the detector. Between the polarizer and the sample, the walls of the light pipe have been cut away. Light baffles in the space between the bottom of the light pipe and the sample prevent stray reflections from the T-R apparatus chamber from reaching the detector. The light baffles are made of three layers of molded black Stycast epoxy #2850 FT (a good FIR absorber). The light reaching the sample is >96% polarized in this apparatus[1]. The costs of the high degree of polarization are threefold: a large amount of radiation is lost in the light baffles, the sample is inhomogeneously illuminated, and light scattered to large angles by surface roughness is lost in the light baffles rather than being collected by the light pipe.

2.2.2 Cryogenics

The T-R apparatus is built around an evacuated Air Products LT 3-110 continuous flow Helium cryostat. Samples are placed on a three-position sample slide. Cold samples may be moved in- and out- of the FIR beam by a shaft connected through a vacuum seal to the outside world. To minimize the heat leak from room temperature, the shaft may be disconnected from the sample slide once the slide is in the desired position. The sample slide is thermally connected by a Copper braid directly to the coldfinger of the cryostat. The sample temperature is measured by a calibrated diode placed directly on the sample

slide[2]. Because of large thermal time constants, it is necessary to control temperature from a second diode. The temperature-control diode is in a hole drilled through the coldfinger, and adjacent to a heater. Temperature may be controlled by a standard proportional temperature controller. Sample temperatures as low as 5K have been measured in the T-R apparatus. Lower temperatures should be achievable by pumping on the Helium transferred to the coldfinger.

2.3. Spectrometer and detectors

The source of radiation for FIR experiments in the Richards lab is a step-and-integrate Michelson Fourier spectrometer[3]. The wavelength range covered in a given experiment is determined by choice of an appropriate beam-splitter. Each beam splitter covers a roughly a factor of four in frequency. The measurements reported here are between 4 cm^{-1} and 350 cm^{-1}.

The detector is a composite bolometer cooled[4] to about 1.5K by a pumped Helium bath. The radiation load on the bolometer is in all cases dominated by room-temperature black-body radiation. Cold low-pass filters are typically placed in front of the bolometer to enhance bolometer sensitivity by limiting room-temperature radiation loading. For minimum bolometer loading, a different low-pass filter is required for each beam-splitter. In a previously built detector cryostat, six filters were arranged on a wheel immersed in the Helium bath directly above the bolometer. Using this cryostat with judiciously chosen filters in conjuction with the T-R apparatus allows maximum flexibility. Without warming up either the sample or the detector, different frequency ranges may be covered by simply changing the beam splitter in the Michelson interferometer and rotating in the appropriate filter on the cold filter wheel. (The trick is to get the Michelson Fourier spectrometer, the detector and the T-R apparatus all working at the same time). Table 2-1 lists the filters used in my experiments.

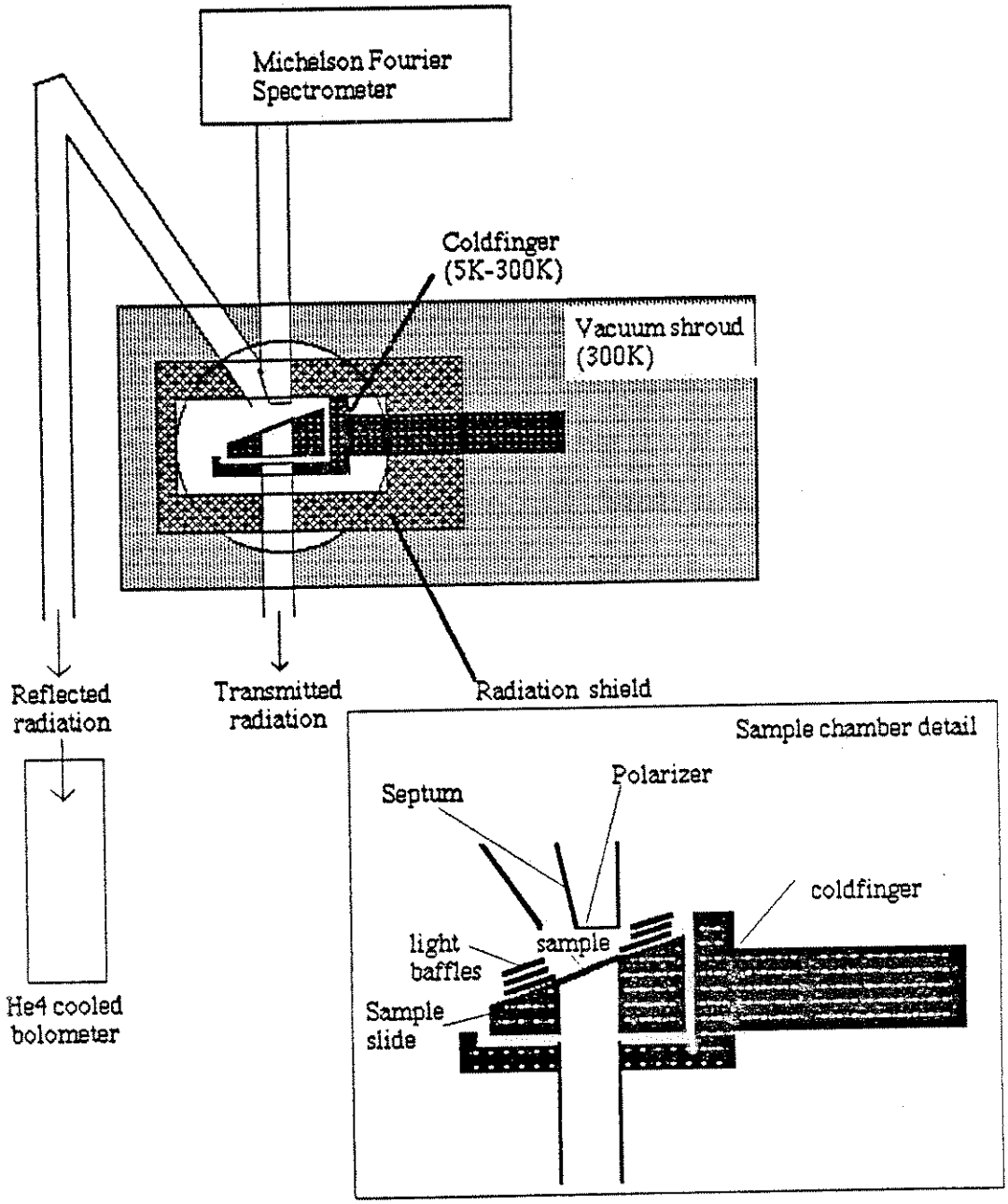

Fig. 2-3: Schematic diagram of the transmittance-reflectance apparatus. With this apparatus, polarized reflectance and transmittance of a sample may be measured as a function of temperature from 5K to 300K.

Filter	Cut-off frequency	Beam splitter
Glass bead†	25 cm^{-1}	5, 10 mil
Perkin-Elmer 1049	60 cm^{-1}	2 mil
Perkin-Elmer 1048	100 cm^{-1}	1 mil
Z-cut quartz (wedged)	250 cm^{-1}	0.5 mil
Black polyethylene	400 cm^{-1}	0.25 mil

Table 2-1: Low-pass filters mounted in the cold filter wheel above the bolometer, approximate cut-off frequencies and appropriate beam splitters. All filters were backed with black polyethylene to avoid any radiation leakage at frequencies >400 cm^{-1}.

The bolometer that I used was optimized for relatively low backgrounds. In order to avoid overloading the bolometer in high backgrounds, it was necessary to stop down the beam with cold apertures for the Z-cut quartz and black polyethylene filters. This explains the relatively poor signal-to-noise ratio in spectra recorded above 250 cm^{-1}.

† Glass beads embedded in a clear polyethylene matrix. This filter was kindly supplied by Prof. Andrew Lange.

References

1 Polarization: The most sensitive test of the degree of polarization achieved by the T-R rig was to measure the reflectance of the highly anisotropic conductor $(TaSe_4)_2I$. For light polarized parallel to the c-axis, a sharp reflectance edge occurs at low temperatures. The reflectance drops from near 100% at 96 cm^{-1} to 20% at 100 cm^{-1}. For light polarized perpendicular to the c-axis, no feature near 100 cm^{-1} could be distinguished from the ≈2% experimental noise.

2 Heat sinking of electrical leads: Between room temperature and the coldfinger, all electrical leads are cooled by wrapping them around the coldfinger stem. The leads to the temperature measurement diode are thermally anchored to copper pads epoxied to the sample slide with Stycast.

3 For an introduction to Fourier Transform Infrared Spectroscopy, see R. J. Bell, *Introductory Fourier Transform Spectroscopy* (Academic Press, New York, 1972)

4 A. E. Lange, E. Kreysa, S. E. McBride and Paul L. Richards, International Journal of Infrared and Millimeter Waves **4**, 689 (1979)

3. Far infrared spectroscopy of (TaSe4)2I

3.1. Introduction

Over the past 15 years, far-infrared (FIR) spectroscopy has been an invaluable tool for the study of quasi-one dimensional materials that undergo a Peierls transition to the charge density wave (CDW) state [1,2,3,4]. Based on the theory of Lee, Rice and Anderson(LRA)[5], one expects a large IR-active response due to the pinned mode of the CDW at frequencies low compared to ordinary phonons and electronic excitations. Large oscillator strength has been found in both the FIR [1-4] and microwave [6,7,8] frequency ranges in several CDW systems. In both frequency ranges, part of this oscillator strength has been attributed to the pinned mode of the CDW. Unfortunately, FIR and microwave measurements reported to date have not provided a complete and consistent dielectric function in the millimeter and submillimeter wave region, and it is not yet clear whether the FIR and microwave modes are distinct. In this chapter, we present FIR data that unambiguously shows that, in the CDW material $(TaSe_4)_2I$, the microwave and FIR modes are distinct. Therefore, the assignment of giant FIR modes observed in other CDW materials to the pinned mode must be re-examined.

3.2. Experimental methods

We have measured the polarized reflectance of $(TaSe_4)_2I$ for frequencies from 8 to 350 cm^{-1} and temperatures from 10K to 290K. The $(TaSe_4)_2I$ unit cell has tetragonal symmetry, and hence there are two principal optical axes. The sample used for the reflectance measurements was a mosaic of several single crystals carefully oriented along both principal axes[9]. The crystals were grown in our laboratory and had large faces that were typically 2mm by 5 mm. The sample was placed in a continuous transfer Helium cryostat adapted in our laboratory for use with a Michelson Fourier spectrometer to measure polarized reflectance. Radiation was detected using a low noise composite bolometer operated at 1.5K. At each fixed sample temperature, the sample spectrum was

divided by the spectrum of a polished brass surface. The details of the experimental apparatus have been described in Chapter 2.

After all data had been measured, gold was evaporated onto (only) the crystal faces of the mosaic. The reflectance was measured after each of several gold evaporations and normalized to the brass surface. The reflectance after each of the last two evaporations was identical, indicating that sufficient gold had been deposited. From 4 to 15 cm^{-1}, the reflectance of the gold-evaporated sample decreased with increasing frequency. Between 15 and 150 cm^{-1}, the reflectance of the gold-evaporated sample was independent of frequency. To properly normalize the temperature-dependent reflectance spectra of $(TaSe_4)_2I$ for frequencies below 15 cm^{-1}, these spectra were divided by the spectrum of the gold-evaporated sample. Above 15 cm^{-1}, spectra were simply divided by the average value of the frequency-independent portion (between 15 and 150 cm^{-1}) of the reflectance of the gold-evaporated sample.

3.3. Experimental Results

Fig. 3-1 presents reflectance curves for $(TaSe_4)_2I$ at various temperatures for radiation polarized parallel to the c-axis. At room temperature the reflectance is high and fairly featureless except for a slow decrease with increasing frequency from 0.9 at 30 cm^{-1} to 0.7 at 300 cm^{-1}. As the sample is cooled through the Peierls transition temperature T_P=265 K, the reflectance between 30 and 90 cm^{-1} begins to increase, and the decrease in the reflectance near 100 cm^{-1} begins to sharpen. These changes signal the onset of an IR active mode associated with the CDW. As the sample is cooled further, the decrease in reflectance develops into an extremely sharp edge, with the reflectance at 110K dropping from near unity at 92 cm^{-1} to 0.2 at 96 cm^{-1}. The reflectance changes little between 110K and 10 K. Fig. 2 (solid line) shows the measured reflectance at 10K. The reflectance rises from 0.9 at low frequencies to near unity at 40 cm^{-1} and remains near unity until 94 cm^{-1}, with the exception of a small dip at 79 cm^{-1}. At frequencies beyond the reflectance edge,

two sharp features are evident, at 143 and 190 cm^{-1}. Between 200 cm^{-1} and 350 cm^{-1} the reflectance slowly rises with no additional sharp features and then levels off at a value of 0.58±0.02, consistent with higher frequency measurements[10].

Fig. 3-3 presents the reflectance of $(TaSe_4)_2I$ at room temperature and at 10K for the electric field polarized perpendicular to the c-axis. Whereas the parallel reflectance looks metallic at room temperature (high reflectance, all phonons screened by free carriers), the perpendicular spectrum looks more like that of a semiconductor (low reflectance, phonons visible at room temperature). The perpendicular reflectance shares no common features with the parallel reflectance described above. At room temperature, the reflectance decreases from 0.44 at 8 cm^{-1} to 0.40 at 40 cm^{-1}. There is a small bump centered at 47 cm^{-1}, and a larger one centered at 71 cm^{-1}. Above 80 cm^{-1} the reflectance drops to roughly 0.25. There is another bump at 118 cm^{-1}. Above 120 cm^{-1}, the reflectance decreases gradually to 0.2±0.02 at 300 cm^{-1}. At 10K, the reflectance looks similar to the room temperature reflectance. The reflectance at 8 cm^{-1} is lower at 10K (0.38±0.02 at 9 cm^{-1}) than at room temperature (0.44 ± 0.02 at 9 cm^{-1}). This is probably because the all of the free carriers present at room temperature have been frozen out at low temperatures. The bumps at 47, 71 and 118 cm^{-1} have all sharpened into features with the characteristic shape of weakly damped phonons. Additional small features are now visible at 64 and 79 cm^{-1}.

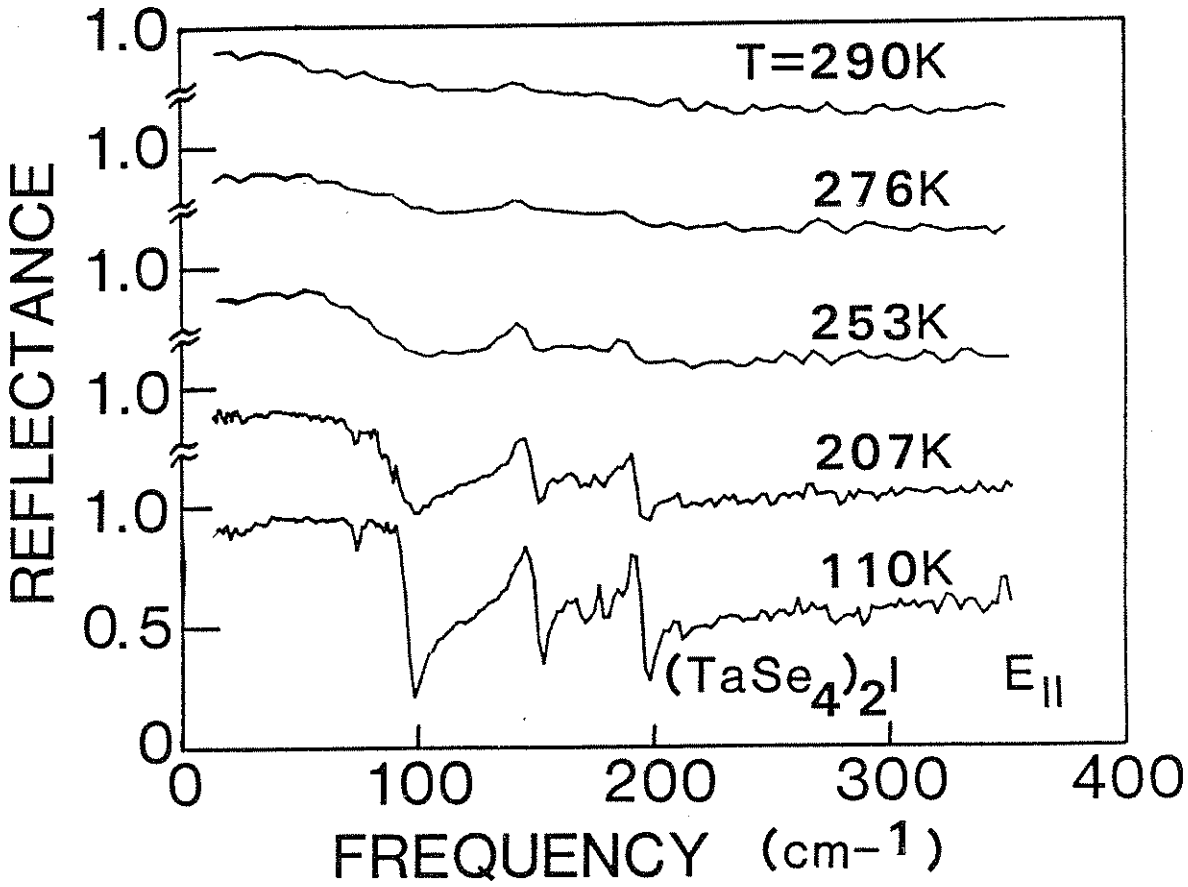

Fig. 3-1: FIR reflectance of $(TaSe_4)_2I$ for electric field polarized parallel to the highly-conducting c-axis at selected temperatures.

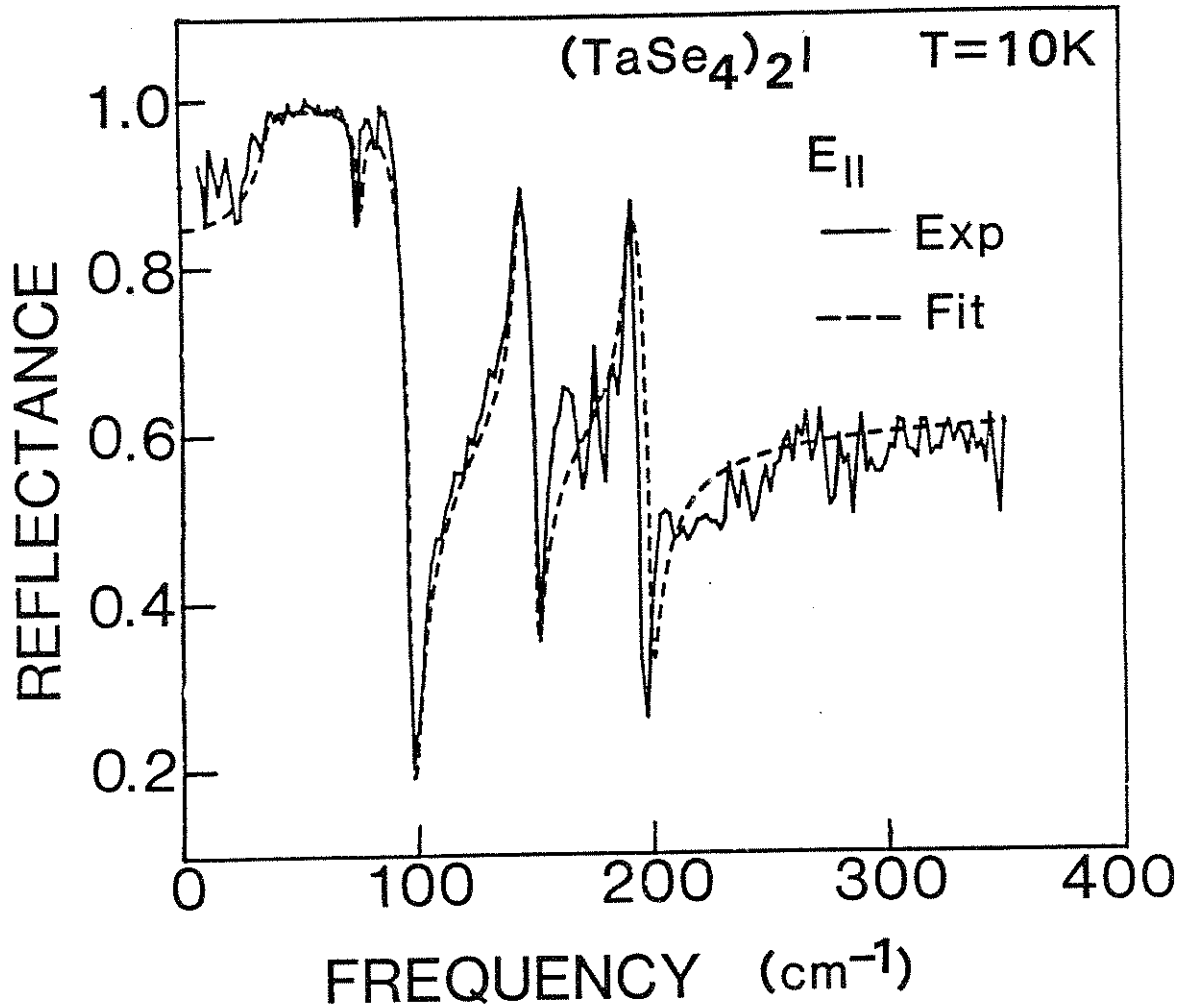

Fig. 3-2: FIR reflectance of $(TaSe_4)_2I$ at 10 K for electric field polarized parallel to c-axis (solid line) and oscillator fit (dashed line) calculated from the parameters of Table 3-1.

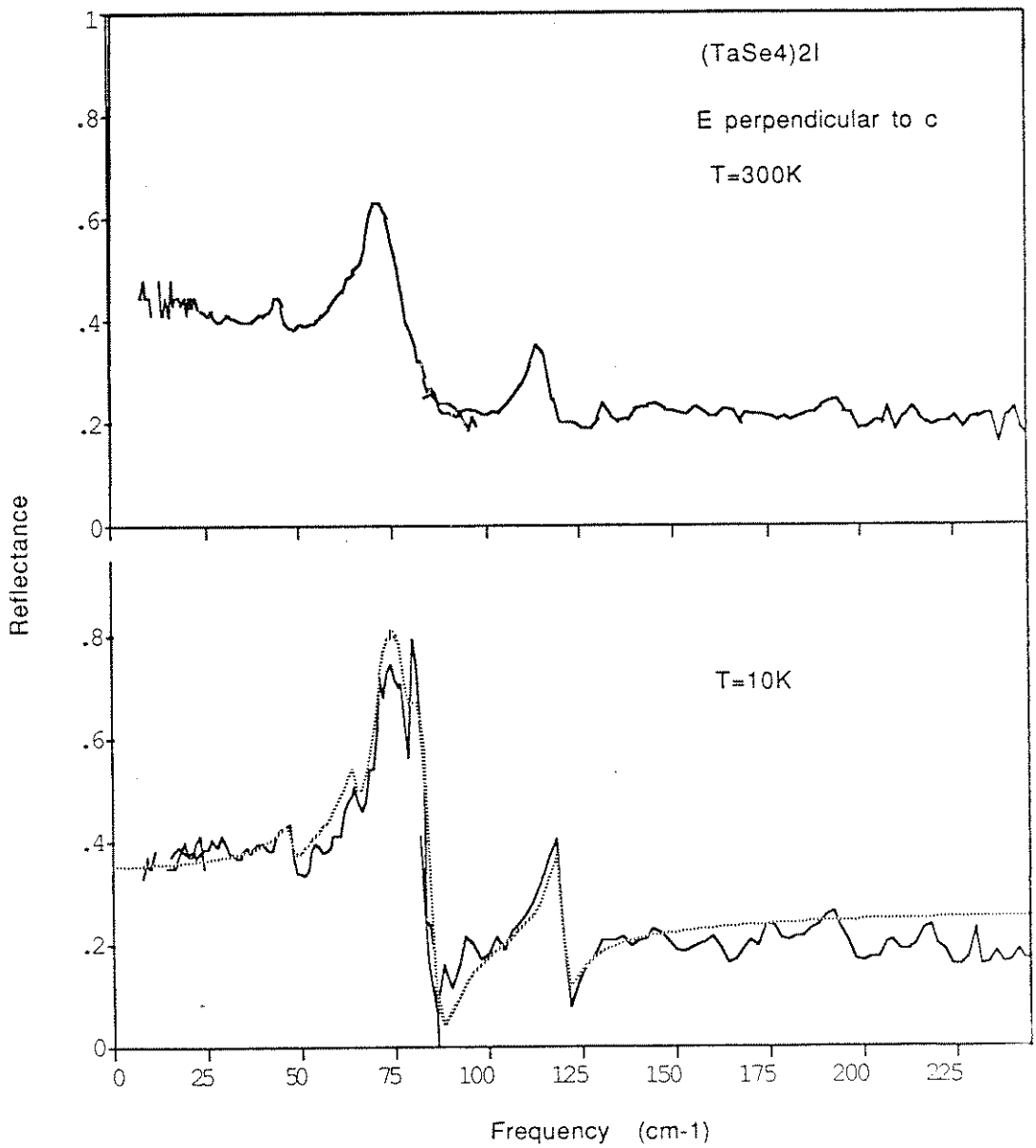

Fig. 3-3: FIR reflectance of $(TaSe_4)_2I$ at room temperature and 10K for electric field polarized perpendicular to the highly-conducting c-axis (solid lines) and oscillator fit to the 10K reflectance (dashed line).

3.4. Oscillator fits

In order to extract the complex dielectric function $\varepsilon=\varepsilon_1+i\varepsilon_2$ from the reflectance data, we have fitted the perpendicular and parallel reflectances to standard oscillator models. The dielectric function is represented as sum a of Lorentz oscillators and a background dielectric constant ε_∞:

$$\varepsilon_1(f) = \varepsilon_\infty + \sum_n S_n \frac{1-(\frac{f}{f_{Tn}})^2}{(1-(\frac{f}{f_{Tn}})^2)^2 + \frac{f^2}{f_{Tn}^4\tau_n^2}} \qquad (3\text{-}1)$$

$$\varepsilon_2(f) = \sum_n S_n \frac{\frac{f}{f_{Tn}^2\tau_n}}{(1-(\frac{f}{f_{Tn}})^2)^2 + \frac{f^2}{f_{Tn}^4\tau_n^2}} \qquad (3\text{-}2)$$

where the TO frequency, static polarizability, and damping time of the nth mode are respectively f_{Tn}, S_n, and τ_n. The oscillator strength $\Omega_p^2 = (2\pi f_{Tn})^2 S$ is related to the fundamental parameters of a mode by the formula

$$\Omega_p^2 = \frac{4\pi n e^{*2}}{m^*} \qquad (3\text{-}3)$$

where n is the density of oscillators, e* is the charge on the mode and m* is the mode mass.

The pattern of a rise in the parallel-polarized reflectance from 0.9 at 20 cm^{-1} to near unity above 40 cm^{-1} followed by a reflectance edge suggests the presence of a mode with a giant oscillator strength[11] in the region between 25 and 50 cm^{-1}. The other peaks in the spectrum (for example at 143 and 190 cm^{-1}) indicate modes with much smaller oscillator strength. The dashed line in Fig. 3-2 shows the fit to the reflectance computed from a

model dielectric function. This dielectric function is dominated by a mode with f_T=38 cm^{-1}, $f_T\tau$=13 and S=500. Changes in the parameters of the 38 cm^{-1} mode of only 5% visibly degrade the quality of the fit. Three other modes with f_T = 79, 149 and 194 cm^{-1} have been added to model smaller features. Table 3-1 lists all the parameters used in the oscillator fit. Our fit is not at all sensitive to the existence of a mode with $S=10^4$ at 35 GHz, as observed using microwave techniques[7]. This proves that our data are consistent with lower frequency measurements.

Fig. 3-4 shows ε_1 and ε_2 calculated from Eqs. 1 and 2 using the fitted parameters. Peaks in ε_2 (and hence the conductivity) occur at each of the mode frequencies, the largest being at 38 cm^{-1}. At frequencies much less than the 38 cm^{-1} resonance peak, ε_1 of Fig. 3-4 is approximately equal to 600, which is consistent with the high reflectance at low FIR frequencies. Between 38 and 100 cm^{-1}, the dielectric function is negative, giving rise to the near unit reflectance over this frequency range. The small dip at 79 cm^{-1} results from a weak mode at that frequency. At 100 cm^{-1}, the dielectric function crosses the real axis, leading to the sharp reflectance edge observed in Fig. 3-2.

The dashed line in the lower trace of Fig. 3-3 is an oscillator fit to the perpendicular reflectance. The parameters of the fit are listed in Table 3-1. The most prominent feature in the perpendicular spectrum is fit by an oscillator with S=3.8 and f_T = 71 cm^{-1}. All other features have S≤1. The total FIR oscillator strength in the perpendicular spectrum is at low temperatures at least 30 times smaller than the FIR oscillator strength in the parallel spectrum. The low oscillator strength perpendicular to the c-axis is consistent with the highly one-dimensional band structure of this material.

Table 3-1: Parameters used in the oscillator fits

TO frequency f_T (cm^{-1})	Static polarizability S	Dimensionless lifetime $f_T\tau$
a) E parallel to c		
38	500	13
79	1.5	25
149	2.5	50
194	4	50
b) E perpendicular to c		
47	.5	14
64	1	19
71	3.8	21
79	.1	24
118	.3	35

Table 3-1: Parameters of the oscillator fits to the parallel and perpendicular reflectance. For the parallel and perpendicular fits, ε_∞ is respectively 75 and 9.7. For comparison, the optic mode in CsI has $f_T = 65\ cm^{-1}$ and S=4.

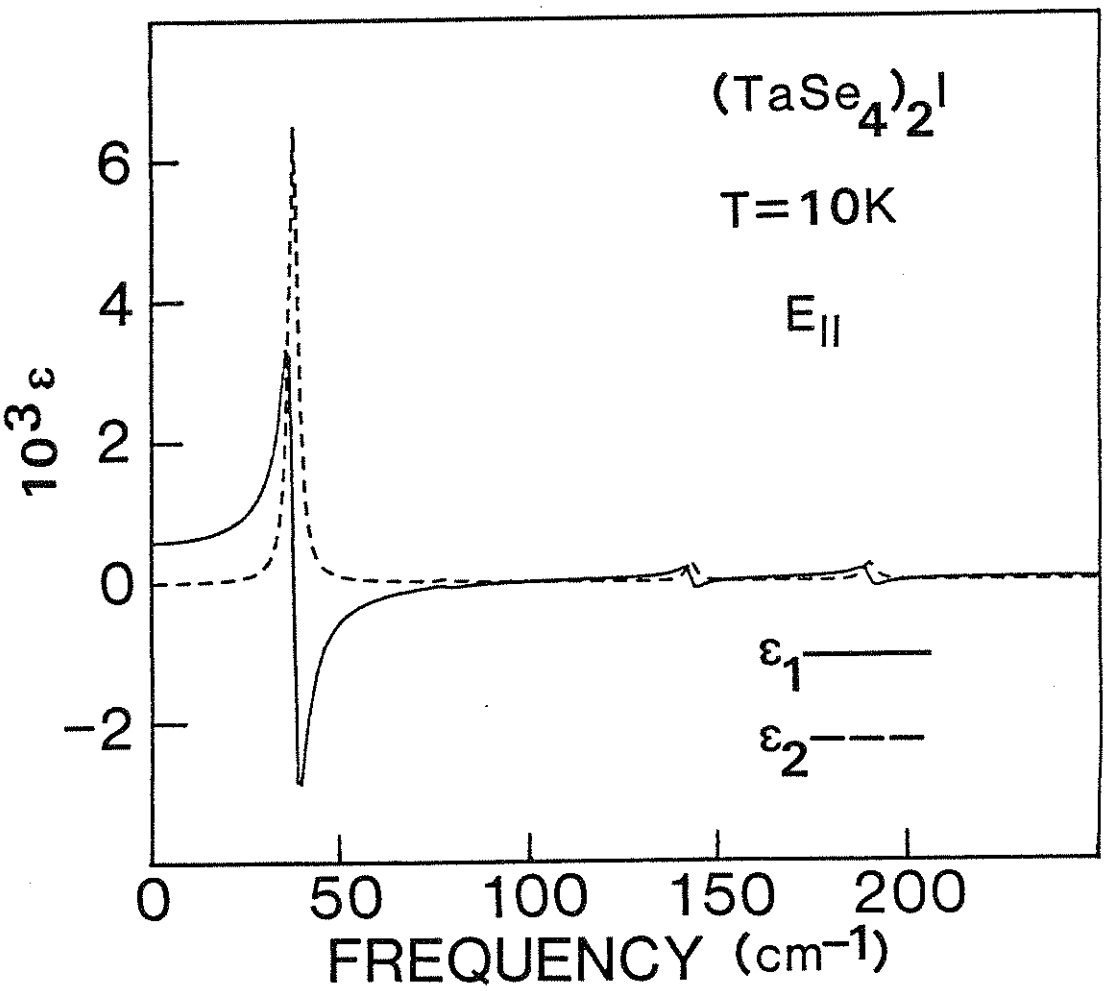

Fig. 3-4: Real and imaginary parts of the dielectric function ε_1 and ε_2 for $(TaSe_4)_2I$ at 10K, as determined by the oscillator fit to the reflectivity. Both ε_1 and ε_2 are flat and featureless between 250 and 400 cm^{-1}.

3.5. Analysis: a new picture of the CDW excitation spectrum

Our measurement of the parallel polarized FIR spectrum of $(TaSe_4)_2I$ completes the excitation spectrum for this material, and for the first time we have a complete and consistent dielectric response function from dc to the Peierls gap of a sliding CDW compound. The contributions to the dielectric function in the CDW state are as follows. A broad peak with a temperature dependent frequency[12] appears below 1MHz and has been associated with dielectric relaxation of the CDW. A large, underdamped resonance[7] at 35 GHz=1.2 cm^{-1} has been convincingly attributed to the pinned mode of the CDW. At 38 cm^{-1} we have observed the giant FIR resonance described above. The 38-cm^{-1} resonance has 80 times the oscillator strength of the 1.2-cm^{-1} resonance. From 78 to 194 cm^{-1} we observe a number of weaker resonances. Finally, the Peierls gap has been observed[9,13] near 2000 cm^{-1}. Table 1 is a summary of the principal features of the dielectric functions of $(TaSe_4)_2I$, $K_{0.3}MoO_3$, and $NbSe_3$.

A giant FIR resonance[1,3] at 15 cm^{-1}, similar to that in $(TaSe_4)_2I$, has been reported in $K_{0.3}MoO_3$. The FIR resonance was originally assigned to the pinned mode[1]. However, the presence of a distinct mode near 3 cm^{-1} was later deduced[3] by combining 40 K microwave[8] and 2K FIR data[3]. The assignment of the 3 cm^{-1} mode to the pinned mode[3] is consistent with assignments for the microwave modes in other CDW materials[6,7].

In $NbSe_3$, the pinned mode appears at microwave frequencies[6] as an extremely overdamped mode with width 60 GHz. A large temperature dependent reflectance edge[2] similar to that in Fig. 1 has also been observed at 140 cm^{-1} and has been interpreted as arising from a combination of free carriers and the pinned mode. However, the parameters for the pinned mode extracted under this interpretation are inconsistent with the microwave data. A possibility that should be investigated is that the 140 cm^{-1} edge arises from a combination of free carriers and a giant FIR mode.

Table 3-2

	Radio Frequency: [a] Dielectric relaxation (MHz)	Microwave: [b] Pinned phason (GHz)	Far Infrared: [c] Kohn Anomaly mode? (cm^{-1})	Near Infrared:[d] Peierls gap (cm^{-1})
$(TaSe_4)_2I$	0.2	35	38	2000
$K_{0.3}MoO_3$	0.7	84	15	1200
$NbSe_3$	19	4.3	<140?	560

Table 3-2: Dielectric response of CDWs for frequencies up to the Peierls gap.

[a] Ref. 11

[b] $(TaSe_4)_2I$: Ref. 7; $NbSe_3$: Ref. 6; $K_{0.3}MoO_3$: Ref. 3

[c] $K_{0.3}MoO_3$: Refs. 1 and 3; $NbSe_3$: Ref. 2.

[d] $(TaSe_4)_2I$: Ref. 10; $K_{0.3}MoO_3$: Ref. 1; $NbSe_3$: Tunneling measurement of A. Fournel, J. P. Sorbier, M. Konczykowski, and P. Monceau, Phys. Rev. Lett. **57**, 2199 (1986). Ref. 2 reports a value of 190 cm^{-1}.

A giant Kohn anomaly drives the Peierls transition in CDW materials[14]. In the simplest picture, an acoustic phonon with wavevector $q=2k_F$ softens as the Peierls transition temperature is approached from above. The phonon frequency goes to zero at the transition temperature, and the static CDW distortion of the electrons and lattice sets in. In the seminal work on the excitation spectrum of the CDW state, Lee, Rice and Anderson[5] predicted two branches of excitations for a CDW: an acoustic or phason branch consisting of excitations of the phase of the CDW, and an optical or amplitudon branch consisting of excitations of the CDW amplitude. In the theory of LRA, the zero-wavevector phason is totally antisymmetric and hence only IR-active, while the zero-wavevector amplitudon is totally symmetric and hence only Raman-active. The presence of two IR-active modes of the CDW with large oscillator strength in $(TaSe_4)_2I$ requires a modification of this standard picture. We discuss two possibilities.

A second IR active mode that is generic to all CDW systems is the optical phason, also called by Walker[15] the first harmonic phason. The optical phason may be simply understood if one draws a parallel between the modulated electronic density in a CDW and the more familiar case of alternating positive and negative ions in an ionic crystal like NaCl. The peaks and troughs in the modulated electronic density are mapped onto the Na and Cl ions. In this analogy, the q=0 acoustic phason corresponds to translations of the entire NaCl crystal, the amplitudon would correspond to a mode in which charge is transferred between Na and Cl ions, and the optical phason would correspond to the familiar IR active optic mode of NaCl. In the same way one would calculate the frequency of the zone center optic phonon mode in a 1-d diatomic crystal with nearest neighbor interactions, one can estimate the frequency of the optical phason from the slope of the dispersion relation and the CDW wavevector $2k_F$. The slope of the acoustic phason branch is given by LRA as $v_{ph}=\sqrt{(m_b/m_{Fr})}v_F$, where m_b is the band mass, m_{Fr} the Frohlich mass, and v_F the Fermi velocity. We assume m_b=free electron mass, $m^*/m_c=10^4$ from microwave measurements[7],

$v_F=hk_F/m$, and $2k_F=2\pi/14$Å from x-ray measurements[16]. The calculated frequency of the optical phason is then $(2/\pi)(2k_Fv_{ph}/2\pi)=39$ cm^{-1}, remarkably close to the 38 cm^{-1} resonant frequency derived from our measurements.

Unfortunately, the optical phason is not expected to have a very large oscillator strength. The amplitude of the charge modulation at low temperatures in $(TaSe_4)_2I$ is about 5%. Returning to the NaCl analogy, the optical phason corresponds to a lattice with each ion containing 5% of the charge in the unit cell. We find that, in order for the optical phason explanation to be correct, the effective mass of the 38 cm^{-1} mode[17] would have to be an unreasonably small $m^*=0.5m_e$. Since the 38 cm^{-1} mode is a coupled electron-lattice mode, its effective mass should be between the electronic and ionic masses.

Sugai et. al.[18] have suggested that the simplest picture of the Peierls transition is not valid in $(TaSe_4)_2I$. Fig. 3-5 (from Ref. 18) is a schematic diagram of the electronic and TA phonon dispersion relations for $(TaSe_4)_2I$. The conduction band in $(TaSe_4)_2I$ is nearly filled, so k_F is near the edge of the first Brillouin zone. The giant Kohn anomaly at $2k_F$ is in the second Brillouin zone. In the extended zone scheme, it is an optic mode at $2k_F$ which begins to soften well above the transition temperature T_P. In the reduced zone scheme, this optic mode (which I will call the Kohn anomaly mode) has wave-vector $2\pi/a-2k_F$, where a is the lattice constant of $(TaSe_4)_2I$. As the Kohn anomaly mode softens, its frequency must approach the frequency of the acoustic mode at $2\pi/a-2k_F$. When the acoustic and optic modes at $2\pi/a-2k_F$ are sufficiently close in frequency, they hybridize and repel one another. The mode that is finally driven to zero frequency to form the static CDW is not the Kohn anomaly mode, but a hybrid mode mostly derived from the acoustic mode at $2\pi/a-2k_F$. The optical phason is $2k_F$ away from point a, at the points labeled "op" in the reduced and extended zone drawings.

In the Sugai et. al. picture, unlike the standard LRA picture, the Kohn anomaly mode is not the lowest lying IR-active mode. The Sugai et. al. picture is supported by their Raman data. They have observed a very strong, temperature-dependent Raman mode with

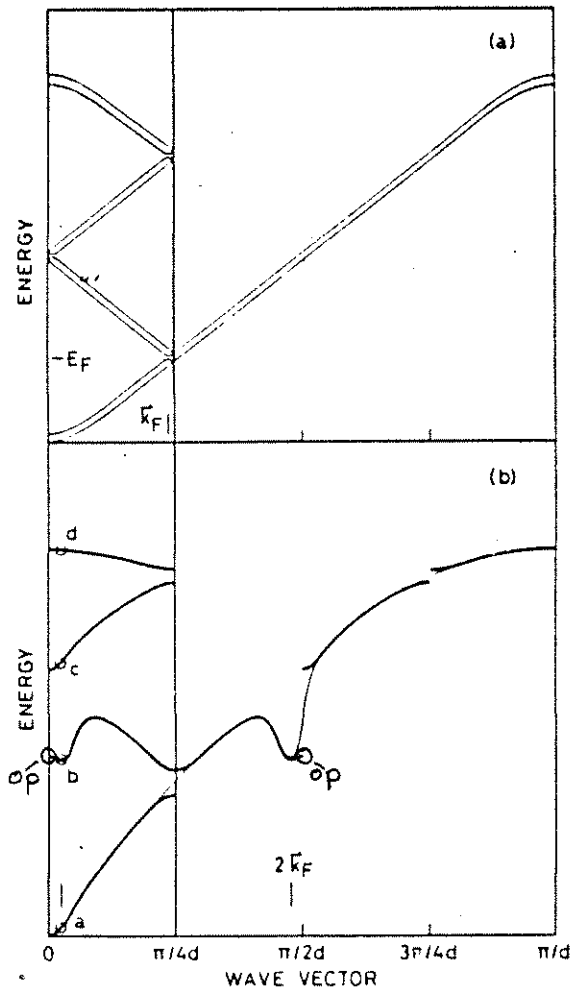

Fig. 3-5: Schematic dispersion relation of the conduction band (a) and the TA phonon branch (b). A fourfold periodicity in the Ta-Ta distance above T = T_P causes the edge of the Brillouin zone to be at $\pi/4d$ above $T=T_p$, where d is the mean Ta-Ta distance. The Fermi wave-vector is nearly at the edge of the Brillouin zone. In the CDW state, antisymmetric IR-active CDW phase modes and Raman-active CDW amplitude modes occur at points a,b,c and d at wavevector $q=\pi/2d$. From Ref. 18.

frequency 87 cm^{-1} at T=25K. They argue that this mode corresponds to the symmetric TO amplitude mode derived from the Kohn anomaly mode (mode b in Fig. 3-5). Two weaker temperature-dependent Raman peaks, with frequency 153 and 197 cm^{-1} at T=25K, are assigned to other symmetric TO amplitude modes at $q=2\pi/a-2k_F$ in the reduced zone scheme (modes c and d in Fig. 3-5). Associated with each symmetric amplitude mode, there should be an antisymmetric phase mode at lower frequency[19]. In the picture of Sugai et. al., the modes we observe at 38, 149 and 194 cm^{-1} are naturally assigned to the antisymmetric phase modes associated with points b, c and d in Fig. 3-5. The 35-GHz microwave mode is assigned to the antisymmetric phase mode associated with point a in Fig. 3-5. No Raman-active mode has been seen at 38 cm^{-1}, indicating that this is a totally antisymmetric mode. We note that a Raman-active mode associated with point a in Fig. 3-5 is expected in the Sugai et. al. picture. However, this frequency is too low to be observed in conventional Raman scattering experiments.

The Kohn anomaly mode is expected to have a large oscillator strength. It is the phonon mode most strongly coupled to the electrons in $(TaSe_4)_2I$. If the Brillouin zone were twice as large, the Kohn anomaly mode would soften to zero frequency at the Peierls transition temperature T_P and give birth to the LRA amplitudon and acoustic phason in the CDW state. LRA calculated the oscillator strength of the acoustic phason using Eq. 3-3 with $e^*=e$, the full electronic charge. The effective mass of the 38 cm^{-1} mode derived from Eq. 3-3 with the full electronic charge is $m^*=200m_e$, a plausible value which is between the electronic and ionic masses.

The picture of Sugai et. al. suggests that all CDW materials with $2k_F$ in the second Brillouin zone should have a linear response spectrum similar to that of $(TaSe_4)_2I$. The blue bronze $K_{0.3}MoO_3$ has $2k_F$ in the second Brillouin zone. A giant FIR mode at a higher frequency than the pinned mode has been observed in $K_{0.3}MoO_3$. $NbSe_3$ has $2k_F$ in the first Brillouin zone, but the presence of a giant FIR mode is unclear because of the large concentration of free carriers at low temperatures. TaS_3 has $2k_F$ in the first Brillouin zone

and is an insulator at low temperatures. TaS_3 should not have a giant FIR mode in the picture of Sugai et. al., but it should have an optical phason. A measurement of the FIR linear response spectrum of TaS_3 is thus important to an understanding of the linear response of CDW conductors[20].

By completing the excitation spectrum of $(TaSe_4)_2I$, we have demonstrated conclusively the presence of an IR-active mode of the CDW with large oscillator strength and with frequency between the pinned mode and the Peierls gap. Combined with Raman data and evidence of similar modes in other CDW systems, our results require a significant modification of the standard LRA picture of the CDW excitation spectrum. Giant FIR modes previously observed in other CDW conductors have been assigned to the pinned mode. The assumption was that the pinned mode is the only candidate for a giant FIR mode in a CDW conductor. These assignments, especially in materials which have $2k_F$ in the second Brillouin zone (for example, KCP)[21] should be re-examined.

References

[1] G. Travaglini and P. Wachter, Phys. Rev. B 30, 1971 (1984)

[2] W. A. Challener and P. L. Richards, Solid State Commun. 52, 117 (1984)

[3] H. K. Ng, G. A. Thomas and L. F. Schneemeyer, Phys. Rev. B 33, 8755 (1986)

[4] P. Brüesch, S. Strässler and H. R. Zeller, Phys. Rev. B **12**, 219 (1975)

[5] P. A. Lee, T. M. Rice and P. W. Anderson, Solid State Commun. 14,703 (1974)

[6] S. Sridhar, D. Reagor and G. Grüner, Phys. Rev. Lett. 55, 1196 (1985)

[7] D. Reagor, S. Sridhar, M. Maki and G. Grüner, Phys. Rev. B 32, 8445(1985)

[8] R. P. Hall, M. S. Sherwin and A. Zettl, Solid State Commun. 55, 307 (1985); S. Sridhar, unpublished.

[9] The mosaic was constructed as follows. The crystals were placed face down on a glass slide inside of a 1-cm diameter metal ring. Warm (but not liquid) wax was pressed onto the backs of the crystals. The wax and a small amount of $(TaSe_4)_2I$ were scraped away from the backs of the crystals. Stycast epoxy was then poured into the metal ring over the backs of the crystals. The wax prevented the stycast from covering the experimentall-important face-down crystal surfaces. When the epoxy was set, the epoxy-wax-sample plug was pushed out of the metal ring. The experimentally-important crystal surfaces were clean and coplanar. The plug was then pressed right-side up into a hole in a copper sample holder. The tight fit of the plug and the Stycast contact to the $(TaSe_4)_2I$ crystals ensured good thermal contact between the crystals and the cold stage.

When it came time to evaporate gold onto the sample surface, the wax was a nuisance. It was necessary to cool the sample in the evaporator bell jar in order to prevent the wax from melting or evaporating. After the gold evaporation, gold was (carefully) scraped from the wax in the cracks between the crystals.

10 H. P. Geserich, G. Scheiber, M. Dürrler, F. Lévy and P. Monceau, Physica **143B**, 198 (1986).

11 The 10% rise in the FIR reflectance between 8 and 50 cm^{-1} is important in obtaining the fitting parameter f_0=38 cm^{-1} for the giant mode. Experienced FIR spectroscopists are correctly suspicious of such small effects in this frequency range. We have no reason to doubt the validity of our data between 8 and 50 cm^{-1}. The rise is statistically significant (much larger than the noise fluctuations between 15 and 40 cm^{-1}). The only obvious source of frequency-dependent systematic errors is diffraction from the surface of the mosaic. The large size of the crystals making up the mosaic, and the frequency-independence of the reflectance of the gold-evaporated sample in this frequency range, make that possibility seem unlikely. However, there may remain a few doubting Thomases who are not convinced. Assuming that the data below 40 cm^{-1} were spurious, they would say that say that the zero-crossing of ε_1 at 100 cm^{-1} could be the LO mode of a large-oscillator strength mode whose TO mode has been observed in the microwave at 35 GHz[7]. Using the Lyddane-Sachs-Teller relation, we can show this assignment to be impossible. The dimensionless oscillator strength $S = \varepsilon_0 - \varepsilon_\infty$ for the microwave mode is 10^4. Based on the reflectivity of 0.6 at 300 cm^{-1}, we deduce $\varepsilon_\infty \approx 75$. The LST relation

$$\frac{\varepsilon_0 - \varepsilon_\infty}{\varepsilon_\infty} = \frac{\omega_L^2}{\omega_T^2} \qquad (3\text{-}3)$$

predicts the longitudinal mode frequency ω_L=12.5 cm^{-1}, eight times lower than the observed reflectance edge. The existence of a mode near 40 cm^{-1} is also supported by transmittance data on a sample of order 100 microns thick. The transmittance decreases from 5% at 10 cm^{-1} to less than 0.5% at 40 cm^{-1}

[12] R. J. Cava, R. M. Fleming, P. B. Littlewood, E. A. Rietmann, L. F. Schneemeyer and R. G. Dunn, Phys. Rev. B **30**, 3228. The frequencies in Table 3-2 are for T/Tp≈0.5)

[13] J. Brill

[14] For reviews of the mean field theory of the Peierls transition and the CDW excitation spectrum, see G. A. Toombs, Physics Reports **40**, 181 (1978); A. J. Berlinsky, Rep. Prog. Phys. **42**, 1243 (1979)

[15] M. B. Walker, Can. J. Phys. **56**, 127 (1978)

[16] H. Fujishita, M. Sato, S. Sato and S. Hoshino, J. Phys. C**18**, 1105 (1985)

[17] Effective mass obtained by solving Eq. 3-3 for m using $n=1.6\times10^{21}$ cm^{-3} (the electronic density) and e*=0.05e, where e is the electronic charge.

[18] S. Sugai, M. Sato, and S. Kurihara, Phys. Rev. B **32**, 6809 (1985)

[19] Ref. 5. See also W. A. Challener, Ph. D. Thesis (1983)

[20] W. N. Creagor, P. L. Richards and A. Zettl, measurement in progress.

[21] KCP was extensively studied in the 1970's. KCP has $2k_F$ in the second Brillouin zone (Phys. Rev. B **8**, 571 (1973)). A giant FIR mode was observed in KCP at 15 cm^{-1} (Ref. 4). To my knowledge, detailed frequency-dependent conductivity studies have not been performed below 3 cm^{-1}. In the picture of Sugai et. al., both a FIR and a microwave mode are expected.

4. Far infrared optical properties of polycrystalline samples of the high-T_c superconductors $La_{1.85}Sr_{0.15}CuO_4$ and $La_{1.85}Ca_{0.15}CuO_4$.

4.1. Introduction

A vigorous research effort into the electrodynamics of high-Tc superconductors has been fueled by the great scientific and technological importance of this subject. The existence and magnitude of the superconducting energy gap are crucial scientific issues that have traditionally been illuminated by far infrared (FIR) spectroscopy. The possibility of devices that operate with low resistive loss in the 100-1000 GHz frequency range at liquid nitrogen temperature is of technological importance. In this chapter we use experimental and theoretical results on the temperature dependence of the FIR reflectance of polycrystalline $La_{1.85}(Sr,Ca)_{0.15}CuO_4$ to address the following questions. First, can one extract an energy gap from the FIR reflectance of high-Tc superconductors? Second, how well do the temperature dependent electrodynamics of the BCS theory fit high-Tc superconductors? Third, do the ac losses for frequencies much less than the energy gap predicted by BCS scale with temperature as predicted by BCS?

Although the mechanism for superconductivity in high-Tc superconductors is not yet clear, experiments have provided important guidelines. Measurements on Josephson junctions[1] indicate that current is carried by pairs of electrons. However, the absence of an observable isotope shift[2] in T_c in $YBa_2Cu_3O_7$ and the small size of the oxygen isotope shift[3] in $La_{1.85}Sr_{0.15}CuO_4$ indicates that phonons alone probably do not mediate the pairing. It has been suggested that a BCS-like theory in which excitons or other relatively high energy excitations mediate electron pairing may apply[4]. The electrodynamics predicted by this class of theories should be close to that of BCS theory. In particular, a mean field treatment of these theories should predict an energy gap with a temperature dependence and magnitude identical to that predicted by BCS. The magnitudes of the energy gap extracted by tunneling for[5] $La_{1.85}Sr_{0.15}CuO_4$ and[6] $Y_1Ba_2Cu_3O_7$ have been

4.5 to 9 and 3.7 to 5.6 respectively, consistent with a strong coupling pairing theory. In contrast, Anderson[7] has suggested that there may be no observable energy gap in high-Tc superconductors if they are described by a resonating valence bond model.

We begin with a review of relevant and sometimes conflicting interpretations of the FIR reflectance of polycrystalline $La_{1.85}Sr_{0.15}CuO_4$. Many groups[8-11] have observed a reflectance edge near 50 cm^{-1} in the superconducting state of polycrystalline $La_{1.85}Sr_{0.15}CuO_4$. This edge was first assigned to the onset of absorption due to excitations across a superconducting energy gap. The magnitude of the energy gap extracted by the first such assignments[8-10] was from 1.6 to 2.7 k_BT_c, considerably smaller[11,12] than the BCS prediction of $3.5k_BT_c$ and the tunneling measurements[5]. Recently, an entirely different mechanism for the 50 cm^{-1} edge in polycrystalline $La_{1.85}Sr_{0.15}CuO_4$ has been proposed by Bonn et. al.[13] They have assigned this edge to a zero-crossing of the real part of the dielectric function ε_1, caused by a strong resonance at 240 cm^{-1} and a weaker resonance at 500 cm^{-1}. Under this interpretation, neither the existence nor the value of the energy gap are obvious from far infrared reflectance data.

A priori, one might think that the temperature dependence of the 50 cm^{-1} reflectance edge could be used to distinguish between the hypothesis of an energy gap and the hypothesis of a plasmon. We report here measurements of the FIR reflectance of polycrystalline samples of $La_{1.85}Sr_{0.15}CuO_4$ and $La_{1.85}Ca_{0.15}CuO_4$. We have probed the temperature dependence of the FIR reflectance of $La_{1.85}Sr_{0.15}CuO_4$. At temperatures well-below T_c, we find a reflectance edge whose frequency scales with T_c in different materials. The frequency of this edge in a given material scales with temperature as the BCS gap. We also describe a model to determine the temperature dependence of the reflectance edge predicted by the plasmon hypothesis. The superconducting state is modeled using the temperature dependent theory of Mattis and Bardeen, which should hold for any mean field pairing theory of superconductivity, independent of the nature of the coupling. We find

that the plasmon and the energy gap hypotheses give nearly identical predictions for the temperature dependence of the frequency of the reflectance edge. The predictions for the temperature dependence for both theories agree with experimental results. We conclude that a mean field, BCS-like theory of the electrodynamics of high-Tc superconductors is consistent with the FIR data. However, it seems premature to deduce an energy gap from FIR data.

The most technologically significant result of the FIR work described in this chapter is that our experimentally observed temperature dependence of the absorption in the superconducting state of polycrystalline $La_{1.85}Sr_{0.15}CuO_4$ for frequencies well below the reflectance edge seems well described by the temperature dependent Mattis-Bardeen theory, or equivalently by a two-fluid model. If this result holds for $Y_1Ba_2Cu_3O_7$, it imposes constraints on the operating temperature of fast superconducting devices made from this material.

4.2. Experiment

The samples used for the measurements reported here are 1 cm diameter ceramic pellets of $La_{1.85}Sr_{0.15}CuO_4$ and $La_{1.85}Ca_{0.15}CuO_4$ kindly provided by Prof. A. Stacy. The pellets were not polished before the optical experiments. Fig. 4-1 shows the magnetic susceptibility $\chi(T)$ for the Sr doped sample. The susceptibility drops sharply as the temperature is decreased below T_{co} = 36K, signaling the onset of the superconducting state. For the Ca doped sample, T_{co} = 17K. At low temperatures the Sr doped sample showed a large volume exclusion of a magnetic field, indicating that a large fraction of the sample consisted of a superconducting phase. The Ca doped sample excluded only 1/5 as much of the magnetic field as the Sr doped sample. The details of the sample preparation have been described elsewhere[8]. The superconducting phase transition was also observed directly from the FIR measurements in the Sr doped sample. The reflectance near 15 cm^{-1} began to increase sharply as a function of decreasing temperature at 37K±1K, (see Fig. 4-

6). This temperature is in agreement with the value of T_{co} determined from $\chi(T)$, and thus we scale all temperature and material dependent properties to T_{co}.

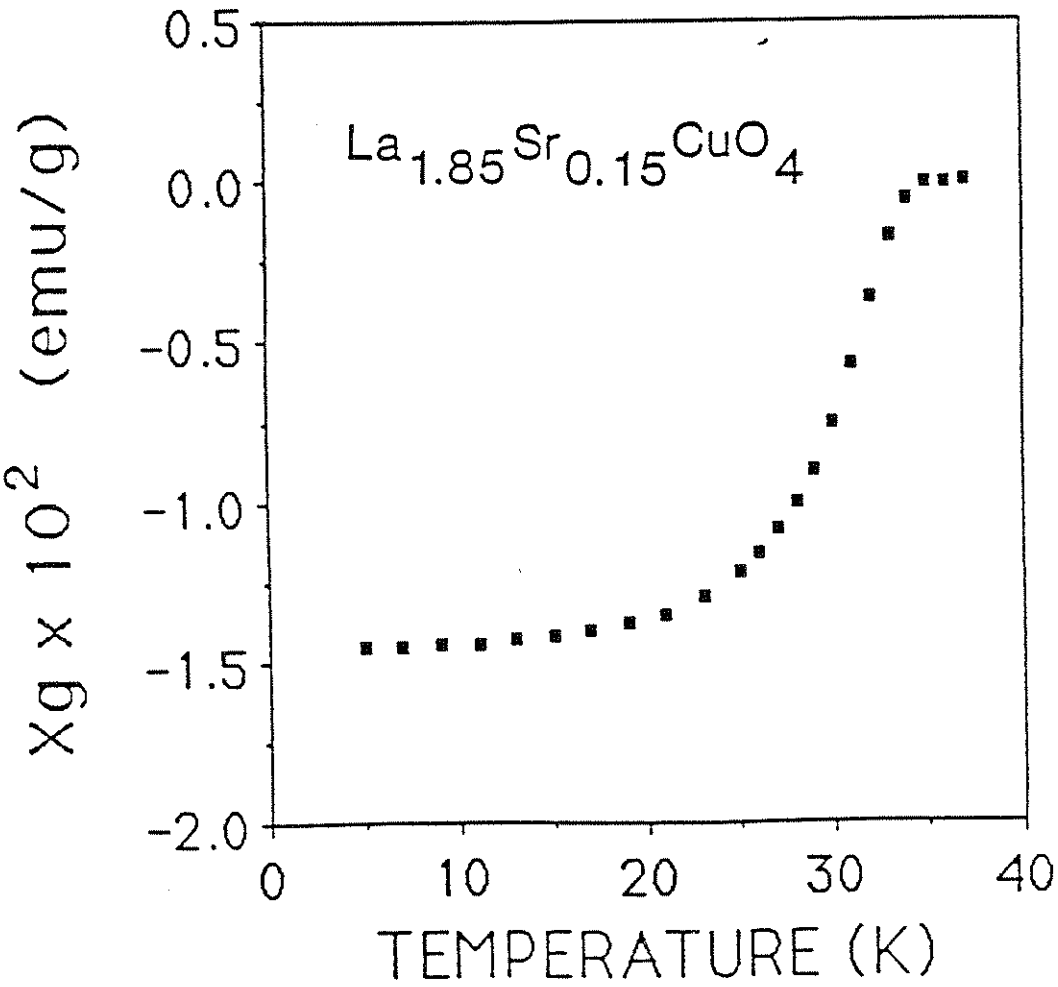

Fig. 4-1: Magnetic susceptibility χ vs. temperature for the Sr doped sample. The onset temperature T_{co}=36K. This data was provided by Prof. A. Stacy.

During the experiment, chopped radiation with a 10° angle of incidence was detected after a single reflection off the sample surface by a sensitive composite bolometer. The radiation source for the FIR experiments was a Michelson Fourier spectrometer. The sample was mounted in the transmittance-reflectance apparatus (see Chapter 2). The transmittance-reflectance apparatus was configured as in Fig. 2-3, except that no polarizer was in place. Light scattered by surface roughness was lost in the light baffles, not collected by the light pipe. The FIR system is described in detail in Chapter two.

At each sample temperature for which a reflectance spectrum was recorded, the data were normalized to a polished brass mirror. After all measurements on $La_{1.85}Sr_{0.15}CuO_4$ had been performed, we attempted to correct our results for the effects of surface scattering by evaporating metal onto the sample surface and using the metallized sample as a reference. The reflectance of the metallized sample was independent of frequency for frequencies less than 60 cm^{-1}, indicating that our data in this frequency range is not much affected by the roughness of the sample surface. Above 60 cm^{-1}, however, the reflectance of the metallized sample decreased continuously with increasing frequency, indicating that our absolute reflectance data in this frequency range is significantly affected by surface scattering. Small cracks occurred in the sample surface just before metallization which prevented an accurate final normalization. However, the conclusions of this chapter are not affected by surface scattering: we are investigating changes in the reflectance as a function of temperature, and thus are relatively insensitive to temperature independent losses due to sample geometry.

Fig. 4-2a shows the ratio R_s/R_n of the superconducting to the normal state reflectance for $La_{1.85}Sr_{0.15}CuO_4$. Here, R_s and R_n are the reflectances measured at 6K and 52K, respectively well below and well above T_{co}. R_s/R_n is greater than one for frequencies less than 60 cm^{-1}($=2.4k_BT_{co}(Sr)$). As the frequency increases past 60 cm^{-1}, R_s/R_n drops below unity, reaches a minimum at 70 cm^{-1}, and then approaches unity from below. This

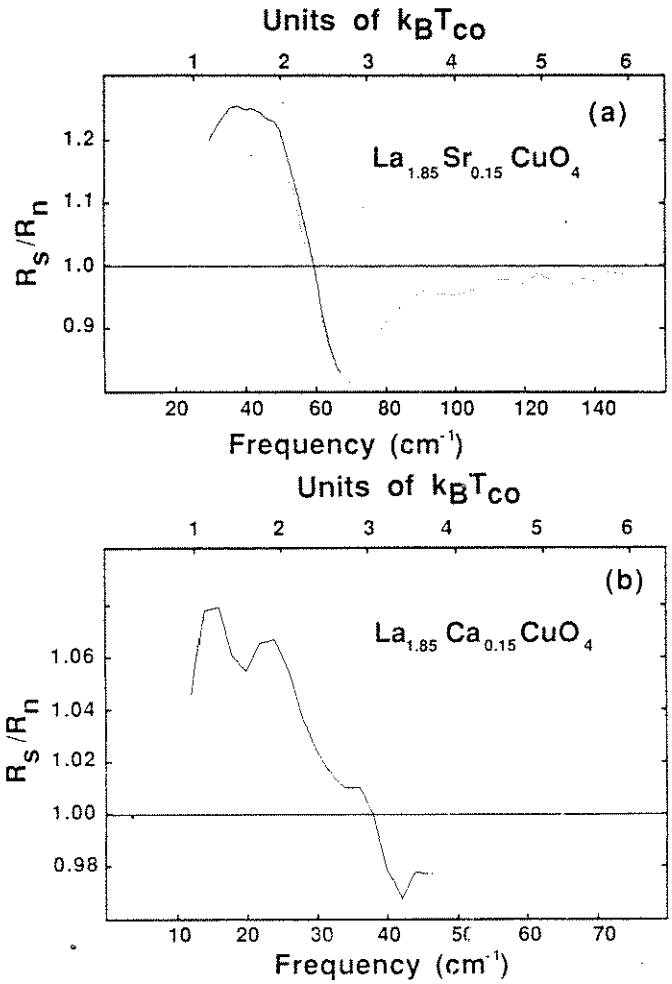

Fig. 4-2: The ratio R_S/R_n of the superconducting to normal state reflectance as a function of frequency for polycrystalline $La_{1.85}Sr_{0.15}CuO_4$ and $La_{1.85}Ca_{0.15}CuO_4$. A solid line has been drawn to mark $R_S/R_n=1$. The scale of Fig. 4-2b is expanded relative to that of Fig. 4-2a by the ratio of the superconducting onset temperatures $T_{co}(Sr)/T_{co}(Ca)=36K/17K$, showing that the frequency of the characteristic features of R_S/R_n scales with T_{co}.

(a) $La_{1.85}Sr_{0.15}CuO_4$: R_S and R_n are reflectances measured at 5K and 52K. The solid and dotted lines represent data from different experimental runs.

(b) $La_{1.85}Ca_{0.15}CuO_4$: R_S and R_n are reflectances measured at 9K and 24K, respectively.

behavior is consistent with that reported by many groups[9-11,13]. Fig. 4-2b shows the first published reflectance data for $La_{1.85}Ca_{0.15}CuO_4$. We have expanded the frequency scale of Fig. 4-2b relative to 4-2a by the ratio of the transition temperatures of the two materials $T_{co}(Sr)/T_{co}(Ca)=36/17$. The behavior of R_s/R_n is similar to that for the Sr doped material, with characteristic frequencies scaled by T_{co}. Below 30 cm^{-1}, R_s/R_n is greater than one. Between 30 cm^{-1}($=2.4k_BT_{co}(Ca)$) and 40 cm^{-1} ($=3.2k_BT_{co}(Ca)$), R_s/R_n drops below unity. The deviations of R_s/R_n from unity are smaller for the Ca than for the Sr doped sample. These differences may arise from the fact that, based on magnetic measurements, a smaller fraction of the Ca doped sample was of a superconducting phase.

Fig. 4-3 shows a series of normalized reflectance spectra of $La_{1.85}Sr_{0.15}CuO_4$ for frequencies 10 to 90 cm-1 at selected temperatures above and below T_{co}=36K. In the low-temperature regimes well below T_{co}, the reflectance follows a consistent behavior. At low frequencies, R is near unity and decreases only slightly with increasing frequency. At higher frequencies, R drops sharply at a characteristic frequency f_0 and begins to flatten out once again at an even higher characteristic frequency f_1. At 6K, f_0 and f_1 are clearly identified at 50 and 66 cm^{-1}, respectively. Both f_0 and f_1 decrease with increasing temperature above 6K. Above 36K, f_0 and f_1 are no longer clearly identifiable. At 52K, the reflectance R decreases smoothly with increasing frequency. Above 50K, the reflectance curve was found to be rather insensitive to temperature.

If one assumes (as is done in Refs. 8-12) that the real part of the dielectric function is negative throughout the FIR, then a general interpretation of the spectra in Figs. 4-1 and 2 is straightforward. The reflectance feature windowed by f_0 and f_1 can be identified as the onset of photon absorption at the superconducting energy gap 2Δ. A similar interpretation is possible for the $La_{1.85}Ca_{0.15}CuO_4$ data shown in Fig. 4-2b. The fact that the frequency of these features in the two materials at temperatures much less than T_{co} scales with T_{co} is consistent with the energy gap hypothesis. As we shall see below, the

temperaturedependence of the reflectance edge is also consistent with the hypothesis of a BCS-like energy gap.

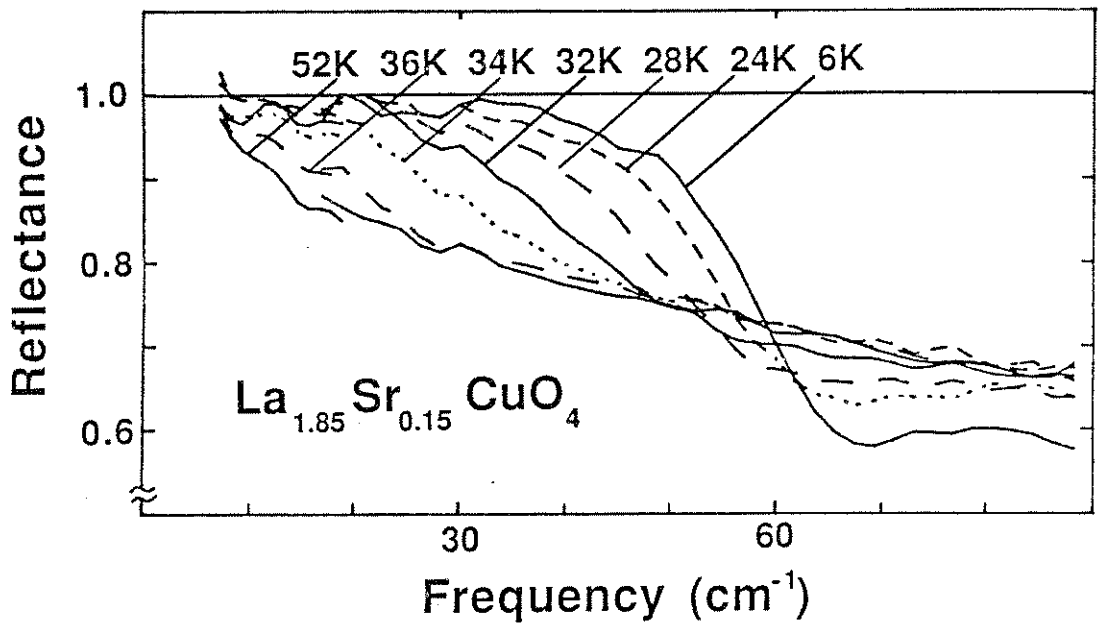

Fig. 4-3: Reflectance of polycrystalline $La_{1.85}Sr_{0.15}CuO_4$ at selected temperatures above and below T_{co}. The temperature dependent reflectance edge has been interpreted as an energy gap[a] and as a plasma edge[b]. A solid line marks R=1.

[a] Refs. 8-12 [b]Ref. 13

4.3. Model for the Reflectance Edge

In the remainder of this chapter we construct a model to investigate the temperature dependence of the reflectance predicted by the plasmon hypothesis, and we compare its predictions to those of the energy gap hypothesis. We note that the temperature dependence of the plasmon hypothesis has not been investigated previously. Finally, we investigate the scaling of the reflectance of polycrystalline $La_{1.85}Sr_{0.15}CuO_4$ near 16 cm^{-1} (500 GHz) with temperature for both the energy gap and plasmon hypotheses.

The interpretation of the normal state reflectance of polycrystalline samples of $La_{1.85}Sr_{0.15}CuO_4$ is complicated by the fact that the crystal structure of this material is highly anisotropic. The conduction electrons are thought to be mostly confined to sheets parallel to the a-b plane, with a relatively low conductivity perpendicular to the a-b plane. Two approaches have been taken to account for the effect of anisotropy on FIR spectra of polycrystalline samples, and these approaches yield different assignments for the observed features in the reflectance spectra. Thomas et. al.[14] have argued that since the size of typical crystallites is much smaller than a wavelength at FIR frequencies, a long wavelength effective medium theory should apply. In such a theory, the reflectance is calculated from a dielectric function which is an average over all crystallite orientations. Under this interpretation, the 240 cm^{-1} resonance first reported by Bonn et. al. must have an extremely large oscillator strength and must have components both in the a-b plane and perpendicular to the a-b plane[15]. Furthermore, if one interprets the 50 cm^{-1} edge in the superconducting state as a plasma edge, this feature must also have components both in and out of the a-b plane. Schlesinger et. al.[16] have analyzed the spectra of their polycrystalline samples by using a short wavelength approximation and averaging reflectivities over different crystallite orientations, rather than averaging the dielectric function. This approach is combined with the assumption that the normal state reflectance of $La_{1.85}Sr_{0.15}CuO_4$ should

closely resemble that of La_2NiO_4, a material of the same crystal structure on which FIR measurements of a single crystal have been made[17]. In La_2NiO_4, there is a moderate oscillator strength resonance near 250 cm^{-1} which has components only perpendicular to the a-b plane. Schlesinger et. al. assign the 240 cm^{-1} resonance to vibrations perpendicular to the a-b plane, and assign the temperature dependent reflectance edge near 50 cm^{-1} to a plasma oscillation also perpendicular to the a-b plane. The first infrared data on single crystals and oriented films of the related Y-Ba-Cu-O compound show that the phonon peaks in that case are confined to the c-axis[21].

The analyses of Thomas et. al. and Schlesinger et. al. both assume a low frequency plasmon. The differences are that the two analyses give different assignments to the direction of the plasma oscillation, and different oscillator strengths for the 240 cm^{-1} mode are needed to fit the normal state spectra. In our modeling, since we are concerned with wavelengths larger than 50 microns (much greater than the size of the <10μm crystallites) we adopt a long wavelength approximation in which the reflectance is given by the standard formula $R=|(\varepsilon^{1/2}-1)/(\varepsilon^{1/2}+1)|^2$ where R is the reflectance and $\varepsilon= \varepsilon_1 +i\, \varepsilon_2$ is an average dielectric function. In order to convincingly model the reflectance in the normal state, it is necessary to consider the reflectance over a broad frequency range. We have chosen the best available data in each frequency range. We use our data in the 10 to 90 cm^{-1} range, those of Bonn et. al.[13] (which are close to our reported data from 50 to 90 cm^{-1}) from 90 to 1000 cm^{-1}, and those of Orenstein et. al.18 from 1000 to 24000 cm^{-1}. The most important conclusions of our modeling will prove to be insensitive to the details of the data above 1000 cm^{-1}.

In the normal state, we model the reflectance for frequencies less than 200 cm^{-1} with a Drude term for the free carriers, a Lorentz oscillator for the 240 cm^{-1} mode deduced by Bonn et. al., and a background dielectric constant for the oscillator strength at much higher frequencies than the FIR. Thus,

$$\varepsilon_1(\omega)= \frac{-\omega_p^2\tau^2}{1+\omega^2\tau^2} + \frac{\omega_T^2(\omega_1^2-\omega^2)}{(\omega_1^2-\omega^2)^2+\frac{\omega^2}{\tau_1^2}} + \varepsilon_\infty \qquad (4.1)$$

$$\varepsilon_2(\omega) = \frac{\omega_p^2\tau}{\omega(1+\omega^2\tau^2)} + \frac{\omega_T^2(\frac{\omega}{\tau_1})}{(\omega_1^2-\omega^2)^2+\frac{\omega^2}{\tau_1^2}} \qquad (4.2)$$

where ε_1 and ε_2 are the real and imaginary parts of the dielectric function, ω is the incident photon frequency, ω_p and τ are the plasma frequency and relaxation time of the free carriers ω_T, $\omega 1$, and $\tau 1$ are the plasma frequency, resonant frequency and relaxation time of the Lorentz oscillator, and ε_∞ is the background dielectric constant.

We determine the parameters of our normal state fit as follows. Orenstein et. al. fitted their high frequency reflectance data to a model in which 94% of the oscillator strength of the electrons in the conduction band is associated with a (non-superconducting) gap at 3600 cm^{-1} which contributes a constant ε_1 =20 in the FIR. The remaining 6% is associated with a term of the Drude form. We have parameterized the FIR resonances at 240 cm^{-1} and 500 cm^{-1} deduced by Bonn et. al. by Lorentz oscillators and have added them to the Orenstein et. al. model. We adjusted the oscillator strength of the Drude term so that the sum of the oscillator strengths of the Drude term and the two resonances adds up to 6% of the total oscillator strength in the conduction band proposed by Orenstein et. al. In the 0-100 cm^{-1} range the resonance at 500 cm^{-1} can be modeled by a constant contribution to ε_1 of 3.

The parameters of our model are as follows: ω_p=3350 cm^{-1}, ω_T=1860 cm^{-1}, ω_1=239 cm^{-1}, $1/\tau_1$=33 cm^{-1}, and ε_∞ =23. the relaxation time τ of the free carriers is adjusted to fit our normal state data. We find $1/\tau$=2000 cm^{-1} gives an adequate fit to our data and those of Bonn et. al.[13] in the frequency range 10-100 cm^{-1}. Given the inhomogeneous nature of these samples, a detailed fit to the reflectance is not warranted. We note that our model

predicts a positive ε_1 at zero frequency in the normal state: the ability of heavily damped free carriers to screen electromagnetic radiation is overwhelmed by the polarizability of the FIR resonances.

Once we fit the normal state reflectance, we calculate the reflectance at selected temperatures in the superconducting state with no additional adjustable parameters. To model the reflectance in the superconducting state, we assume an energy gap of magnitude and temperature dependence predicted by weak coupling BCS. The Drude terms in Eqs. 4.1 and 4.2 are replaced with terms calculated from the temperature dependent Mattis-Bardeen[20] expressions for the frequency dependent conductivity in the superconducting state. We have integrated numerically these singular integrals using Gaussian and Chebyshev integration routines[21] (See Appendix A). The Mattis-Bardeen expressions are valid in the limits in which the penetration depth of the electromagnetic radiation is much larger than or much less than the coherence length. The former limit applies in the superconducting oxides.

The temperature dependent reflectance from our plasmon model is shown in Fig. 4-4. Many qualitative features of the data are apparent. Below $T=T_c$, the calculated reflectance shows systematic trends similar to the data of Fig. 4-3. For low frequencies, the reflectance is near unity. At a frequency f_0 the reflectance begins to drop and at f_1 it begins to flatten out. For $T< 34K$ there is a minimum. The reflectance then approaches the normal state reflectance from below. The steepness of the reflectance edge increases with decreasing temperature. At T=6K the reflectance edge at 80 cm^{-1} is extremely sharp. The experimentally observed reflectance edge is broader, which is to be expected if sample inhomogeneity leads to damping mechanisms not included in the model. The assumed energy gap for T=6K is 88 cm^{-1} and is marked by an arrow in Fig. 4-4. There is no obvious feature in the calculated reflectance at this frequency. This shows that if the

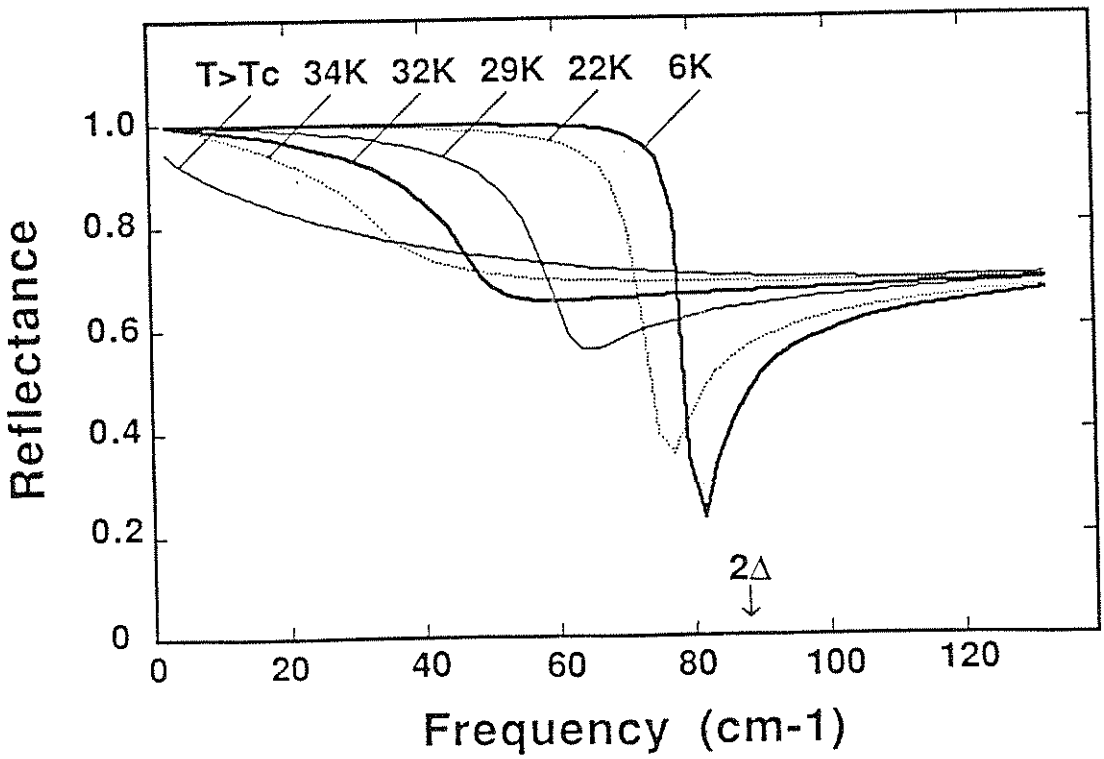

Fig. 4-4: Reflectance calculated at selected temperatures from a model which contains free carriers and a strong phonon, and treats the reflectance edge as a plasma edge. The model qualitatively reproduces the experimental data of Fig. 4-3. The position of the energy gap $2\Delta(T=0)$ used in this calculation is marked with an arrow. There is no obvious feature in the calculated reflectance at this frequency.

plasmon hypothesis is correct, it is impossible to extract a value for the energy gap by simple inspection of the reflectance.

The derivatives of the reflectance curves in Figs. 4-3 and 4-4 show clear minima at a frequency fp between f_0 and f_1 and thus enable an objective comparison of the temperature dependence of the reflectance edge in the model and the experiment. We have plotted the temperature dependence of f_p for both experiment and model in Fig. 4-5. We have also plotted the temperature dependence of the BCS gap. All quantities are normalized to 1 for temperatures much less than T_{co}. We see that the temperature dependence of the reflectance edge in both the model and the experiment closely fits the temperature dependence of the BCS gap. Thus the predicted temperature dependences of the reflectance edge in the plasmon hypothesis and the energy gap hypothesis are *virtually indistinguishable*. The only difference between the temperature dependence predictions of the two hypotheses is that f_p in the plasmon hypothesis lies at slightly higher frequencies than the BCS curve for temperatures $T_{co}/3<T<T_{co}$. This arises in the model from the frequency dependence of the contribution to $\varepsilon 1$ of the 240 cm^{-1} resonance.

In the model the reflectance edge is caused by a zero-crossing of ε_1. We hereafter refer to the frequency of the reflectance edge as the plasma frequency. A second higher plasma frequency is of course to be expected at near IR or visible wavelengths. The temperature dependence of the reflectance may be qualitatively understood as follows. At T=0, the maximum number of carriers are condensed into the dissipationless superconducting state and the system can screen electromagnetic radiation effectively for frequencies as high as the low temperature plasma frequency 80 cm^{-1}. As the temperature is increased toward T_c, the fraction of carriers in the superconducting state decreases with the temperature dependence of the order parameter, decreasing the ability of the free carriers to screen and lowering the plasma frequency until it reaches zero for T>Tc. The broadening of the

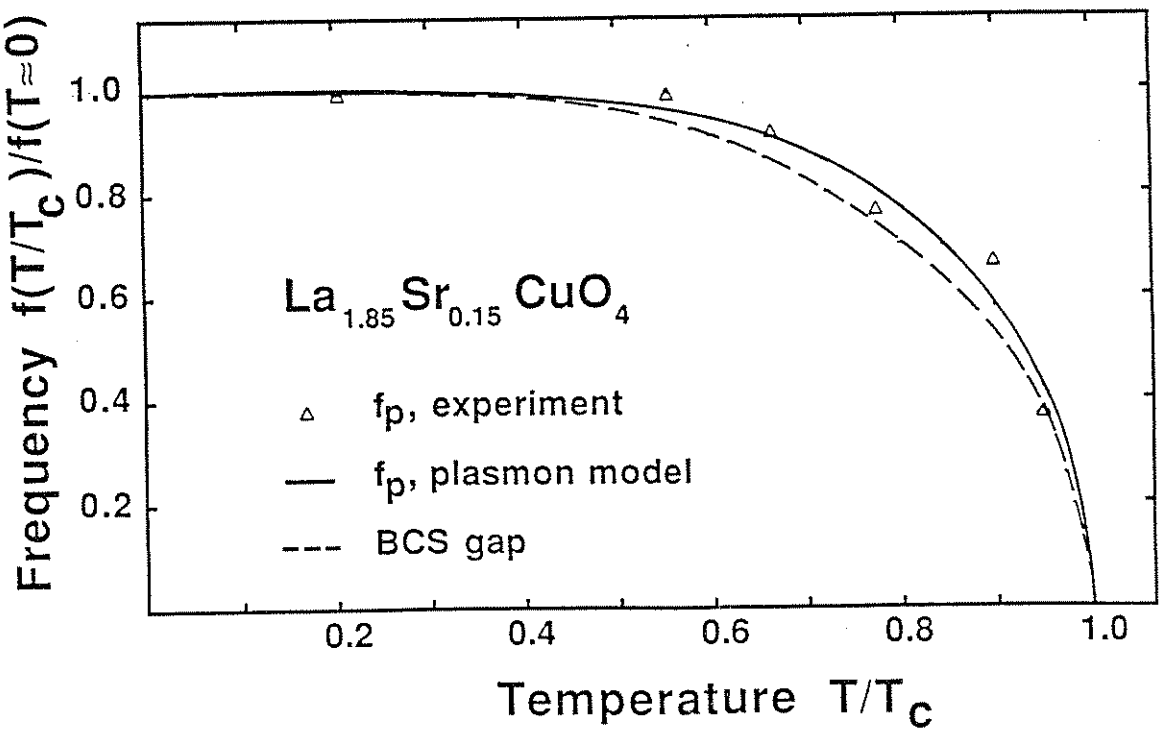

Fig. 4-5: Frequency of the reflectance edge vs. reduced temperature for experiment (triangles) and for the plasmon model (solid line). The BCS gap is also plotted (dashed line). All quantities are normalized to 1 at T≈0.

reflectance edge with increasing temperature arises from finite dissipation for $\omega<2\Delta(T)$ due to quasi particles excited across the superconducting gap.

The plasmon hypothesis as implemented in our model can also account for the scaling of the frequency of the reflectance edge with T_{co}. We have observed a clear bump in the reflectance of $La_{1.85}Ca_{0.15}CuO_4$ near 250 cm^{-1}, indicating at least one strong phonon similar to that observed in the Sr doped material. If we assume that the free carrier density and relaxation times in $La_{1.85}Ca_{0.15}CuO_4$ and $La_{1.85}Sr_{0.15}CuO_4$ are comparable, and that the energy gap scales with the transition temperature, then the oscillator strength condensed into the superconducting state should also scale with transition temperature and so should the frequency of the reflectance edge.

Although the plasma frequency in our model depends critically on the parameters of the normal state fit, the scaling of the plasma frequency with temperature does not. Given the uncertainties inherent in modeling the normal state reflectance of polycrystalline $La_{1.85}Sr_{0.15}CuO_4$, we do not attempt to make more than a rough comparison between the plasma frequencies in the model and in the experiment, and we are pleased that they agree to within 30%. Agreement could clearly be improved by adjusting the model parameters or the magnitude of the energy gap. However, our conclusions about the scaling of the plasma frequency with temperature and with T_c are robust. These conclusions depend only on the normal state being characterized by a low free carrier density and a resonance that has large enough oscillator strength to yield a positive ε_1 for low FIR frequencies. Thus our main results should be valid for both the long wavelength effective medium characterization of the normal state which we have adopted, and for the short wavelength approximation adopted by Schlesinger et. al.

4.4. Low Frequency Reflectance

Finally, we investigate the scaling of the reflectance of polycrystalline $La_{1.85}Sr_{0.15}CuO_4$ with temperature at sub-mm wavelengths. We give the reflectance in a manner that is independent of the details of the fit to the normal state and independent of small (1-2%) temperature independent losses due to surface scattering or to a normal surface layer. In Fig. 4-6, we have plotted $(R(T)-R_n)/(R_s-R_n)$ averaged over a 2 cm^{-1} band about 16 cm^{-1} for our experiment (squares) and our model of the plasmon hypothesis (solid line). R_n and R_s are here the reflectance at T=37K and at T=24K. The agreement between model and experiment is quite good. A model dielectric function which does not include the 240 cm^{-1} phonon (consistent with the energy gap hypothesis) gives results identical to those of the plasmon hypothesis. This indicates that the simple Mattis-Bardeen model of the superconducting state, which is equivalent a two fluid model with current carried by normal and superconducting carriers, is adequate to describe the temperature dependence of the reflectance at sub-mm wavelengths. This temperature dependence cannot be used to distinguish between the plasmon and the energy gap hypotheses.

In order to assess the feasibility of using high-Tc superconductors for the construction of electronic devices that operate at sub-mm wavelengths, it is useful to compare the losses in these materials for frequencies less than $2\Delta_{BCS}/4 \approx 0.9 k_B T_c$ (where our calculations should be valid) to the losses in a good metal like copper. The absorption A_{Cu} of copper in the FIR was calculated using the dc conductivity and the Hagen-Rubens relation. The absorption for $T>T_c$ of the $La_{1.85}Sr_{0.15}CuO_4$ sample discussed here is typical for sintered polycrystalline samples[11], and is roughly 200 times that of copper, independent of frequency to within 10% for frequencies less than $2\Delta_{BCS}/4 \approx 25$ cm^{-1}. Assuming no extrinsic surface losses and a temperature dependence of the absorption in the superconducting state described by BCS, $La_{1.85}Sr_{0.15}CuO_4$ would have to be cooled to

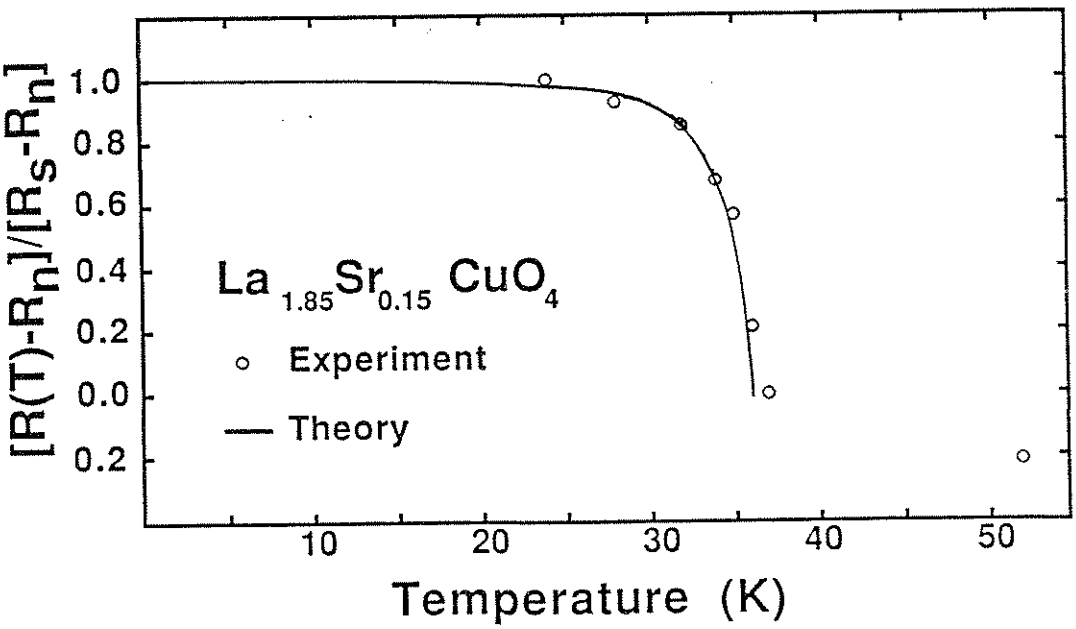

Fig. 4-6: Excess submillimeter reflectance $[R(T)-R_n]/[R_s-R_n]$ in the superconducting state vs. temperature. Here, R_s and R_n were measured at 24K and 37K respectively. In this frequency range, the predictions of the plasmon model and those of the simple Mattis-Bardeen expressions are indistinguishable. Both models (solid line) agree with the experimental results (circles).

$T/T_{co} \approx 0.4$ ($T \approx 14K$) before its absorption equalled that of room temperature Copper for frequencies less than 25 cm^{-1}. A recent measurement[22] of the reflectance of an epitaxial film of $Y_1Ba_2Cu_3O_7$ ($T_c \approx 90K$) showed a normal state absorption of roughly $60A_{Cu}$ for frequencies less than 200 cm^{-1}. If the temperature-dependent electrodynamics of this material for frequencies much less than the energy gap are also described by BCS, we estimate that this film would have to be cooled to $T/T_{co} \approx 0.5$ (45K) before its absorption equalled that of room temperature Copper for frequencies less than $2\Delta_{BCS}/4 \approx 60$ cm^{-1}. Thus it appears that for existing materials, devices made from high-Tc superconducting oxides will have to be cooled to temperatures lower than $T_c/2$ in order to have lower losses than good metals. Some improvement in the conductivity of single crystals and epitaxial films can be expected.

4.5. Conclusion

The reflectance polycrystalline samples of the high-Tc superconductor $La_{1.85}Sr_{0.15}CuO_4$ for frequencies less than 100 cm^{-1} is well described by BCS electrodynamics. Our results are therefore consistent with a mean field pairing theory of superconductivity. We have also shown that the temperature- dependence of the FIR reflectivity cannot be used to distinguish between the plasmon hypothesis and the energy gap hypothesis. The success of our model strengthens the plasmon hypothesis. However, a definitive understanding of the FIR dielectric function for $La_{1.85}Sr_{0.15}CuO_4$ must await a better understanding of the effect of crystal anisotropy on the reflectance of polycrystalline samples. Until this matter is clarified, it is premature to deduce the magnitude of the energy gap for polycrystalline samples from the infrared data.

References

[1] Daniel Estève, John M. Martinis, Christian Urbina, Michel H. Devoret, Gaston Collin, Philippe Monod, Michel Ribault and Alexandre Revcolevschi, Europhysics Letters **3**, 1237 (1987); W. R. McGrath, H. K. Olsson, T. Claeson, S. Eriksson and L.-G. Johannson, Europhys. Lett. **4**, 357 (1987)

[2] L. C. Bourne, M. F. Crommie, A. Zettl, Hans-Conrad zur Loye, S. W. Weller, K. J. Leary, Angelica M. Stacy, K. J. Chang, Marvin L. Cohen and Donald E. Morris, Phys. Rev. Lett. **58**, 2337 (1987); B. Batlogg, R. J. Cava, A. Jayaraman, R. B. van Dover, G. A. Kourouklis, S. Sunshine, D. W. Murphy, L. W. Rupp, H. S. Chen, A. White, K.T. Short, A. M. Mujsce, and E. A. Rietman, *ibid.*, 2333; L. C. Bourne, A. Zettl, T. W. Barbee III, and M. L. Cohen, Phys. Rev. B **36**, 3990 (1987)

[3] T. A. Faltens, W. K. Ham, S. W. Keller, K. J. Leary, J. N. Michaels, A. M. Stacy , H-C zur Loye, D. E. Morris, T. W. Barbee III, L. C. bourne, M. L. Cohen, S. Hoen and A. Zettl, Phys. Rev. Lett. **59**, 915 (1987); B. Batlogg, G. Kourouklis, W. Weber, R. J. Cava, A. Jayaraman, A. E. White, K. T. Short, L. W. Rupp and E. A. Rietman, Phys. Rev. Lett. **59**, 912 (1987)

[4] V. J. Emery, Phys. Rev. Lett. **58**, 2794 (1987)

[5] J. R. Kirtley, C. C. Tsuei, S. I. Park, C. C. Chi, J. Rozen, and M. W. Shafer, Phys. Rev. B **35**, 7216 (1987); M. E. Hawley, K. E. Gray, D. W. Capone II, and D. G. Hinks, *ibid.*, 7224 ; S. Pan, K. W. Ng, A. L. de Lozanne, J. M. Tarascon, and L. H. Greene, *ibid*, 7220

6 M. F. Crommie, L. C. Bourne, A. Zettl, Marvin L. Cohen, and A. Stacy, Phys. Rev. B **35**, 8853; J. Moreland, J. W. Ekin, L. F. Goodrich, T. E. Capobianco, A. F. Clark, J. Kwo, M. Hong and S. H. Liou, *ibid.*, 8856; J. R. Kirtley, R. T. Collins, Z. Schlesinger, W. J. Gallagher, R. L. Sandstrom, T. R. Dinger, and D. A. Chance, *ibid.*, 8846

7 P. W. Anderson, in Novel Superconductivity, Proceedings of the International Workshop on Novel Mechanisms of Superconductivity, Berkeley, 1987, edited by S. A. Wolf and V. Z. Kresin (Plenum, New York, 1987), p. 295.

8 U. Walter, M. S. Sherwin, A. Stacy, P. L. Richards and A. Zettl, Phys. Rev. B **35**, 5327 (1987)

9 P. E. Sulewski, A. J. Sievers, S. E. Russek, H. D. Hallen, D. K. Lathrop and R. A. Buhrmann, Phys. Rev. B **35**, 5330 (1987); P. E. Sulewski, A. Sievers, R. Buhrman, J. Tarascon and L. Greene, *ibid.*, 8829

10 Z. Schlesinger, R. T. Collins, and M. W. Shafer, Phys. Rev. B **35**, 7232 (1987)

11 G. A. Thomas, A. J. Millis, R. N. Bhatt, R. J. Cava, E. A. Rietman, Proceedings of the Eighteenth International Conference on Low Temperature Physics, Kyoto, 1987 [Jpn. J. Appl. Phys. **26**, Suppl. 26-3, 1001 (1987)]. In this work the reflectance in the superconducting state was fit to a long wavelength effective medium theory. A value of the energy gap consistent with weak coupling BCS was found to give the best fit.

12 D. A. Bonn, J. E. Greedan, C. V. Stager and T. Timusk, Solid State Comm. **62**, 383 (1987).

13 D. A. Bonn, J. E. Greedan, C. V. Stager, T Timusk, M. G. Doss, S. L. Herr, K. Kamaras, C. D. Porter, D. B. Tanner, J. M. Tarascon, W. R. McKinnon and L. H. Greene, Phys. Rev. B **36**, 8843.

14 G. A. Thomas, H. K. Ng, A. J. Millis, R. N. Bhatt, R. J. Cava, E. A. Rietman, D. W. Johnson, Jr., G. P. Epinosa, and J. M. Vandenberg, Phys. Rev. B **36**, 846 (1987)

15 G. A. Thomas, private communication

16 Z. Schlesinger, R. T. Collins, M. W. Shafer, and E. M. Engler, Phys. Rev. B **36**, 846 (1987)

17 J. M. Bassat, P. Odier, and F. Gervais, Phys. Rev. B **35**, 7224 (1987)

18 R. T. Collins, Z. Schlesinger, R. H. Koch, R. B. Laibowitz, T. S. Plaskett, P. Freitas, W. J. Gallagher, R. L. Sandstrom, and T. R. Dinger, Phys. Rev. Lett. **59**, 704 (1987)

19 J. Orenstein, G. A. Thomas, D. H. Rapkine, C. G. Bethea, B. F. Levine, R. J. Cava, E. A. Rietman and D. W. Johnston, Jr., Phys. Rev. B **36**, 729 (1987).

20 D. C. Mattis and J. Bardeen, Phys. Rev. **111**, 412 (1958)

21 See for example M. Abramowitz and I. A. Stegun, Handbook of Mathematical Functions, National Bureau of Standards Applied Math Series **55** (1970), formulas 25.4.37 and 25.4.39. See also appendix A.

22 R. T. Collins, Z. Schlesinger, R. H. Koch, R. B. Laibowitz, T. S. Plaskett, P. Freitas, W. J. Gallagher, R. L. Sandstrom, and T. R. Dinger, Phys. Rev. Lett. **59**, 704 (1987)

Part 2: Radio-frequency nonlinear response of charge-density-wave conductors.

The first part of this thesis describes measurements of the linear response of CDW conductors and high-T_C superconductors. Linear response theory provides a straightforward means of extracting physical parameters from any experimental linear response data. The second part of this thesis describes aspects of the novel radio-frequency nonlinear response of the pinned mode in the CDW conductor $NbSe_3$. Nonlinear response is much more varied than linear response. To extract detailed information from a particular nonlinear response experiment, it is necessary to model the experiment by solving a particular nonlinear differential equation. However, all the details may not be of great interest. Recent advances in the theory of nonlinear dynamical systems provide methods of understanding certain general features of the nonlinear response of a particular dynamical systems by solving simple, generic models. In Chapter 5, relevant experimental and theoretical results on CDW transport are discussed. Some concepts from the theory of nonlinear dynamical systems are also introduced.

In Chapter 6, the first observation of complete mode-locking in a CDW conductor is discussed. The experiments were performed on nonswitching crystals of $NbSe_3$. The differential resistance dV/dI in the completely mode-locked state is equal to dV/dI in the pinned state, indicating that the entire volume of the CDW is locked to the ac field. The noise level in the completely mode-locked state is indistinguishable from the noise level in the pinned state. The many-degree of freedom CDW dynamical system apparently collapses onto a surface with few degrees freedom. The dramatic reduction of CDW velocity fluctuations is analyzed in terms of continuous time models and the sine circle map with added noise.

In Chapter 7 the response of switching $NbSe_3$ to combined ac and dc electric fields is discussed. The response is dramatically different from that of nonswitching CDWs. For low frequency ac electric fields, "ac switching noise" occurs. The power spectrum of ac

switching noise is broad band and has amplitude as much as 10 dB larger than the broad band noise associated with dc sliding CDW conduction. In samples driven by combined dc and high frequency ac electric fields, a period doubling route to chaos and related instabilities are observed when the CDW is mode-locked. All instabilities are consistent with the phase slip picture of switching CDW conduction. Mode-locking and associated instabilities in switching CDWs are analyzed in terms of the sine circle map, the logistic map and the theory of noisy precursors.

In Chapter 8 a continuous time model of CDW elasticity is proposed to explain the behavior of the CDW elasticity in the presence of dc, ac and combined ac and dc electric fields. The model is an extension existing models of CDW conduction which assigns degrees of freedom to the impurities that pin the CDW. The model predicts that the elastic constants in the mode-locked state are close to those in the pinned state, consistent with experimental observations. This hardening of the crystal during mode-locking is seen to arise from the strong coupling induced between CDW and lattice degrees of freedom.

5. Introduction to Part 2: sliding CDW transport and the theory of nonlinear dynamical systems

For sufficiently large applied electric fields, some CDWs can be induced to slide. Sliding CDW conduction is a highly nonlinear process. One of the most fascinating aspects of sliding CDW conduction is the ac-dc interference, or mode-locking, which occurs in the presence of combined strong rf and dc electric fields. In the second half of this thesis, several novel features of mode-locking in $NbSe_3$ are explored. Mode-locking is discussed in terms of both specific models of CDW conduction and generic models borrowed from the theory of nonlinear dynamical systems. This chapter provides the background necessary for a discussion of mode-locking in CDWs in Chapters 6-8. Section 5.1 briefly discusses relevant experimental results on sliding CDWs. For more detailed information, the reader is referred to one of the excellent reviews of CDW transport[1,2]. Section 5.2 reviews various models of CDW transport. Section 5.3 reviews relevant concepts from the theory of nonlinear dynamical systems. Section 5.4 summarizes the results of Chapters 6-8.

5.1. Experimental results

$NbSe_3$ is a quasi one-dimensional conductor with three inequivalent conducting chains in its unit cell. As $NbSe_3$ is cooled, two of the chains undergo Peierls distortions to CDW states. The first transition is at 144K , the second at 59K. The third chain remains metallic as low as has been measured. Fig. 5-1 shows the temperature-dependent resistance of $NbSe_3$ for various applied currents below 70K. The lower phase transition manifests itself as a large bump on a background resistance that decreases as temperature is lowered. Monceau et. al.[3] were the first to observe nonlinear dc conductivity in the CDW states of $NbSe_3$. As shown in Fig. 5-1, the height of the resistive bump decreases for increasing

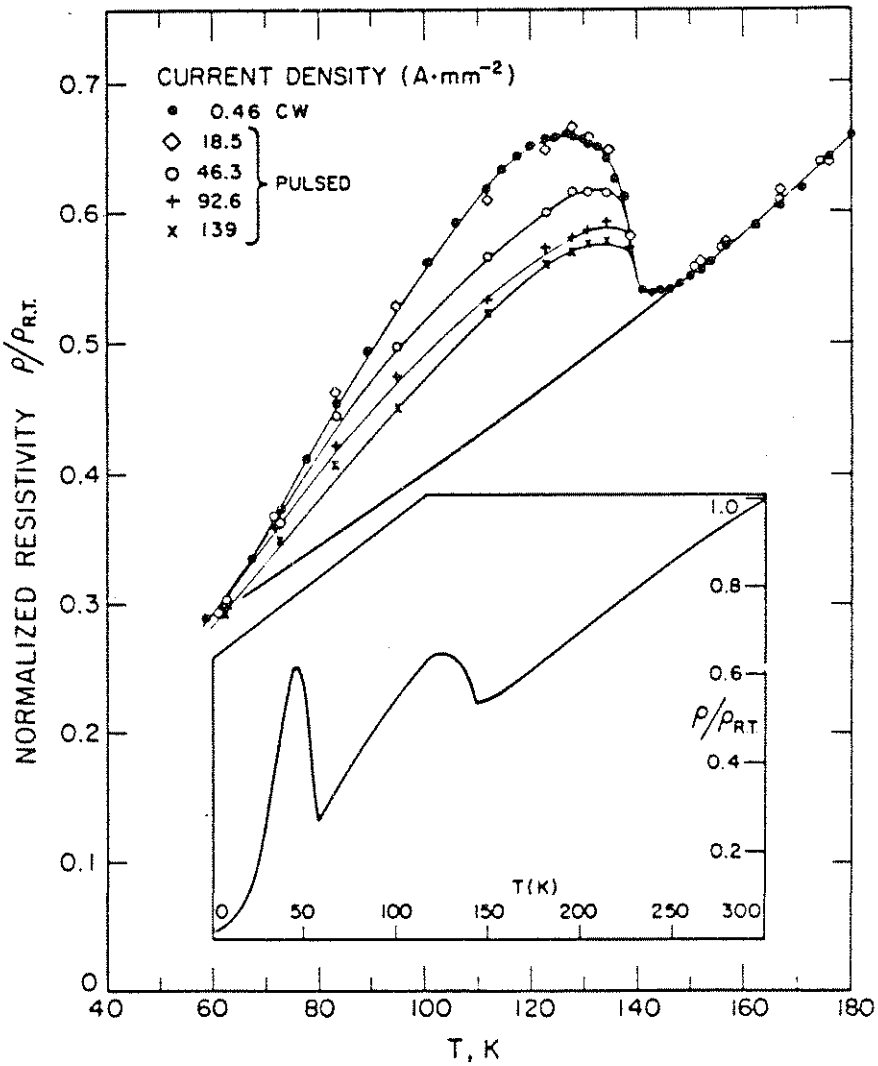

Fig. 5-1: Variation of the normalized dc resistivity of $NbSe_3$ below 70K as a function of temperature at several current densities applied to the sample (from Ref. 3)

applied currents. The enhanced dc conductivity at high currents is attributed sliding CDW conduction.

Fleming and Grimes[4,5] later discovered the existence of a threshold for the onset of electric field-dependent conductivity. Fig. 5-2 shows I-V and dV/dI curves for a typical "nonswitching" sample of $NbSe_3$. For sufficiently low electric fields, the dc conductivity is linear. Nonlinear dc conductivity occurs only above a well-defined threshold electric field E_T. In such conventional samples, the conductivity increases smoothly from the ohmic value as the electric field E is increased above E_T ("Switching samples", to be discussed in Chapter 7, show a different depinning behavior). The differential resistance dV/dI remains always positive. In nonswitching samples of $NbSe_3$ the nonlinear conductivity above E_T is well-described by the empirical expression

$$\sigma_{dc}(E) = \sigma_a + \sigma_b\left(1-\frac{E_T}{E}\right)\exp\left(-\frac{E_0}{E-E_T}\right) \qquad (5\text{-}1)$$

σ_a is the low field dc conductivity, representing the contribution to the dc conductivity of electrons not condensed into the CDW. E_T is the threshold field, and E_0 and σ_b are free parameters. For $E>>E_T$, the conductivity approaches a high-field limit $\sigma_{dc} \approx \sigma_a + \sigma_b$. The threshold field E_T is highly temperature-dependent. The minimum E_T in $NbSe_3$ samples typically occurs near 50K. E_T also depends sensitively on the impurity concentration. In $NbSe_3$, E_T at 50K may vary from 1 mV/cm for extremely pure samples to >100 mV/cm for samples purposely doped with impurities.

A small fraction of $NbSe_3$ samples exhibit threshold behavior radically different than that predicted by Eq. 5-1. These are called "switching" samples[6]. Typical I-V curves for a switching sample of $NbSe_3$ are shown in Fig. 5-3. As the electric field is increased in a switching sample, a small deviation from ohmic behavior often (but not always) occurs at a

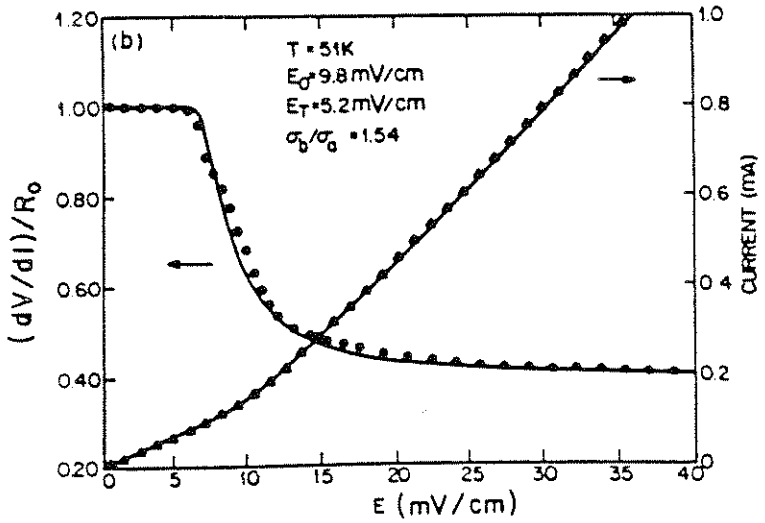

Fig. 5-2: Electric field dependence of the current and normalized differential resistance in the lower CDW state of $NbSe_3$. A threshold field for the onset of nonlinear conduction is clearly observed. The solid lines derived from Eq. 5-1 using parameters indicated on the figure. (from Ref. 5)

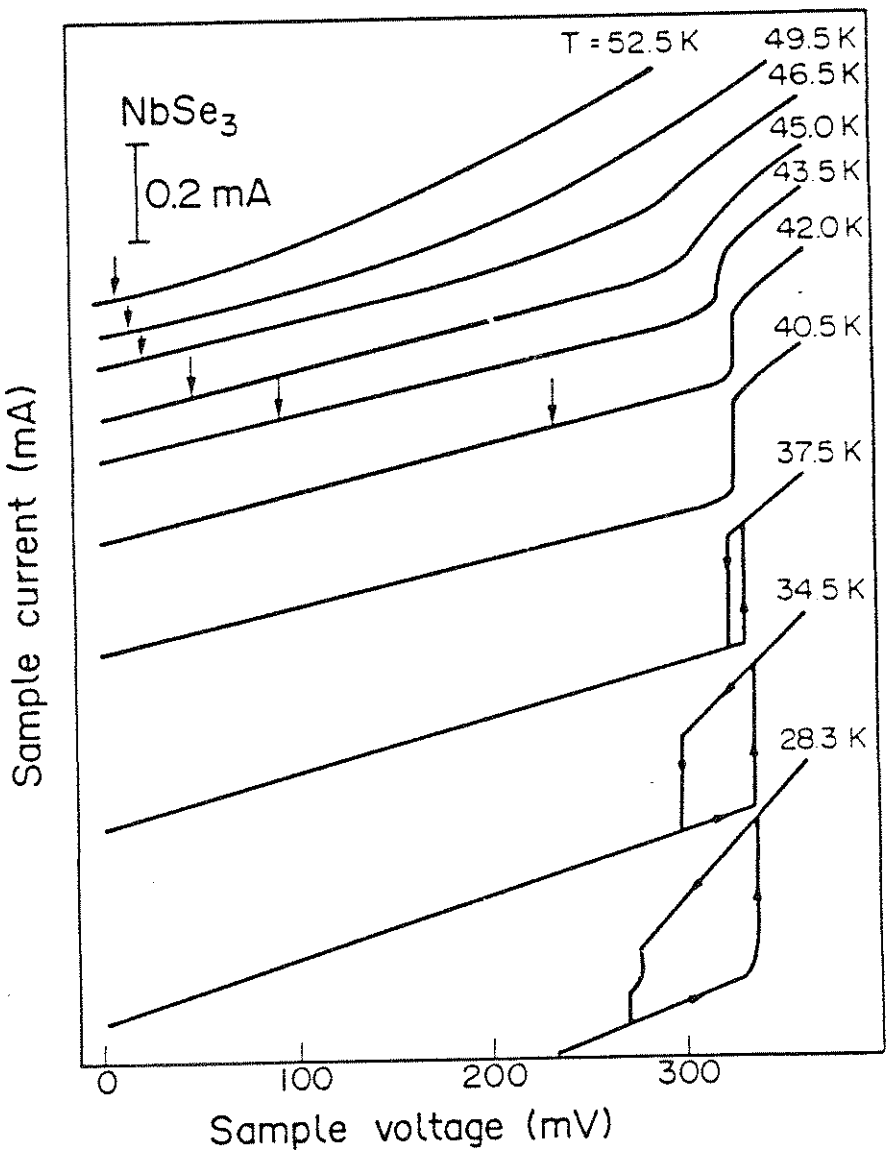

Fig. 5-3: Current-voltage curves (voltage-driven) for a "switching" crystal of $NbSe_3$ at selected temperatures. The initial depinning threshold E_T is indicated by an arrow for temperatures above 42K. Below 40K the I-V curve is hysteretic. (R. P. Hall and A. Zettl, Solid State Commun. **50**, 813 (1984))

lower critical field E_T. At a higher critical field E_C the CDW switches abruptly and often hysteretically from a nearly ohmic state ($\sigma \approx \sigma_a$ in Eq. 5-1) to a state with the high-field conductivity ($\sigma \approx \sigma_a + \sigma_b$ in Eq. 5-1). One or several such "switches" may occur in a single sample. At a given temperature the critical fields E_C in switching samples are three to ten times higher than the threshold fields E_T in nonswitching samples of comparable chemical purity[7].

When the threshold field E_T is exceeded in both switching and nonswitching samples, the sample current becomes time-dependent. For $E>E_T$ so-called "broad band noise" is readily observable in $NbSe_3$ for frequencies less than 100kHz. The broad band noise follows a $1/f^{\alpha}$ frequency distribution[8] with $\alpha \approx 0.8$. In addition to the low frequency broad band noise, coherent oscillations ("narrow band noise") are observed in $NbSe_3$ and other CDW conductors. The frequency of the narrow band noise (NBN) oscillations is directly proportional to the current carried by the CDW, and hence to the velocity of the CDW. For typical experimental parameters, the NBN frequency in $NbSe_3$ is in the 1MHz-50MHz range, though higher and lower NBN frequencies are easily attainable.

The elastic properties of CDW conductors are also strongly electric field-dependent. As first shown by Brill and Roark[9], the velocity of sound in a CDW crystal decreases and the internal friction increases as the electric field is increased above E_T. This phenomenon is discussed in more detail in Chapter 8.

Monceau et. al. [10] and Zettl and Grüner[11] first noted that the application of strong combined ac and dc electric fields leads to a host of phenomena associated with interference between the externally applied ac electric field and the internally generated narrow band noise frequency. The ac electric field reduces the threshold field for sliding CDW conduction. In the sliding state, the narrow band noise frequency is pulled toward rational multiples of the applied ac frequency. When the narrow band noise frequency is sufficiently near a low order rational multiple of the ac frequency (a rational multiple p/q,

where the denominator q is a small integer), the narrow band noise frequency may actually lock onto that multiple of the ac frequency. When such mode-locking occurs, the narrow band noise frequency is independent of dc bias over a small range of dc bias. Since the CDW current is proportional to the narrow band noise frequency, the CDW current is constant during mode-locking. A mode-locked region manifests itself as a step in the I-V curve and a peak in the differential resistance. Typical I-V and dV/dI curves exhibiting mode-locking are shown in Fig. 5-4.

Finally, we make a note on comparing experiment with theory. A CDW crystal may be driven in a voltage-controlled or current-controlled configuration. Theories of CDW conduction treat the CDW as driven with a voltage source and calculate the current. However, because of the relatively low impedance of many CDW crystals, most experiments drive a CDW crystal with a current source and monitor the voltage. In current-controlled experiments the current is divided between the normal electrons (electrons not condensed into the CDW) and the CDW. The normal electrons cause the driving condition on the CDW itself to be in between current- and voltage-controlled. In nonswitching $NbSe_3$, where the conductivity due to the normal electrons is relatively high and the depinning transition is gradual, a current-controlled driving condition for the entire crystal is close to a voltage-controlled driving condition for the CDW. In nonswitching $NbSe_3$, one may thus to good approximation interpret most current-controlled experimental results in terms of a voltage-controlled picture. One simply treats the CDW as driven by the voltage drop across the sample.

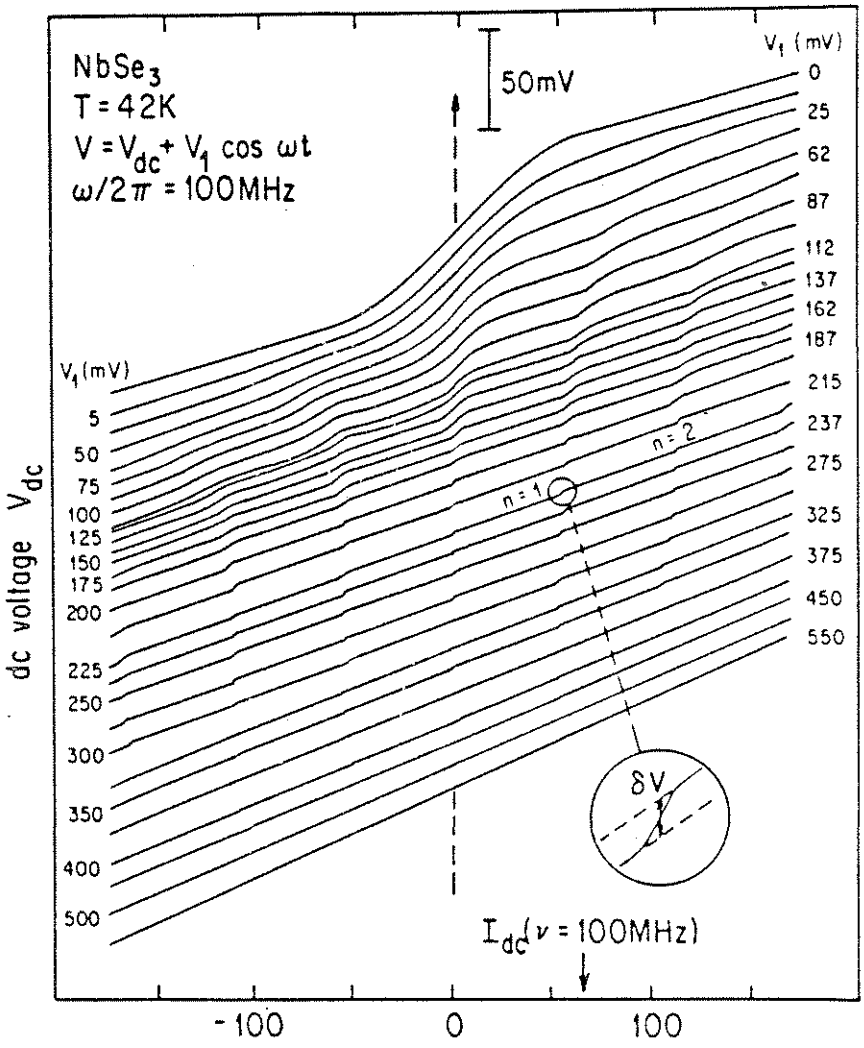

Fig. 5-4a : I vs.V curves for a sample of $NbSe_3$ in the presence of an applied rf field with frequency $\omega/2\pi = 100$ MHz. "Shapiro steps" are clearly visible in the I-V curve for nonzero V_{ac}. (from Ref. 11)

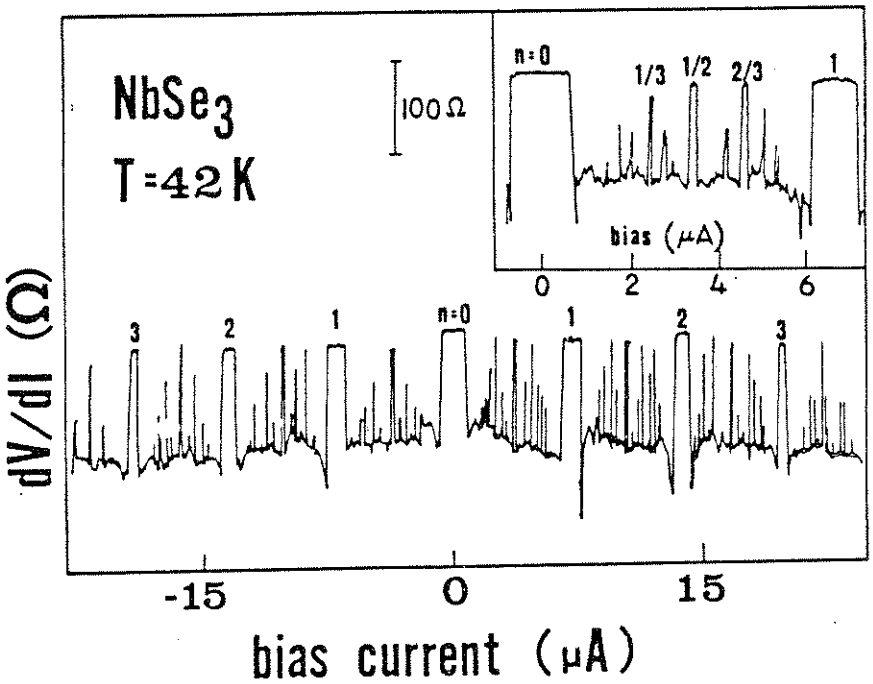

Fig. 5-4b: dV/dI vs. I for a sample of $NbSe_3$ in the presence of an applied rf field with frequency 5 MHz. Both harmonic and subharmonic steps are observed. The inset shows the subharmonics in greater detail. (R. P. Hall and A. Zettl, Phys. Rev. B **30**, 2279 (1984))

5.2. Theoretical models of CDW transport

Both classical and quantum mechanical models have been proposed to explain the novel features of nonlinear CDW transport. The first and simplest model of CDW transport was proposed Grüner, Zawadowski and Chaikin[12] (GZC). The GZC model is isomorphic to the driven damped pendulum, or to the resistively shunted Josephson Junction (RSJ) model. The CDW is treated as a rigid particle in a sinusoidal potential caused by impurities. Even for randomly distributed impurities, the potential must have the period of the CDW wavelength λ: the total energy of the CDW is invariant under a translation by $n\lambda$. The equation of motion is

$$m^*\frac{d^2x}{dt^2} + \gamma\frac{dx}{dt} + eE_T\sin(Qx) = eE(t) \qquad (5\text{-}1)$$

where m* is the effective mass of the CDW, x is the position of the CDW center of mass, γ is a phenomenological damping constant, e is the charge of the CDW, E_T is the threshold electric field, $Q = 2\pi/\lambda$ is the wavevector of the CDW, and E(t) is the applied electric field, which may depend on time. The CDW is so heavily damped that at the frequencies of interest (MHz range), the CDW is treated as massless and the first term on the left hand side of Eq. (5-1) is dropped.

The GZC model qualitatively accounts for many features of the nonlinear behavior of CDWs. It predicts nonlinear conduction with a threshold electric field. For $E>E_T$, narrow band noise occurs as the particle slides through the periodic potential. For combined ac and dc electric fields, mode-locking occurs. Mode-locking also occurs in Josephson Junctions, which may be quantitatively modeled by the isomorphic RSJ model. In Josephson Junctions, mode-locked steps in the I-V curve are called Shapiro steps, and the same name has been adopted in the CDW literature.

The GZC model fails to account for many features of sliding CDW conduction. In a current-regulated experiment, the GZC model predicts a differential resistance dV/dI which is infinite and negative at threshold. In a real experiment, dV/dI is always finite and positive in nonswitching samples. The GZC model predicts no broad band noise for a dc applied electric field. The GZC model with a sinusoidal potential and m*=0 predicts only harmonic Shapiro steps, where the ratio p/q of the narrow band noise frequency to the ac frequency is an integer. In experiments, both harmonic and subharmonic Shapiro steps are observed, with p/q not necessarily an integer. The GZC model does not address the issue of CDW elasticity at all. Finally, the GZC model fails to account for the low frequency ac conductivity and the transient response of CDWs, but these matters are beyond the scope of this thesis.

Agreement between theory and experiment is significantly improved in a class of models which treat the CDW as a classical object composed of many degrees of freedom. These models are all based on a Hamiltonian proposed by Fukuyama and Lee[13].

$$H=\pi v' \int d\underline{r}\left[p^2+\frac{1}{4\pi^2}\left(\frac{v}{v'}\right)^2(\underline{\nabla}\phi)^2+\sum_j V_j\delta(\underline{r}-\underline{R}_j)\cos(\underline{Q}\cdot\underline{r}+\phi(\underline{r}))\right] \qquad (5\text{-}2)$$

where $\phi(r)$ is the slowly-varying phase of the CDW, p is the momentum conjugate to ϕ, V_j is the (random) potential associated with the jth impurity, R_j is the position of the jth impurity, $v' = v^2/v_F$ where v_F is the Fermi velocity and

$$v=\left(\frac{m}{m^*}\right)^{1/2}v_F \qquad (5\text{-}3)$$

where m is the band mass of an electron and m* is the effective mass of an electron condensed into the CDW. The ratio m/m* for $NbSe_3$ in the lower CDW state is of order 100, based on microwave conductivity measurements[14].

An equation of motion derived from a discretized version of the Hamiltonian 5-2, assuming only motion in the z-direction a massless CDW, and replacing the phase ϕ by a position r, is

$$\gamma_0 \frac{dr_j}{dt} + \sum_{ij} K_i(2r_j - r_{j+i} - r_{j-i}) + QV_j \sin(Q(R_j + r_j)) = eE(t) \qquad (5\text{-}4)$$

where r_j is the position of the CDW domain associated with the jth impurity, γ_0 is a phenomenological dampling term, K_i is the spring constant of the spring connecting two particles i sites apart, and V_j is the strength of the potential associated with the jth impurity site.

Fisher[15] has considered a mean field treatment of a three-dimensional model like (5-4). In Fisher's calculation, there is an infinite number of CDW degrees of freedom and the interactions between degrees of freedom have infinite range. The Fisher calculation predicts no divergence in dV/dI at threshold, solving one of the problems that plagues the GZC model. Sneddon has solved analytically an infinite range incommensurate model like Eq. (5-4) The impurities in Sneddon's model all have the same strength, and the spacing between impurities is an irrational multiple of the CDW wavelength. The Sneddon model is a dynamnical version of the Frenkel-Kontorova model, orginally developed to study twinning dislocations[16]. Sneddon finds good agreement with the experimentally observed field- and frequency-dependent conductivity of static and sliding CDWs[17]. Extensive numerical simulations on a one-dimensional model like Eqs. (5-4) have been performed by Coppersmith and Littlewood. They find harmonic and subharmonic Shapiro steps[18]. The transient response of a CDW to an applied current pulse is also nicely reproduced[19], as are low-frequency anomalies in the ac conductivity[20].

The above models all predict that narrow-band noise should vanish in the infinite volume limit. This prediction appears to hold, in that large samples show less noise than

small ones. Numerical simulations of Eqs. (5-4) find no steady-state broad band noise even for a finite number of particles[21]. In the dc sliding state, after an initial noisy transient, a sliding CDW with average velocity $\overline{v}$ always settles into a state in which the motion of each particle is periodic with frequency $\omega=Q\overline{v}$. It has been suggested that the broad band noise is an amplification by the sliding CDW of ambient fluctuations[22]. The long noisy transients observed in simulations of Eq. (5-4) provide a natural mechanism for the amplification of ambient fluctuations[21]. However, the origin of broad band noise is not well understood.

The models based on Eqs. (5-4) treat the CDW as an elastic medium, but neglect the elasticity of the underlying lattice. The impurities in Eqs. (5-4) are completely rigid, and their coordinates R_j are not free to move. Thus none of these equations can address the issue of elastic coupling between the CDW and the lattice.

None of the models discussed in this section are appropriate to switching CDW conduction. The single and many degree-of-freedom models discussed above treat the CDW amplitude as constant and consider only the dynamics of the CDW phase. Switching CDW conduction is associated with a periodic collapse of the CDW amplitude at a phase slip center. The phase slip picture of switching is discussed in Chapter 7.

To conclude this review of the theoretical models of CDW transport, I will briefly discuss the quantum mechanical model of CDW transport championed by Bardeen[23]. In Bardeen's model, the CDW is treated as a macroscopic particle that does not "slide", but tunnels through the impurity pinning potential. This model has been used to successfully reproduce the dc I-V curve, scaling of field- and frequency-dependent conductivity, and harmonic mixing experiments. In many cases, the predictions of the quantum tunneling model are very similar to those of classical many-degree-of-freedom models, although the physics is drastically different. In most of the sections of this thesis on CDW dynamics,

phenomena are described in the language of classical mechanics. A similar analysis should, however, be possible in the language of quantum tunneling theory.

5.3. Nonlinear dynamics

In the past decade, great advances have been made in the study of classical nonlinear dynamical systems[24]. In addition to considering the specific classical models of CDW conduction outlined above, it is fruitful to examine sliding CDW conduction in the context of the modern theory of nonlinear dynamical systems. This section first briefly reviews the description of general nonlinear dynamical systems in terms of low-dimensional discrete mappings. Then the relation between the GZC model of CDW conduction and the sine circle map is discussed as a relevant example. Finally, the relevance of the sine circle map to CDW dynamics is briefly discussed.

Classical nonlinear dynamical systems are naturally described by coupled ordinary differential equations. In general, these systems may be written as

$$\frac{d\underline{x}}{dt} = \underline{F}(\underline{x};\underline{\lambda}) \tag{5-5}$$

where $\underline{x}$ is the state vector of the system and the evolution of the state vector from an initial condition $\underline{x}_0$ is determined by the vector field $\underline{F}(\underline{x};\underline{\lambda})$. The vector $\underline{\lambda}$ is a vector of parameters on which the vector field depends. The solution to Eqs. (5-5) is a trajectory $\underline{x}(t;\underline{x}_0,\underline{\lambda})$. If Eqs. (5-5) are dissipative, then the trajectory will in the limit of long times approach a trajectory $\underline{x}(t;\underline{\lambda})$ that is independent of initial conditions. For a dissipative set of equations, the trajectory $\underline{x}(t;\underline{\lambda})$ will lie in a surface of lower dimensionality than the entire set of differential equations. All equations of concern to us are dissipative.

Generating the unique solution $\underline{x}(t;\underline{\lambda})$ to Eqs. (5-5) in general is a difficult problem requiring lots of computer time. However, it is often the case that knowledge of $\underline{x}(t;\underline{\lambda})$ for

all time is unnecessary. For many applications only the periodicity of the solution is of interest. Eqs. 5-5 may rigorously be replaced by a return map of the form

$$\underline{x}_{n+1} = \underline{F}'(\underline{x}_n;\underline{\lambda}) \tag{5-6}$$

where $\underline{x}_n = \underline{x}(n\tau; \underline{\lambda})$ and

$$\underline{F}'(\underline{x}_n;\underline{\lambda}) = \underline{x}_n(t;\underline{\lambda}) + \int_{n\tau}^{(n+1)\tau} \underline{F}(\underline{x}(t;\underline{\lambda}))dt \tag{5-7}$$

If the trajectory $\underline{x}(t;\underline{\lambda})$ has collapsed onto a low-dimensional surface, then it will in principle be possible, by some nonlinear coordinate transformation, to write the return map (5-6) in terms of a new coordinate vector $\underline{z}$ which has a lower dimension than the original coordinate vector $\underline{x}$. The advantage of a description in terms of discrete mappings is that it is much easier to iterate a map than it is to integrate a differential equation. The Catch-22 is that, as illustrated by Eq. (5-7), it is necessary to integrate the differential equation in order to determine the exact return map. However, many features of the dynamics of a dynamical system may be understood without knowledge of the exact return map. It is often sufficient to study a generic map that is a member of the same class of return maps as the exact return map.

For a concrete example, we consider the GZC model. In terms of dimensionless variables, Eq. (5-1) for $E(t) = E_{dc} + E_{ac}\cos\omega t$ may be written in the form of (5-5):

$$\frac{d\phi}{d\tau} = \psi \tag{5-8a}$$

$$\frac{d\psi}{d\tau} = \frac{1}{\beta}(-\psi - \sin\phi + e_{dc} + e_{ac}\cos\xi) \tag{5-8b}$$

$$\frac{d\xi}{d\tau} = \Omega \tag{5-8c}$$

where $\phi = Qx$, dimensionless time τ is measured in units of $(QeE_T/\gamma)^{-1}$, $\beta = (mQeE_T/\gamma)$, $e_{dc}=E_{dc}/E_T$, $e_{ac}=E_{ac}/E_T$, $\xi=\Omega t$, and $\Omega=\omega/(QeE_T/\gamma)$. The state vector of the system is $\underline{x}=(\phi,\psi,\xi)$, and the vector of parameters is $\underline{\lambda} = (\beta,e_{dc},e_{ac},\Omega)$.

For many parameter ranges, the steady state solutions of Eqs. 5-8 alternate between free running quasiperiodic states and mode-locked periodic states (limit cycles) as a parameter is varied. All trajectories for these parameters are attracted to a two-dimensional torus embedded in the three-dimensional phase space, as shown in Fig. 5-5a. The trajectories lying on the torus may be parameterized in terms of the angles ϕ and ξ. A return map may then be constructed by slicing the torus with a surface of section of constant ξ. The return map is a relation between successive intersections of the orbit on the torus with the surface of section. In this case the return map is a relation between successive values of ϕ separated by intervals of $\tau=2\pi/\Omega$. The one-dimensional return map for the three-dimensional system of equations (5-8) will, for the appropriate parameters, be of the form

$$\phi_{n+1} = \phi_n + G(\phi_n) \qquad (5\text{-}9)$$

where $G(\phi+2\pi) = G(\phi)$. This is a "circle map", a mapping of the circle onto itself. The equivalence of the differential equations (5-8) and the mapping (5-9) has been verified numerically by Bak[25]. A quasi-periodic orbit will, after an infinite number of iterations, fill up the entire circle, as shown in Fig. 5- 5b. A periodic orbit will intersect the circle in only a finite number of points, as shown in Fig. 5-5c.

Some solutions of Eqs. (5-8) are neither periodic nor quasi-periodic, but chaotic. A chaotic trajectory cannot lie in only two dimensions[25]. A chaotic trajectory for a moderately dissipative version of Eqs. (5-8) lies on a "bumpy torus"[26] which is a fractal with a dimension greater than two. To rigorously model a chaotic system, an invertible two-dimensional mapping is required. However, if the system is sufficiently dissipative, a

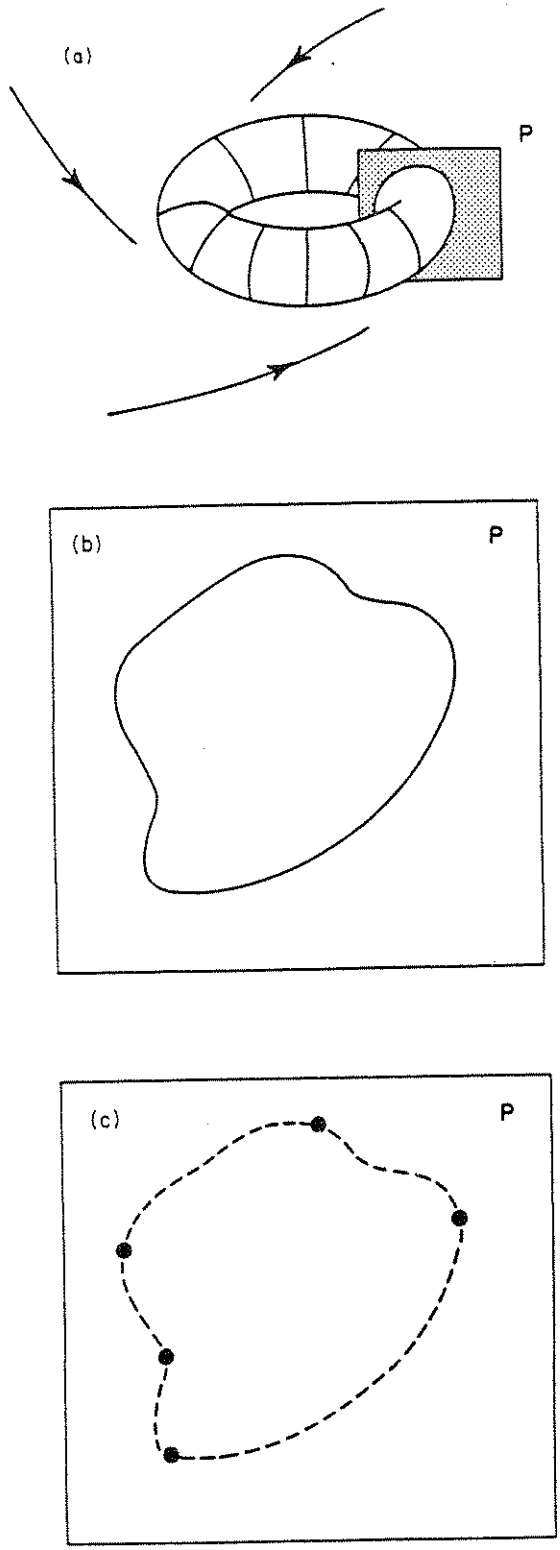

Fig. 5-5: (a) Phase space attraction toward an invariant 2-torus; the Poincaré section P induces an iterative map on the circle. (b) Quasiperiodic dynamics fills in an invariant curve (topologically equivalent to a circle) on P (c) An example of period 5 locked dynamics on P. (from K. Wiesenfeld and I. Satija, Phys. Rev. B **36**, 2483 (1987))

one-dimensional non-invertible map is an approximately correct description. We will restrict ourselves to one-dimensional maps.

The function $G(\phi)$ is difficult to compute. Bohr et. al.[26] have argued that the whole class of maps (5-9) with $G(\phi) = G(\phi+2\pi)$ behave similarly. Thus the simplest version of a nonlinear circle map, the sine circle map has been studied. The sine circle map is

$$\theta_{n+1}=\theta_n + \Omega + \frac{K}{2\pi}\sin(2\pi\theta_n) \qquad (5\text{-}10)$$

where θ is a modulo 1 variable and K parameterizes the nonlinearity. Ω is the "bare winding number". In the case of the GZC model, Ω is the ratio of the internal "narrow band noise" frequency to the frequency of the externally applied ac field. For nonlinearity $K<1$, the solutions alternate between mode-locked and quasi-periodic states. For $K>1$, there are no quasi-periodic solutions, and chaotic solutions are possible. The detailed behavior and predictions of the sine circle map will be discussed as needed in Chapters 6 and 7.

The equivalence of the GZC model to a circle map for certain parameter ranges is well-established. However, the GZC model is only a crude approximation to the dynamics of a real CDW. The extent to which the sine circle map is relevant to CDWs is a controversial matter. The success of the many particle models indicates that a one-dimensional mapping may yield a simplistic description of CDW transport. However, the relevance of a low-dimensional mapping in some circumstances is not ruled out simply because the underlying dynamical system has many degrees of freedom. If for certain parameter ranges the high-dimensional dynamical system collapses onto a low-dimensional subspace, then a low-dimensional mapping may yield useful insights.

References

[1]G. Grüner and A. Zettl, Phys. Reports **119**, 117 (1985)

[2]P. Monceau, "Charge Density Wave Transport in Transition Metal Tri- and Tetrachalcogenides," in P. Monceau (ed.), Electronic Properties of Inorganic Quasi-One-Dimensional Materials, Vol. II, p. 139 (D. Reidel Publishing Company, 1985)

[3]P. Monceau, N. P. Ong, A. M. Portis, A. Meerschaut, and J. Rouxel, Phys. Rev. Lett. **37**, 602 (1976)

[4]R. M. Fleming and C. C. Grimes, Phys. Rev. Lett. **42**, 43 (1979)

[5] R. M. Fleming, Phys. Rev. B **22**, 5606 (1980)

[6] P. Monceau, J. Richard and M. Renard, Phys. Rev. **B25**, 931 (1982); A. Zettl and G. Grüner, Phys. Rev. **B26**, 2298 (1982)

[7]R. P. Hall and A. Zettl, submitted to Phys. Rev. B

[8]J. Richard, P. Monceau, M. Papoular and M. Renard, J Phys. C **15**, 7157 (1982)

[9] J. W. Brill and W. Roark, Phys. Rev. Lett. **53**, 846 (1984)

[10] P. Monceau, J. Richard and M. Renard, Phys. Rev. Lett. **42**, 1423

[11] A. Zettl and G. Grüner, Solid State Commun. **46**, 501 (1982)

[12] G. Grüner, A. Zawadowski and P. M. Chaikin, Phys. Rev. Lett. **46**, 511 (1981)

[13] H. Fukuyama and P. A. Lee, Phys. Rev. B **17**, 535 (1978)

[14] S. Sridhar, D. Reagor and G. Grüner, Phys. Rev. B

[15] D. S. Fisher, Phys. Rev. B **31**, 1396 (1985)

[16] J. Frenkel and T. Kontorova, Journal of Physics **1**, p. 137 (1939)

[17] L. Sneddon, Phys. Rev. Let. **52**, 65 (1984)

[18] S. N. Coppersmith and P. B. Littlewood, Phys. Rev. Lett. **57**, 1927 (1986)

[19] S. N. Coppersmith and P. B. Littlewood, Phys. Rev. B

[20] P. B. Littlewood, Phys. Rev. B (metastable states, dielectric relax.)

[21] P. B. Littlewood, "Sliding CDWs: a numerical study"

[22] S. Bhattacharya, J. P. Stokes, M. O. Robbins and R. A. Klemm, Phys. Rev. Lett. **54**, 2453 (1985)

[23] J. Bardeen, Phys. Rev. Lett. **42**, 1498 (1979); **45**, 1978 (1980)

[24] For a readable primer on nonlinear dynamics, see J. M. T. Thompson and H. B. Stewart, Nonlinear Dynamics and Chaos, (John Wiley and Sons, Somerset, NJ, 1986)

[25] T. Bohr, P. Bak and M. H. Jensen, Phys. Rev. A **30**, 1970 (1984); M. H. Jensen, P. Bak and T. Bohr, *ibid.* 1960.

6. Complete mode-locking and suppression of fluctuations in nonswitching $NbSe_3$

This Chapter investigates further the mode-locking phenomenon in nonswitching $NbSe_3$. Under appropriate conditions of applied dc and rf currents, we find that the CDW phase can be completely mode-locked to the frequency of the external rf drive. The locking persists over well-defined ranges of dc bias current (or dc bias field), and complete harmonic and complete subharmonic locking occurs. Relative to the unlocked state, the broad-band noise power in the completely mode-locked state is suppressed by a factor greater than 400. These observations are discussed in terms of stochastically driven models of sliding CDW conduction.

6.1. Experiment

A two-probe sample mounting configuration was used exclusively, with conductive silver paint contacts. It is easier to achieve complete mode-locking if extremely short samples are used. The sample used for this study was 250μm long. The experiments were performed in a current-driven configuration. The perturbation applied to the sample was a superposition of a dc current and two ac currents. One ac current was of very low frequency (200 Hz) and amplitude, and provided a suitable signal for lock-in detection of the differential resistance of the sample. A Wheatstone bridge circuit was used for this purpose. The second rf current, typically in the MHz frequency range, was the source of the Shapiro step interference. Broad-band noise measurements were obtained by first amplifying the voltage across the sample with a low-noise pre-amplifier (bandwidth .03Hz to 10kHz, gain 10^4), followed by detection with either a sensitive rms voltmeter or a low frequency spectrum analyzer.

Fig. 6-1a shows the differential resistance dV/dI and broad-band noise of $NbSe_3$ at T = 45 K, plotted versus dc bias current I. The threshold current I_T, identified by the sharp bend in dV/dI, also corresponds to the threshold for the onset of broad-band noise. The

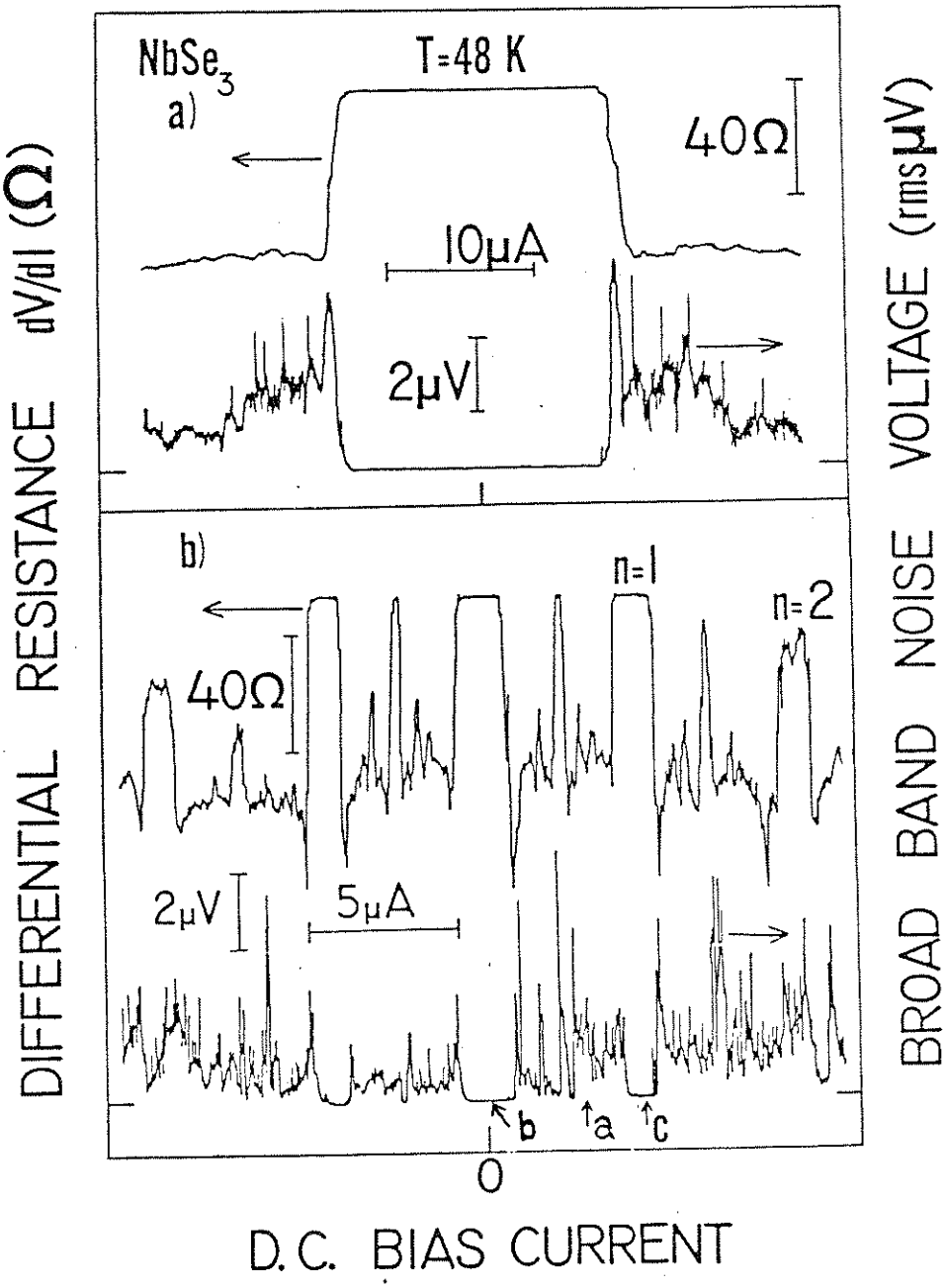

6-1: a) Differential resistance dV/dI and broad-band noise amplitude vs. bias current in $NbSe_3$. The threshold current is indicated with an arrow. b) Same as a), except that an rf current at frequency ω_{rf} = 5MHz has been added to the sample. Complete mode-locking is evident on the step labeled n=1 on the upper trace. All broad-band noise vanishes in the mode-locked regime. The lettered arrows refer to where the corresponding frequency spectra of Fig. 2 were taken.

broad band noise amplitude is a strong function of excess CDW current I_{CDW} and there exists a broad maximum in the noise amplitude for bias currents slightly above I_T. The measurements of Fig. 6-1a are consistent with earlier studies of differential resistance and broad-band noise in $NbSe_3$.[1,2] Fig. 6-1b shows the effect of an externally applied rf current on the differential resistance and broad-band noise of the same $NbSe_3$ crystal. The addition of rf current reduces I_T slightly, although the thresholds for CDW conduction (break in dV/dI) and onset of broad-band noise remain equivalent. The sharp step structure in the upper curve in Fig. 6-1b corresponds to Shapiro step interference, and both harmonic and subharmonic structure is observed. The step labeled n = 1 corresponds to a region where the fundamental narrow-band noise frequency ω_{NBN} equals the externally applied rf frequency, ω_{rf}. The important features of the n = 1 step structure are that the top of the step appears flat over a finite range of dc bias current, and that over this range dV/dI corresponds exactly to the low-field (ohmic) differential resistance. Over the finite range of bias field comprising a step, the velocity (and hence time derivative of the CDW phase) does not change, but remains "locked" to the frequency of the applied rf field. The observation that dV/dI attains its ohmic value on the step confirms that the mode-locking is complete, and involves the entire CDW condensate. This is the first observation of complete mode-locking CDW system. We note that not all interference steps in Fig. 6-1b display complete locking. For example, only one of the subharmonics locks completely (at n = 1/2), and although harmonics equal to or greater than n = 2 show some evidence of locking, they fail to achieve the ohmic value for dV/dI.

The fact that the CDW velocity is "fixed" in the mode-locked states suggests that similar "plateau" structure might occur in the broad-band CDW conduction noise response. A naïve expectation is that the broad-band noise amplitude should remain constant over the whole range of mode-lock, with a value dictated by the (fixed) CDW velocity. This value could be extracted from Fig. 6-1a. The lower trace of in Fig. 6-1b shows, however, dramatically different results. The observed behavior for $NbSe_3$ is that, on a mode-locked

step, the broad band noise power is suppressed by more than a factor of 400, to below our instrumental noise level. Our results are thus consistent with the complete suppression of the broad-band noise. The complete suppression of noise occurs only for those (harmonic or subharmonic) steps which display complete mode-locking; on the n = 2 step in Fig. 6-1b, for example, which shows incomplete locking, the broad-band noise is significantly reduced, but not completely suppressed.

To investigate further the broad-band noise response in the presence of mode-locking, we have measured the frequency spectrum of the noise in the range of 0 - 25 kHz. Fig. 6-2a shows the spectral response for zero applied dc and ac current (the spectra shown here measure the noise amplitude, which is proportional to the square root of the noise power). In this pinned regime, no CDW conduction noise is generated, and only instrumental noise is observed. Fig. 6-2b shows the response for applied dc and rf currents yielding a sliding CDW with incomplete mode-locking. The noise power level here follows a $1/f^{\alpha}$ law, with $\alpha = 1.1 \pm 0.1$, consistent with other studies of broad-band noise[3] in $NbSe_3$. Fig 6-2c demonstrates that when the $NbSe_3$ sample is dc and rf driven to a completely mode-locked step, the spectral response again becomes identical to that of a pinned CDW condensate. At the low frequency end of this figure, the broad-band noise power and hence the effective noise temperature have been suppressed by more than two orders of magnitude! Complete suppression of broad band noise like that in Fig. 6-2c was also observed for the 1:2 mode-locked step.

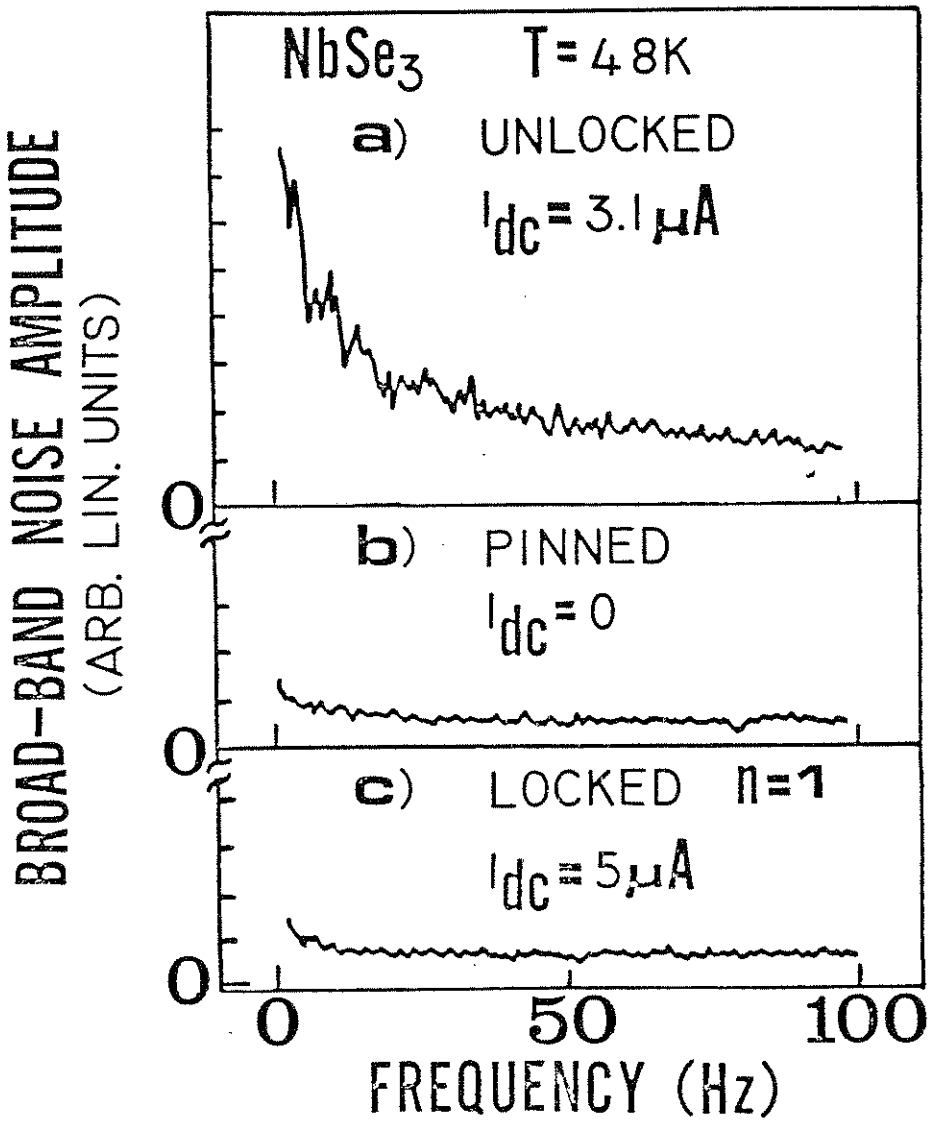

6-2: Broad-band noise spectrum in $NbSe_3$. a) Pinned CDW state; b) a depinned CDW in the presence of an external rf current, but without mode-locking; c) in a mode-locked regime.

6.2. Analysis

This section takes the view that the broad-band noise in CDWs is a nonlinear amplification of external noise. In relation to our experiments, Wiesenfeld and Satija[4] have considered the response to external noise of the sine circle map, the simplest model which exhibits mode-locking. The section begins with a review of their results. The section concludes with a discussion of the extension of the Wiesenfeld and Satija results to many degree-of-freedom models of CDW conduction.

The low value of the noise in the completely mode-locked sliding CDW state indicates that the trajectory of the CDW in phase space is close to a one-dimensional limit cycle. Thus a low-dimensional description of the mode-locked state should be appropriate. Wiesenfeld and Satija have considered the sine circle map driven by external noise.

$$\theta_{n+1} = \theta_n + \Omega + \frac{K}{2\pi} \sin(2\pi\theta_n) + \xi_n \qquad (6\text{-}1)$$

where all variables except ξ are as defined for Eq. (5-). ξ_n is a delta-correlated random variable. In this model, K is always less than 1 and the solutions for ξ=0 are either mode-locked or quasi-periodic.

In a mode-locked state, fluctuations will be damped. For simplicity, consider parameters for which 1:1 mode-locking occurs. All initial conditions will relax to a unique steady state solution $\theta_{n+1}=\theta_n = \theta_0$. A linearized equation may be written for perturbations about the steady state solution:

$$\eta_{n+1} = \lambda\eta_n + \xi_n \qquad (6\text{-}2)$$

where $\theta_n = \eta_n + \theta_0$ and λ is the relaxation rate, which may be calculated by linearizing Eq. (6-1). Stability of the 1:1 fixed point requires $\lambda<1$. The noise ξ is assumed to be small. The fluctuations are damped most quickly for λ close to zero.

In the unlocked case, fluctuations are not damped. If one is only interested in long-time (low-frequency) behavior, the nonlinearity may be ignored to lowest order in the unlocked case. The response of an unlocked state to fluctuations may then be estimated from the equation

$$\theta_{n+1} = \theta_n + \rho + \xi_n \qquad (6\text{-}3)$$

Here $\rho = \langle(\theta_{n+1} - \theta_n)\rangle$ is the "winding number", the average change in θ per iteration of the map. In the context of CDWs, the winding number is the ratio of the narrow band noise frequency to the external drive frequency. The fluctuations in Eq. 6-3 are not damped: the noise kicks provided by ξ accumulate over time and result in a random walk on the circle.

Fig. 6-3 shows the power spectra of θ calculated from digital computer simulations of the nonlinear equations 6-1. The upper trace is the power spectrum for a 1:1 mode-locked state. It shows a noise level significantly higher than that of the lower trace, which is the power spectrum for an unlocked state. The simulation of the nonlinear equation confirms that the approximate predictions of the linear equations (6-2) and (6-3) are correct. Fig. 6-3 is in qualitative agreement with our experimental results that the noise is reduced during mode-locking. However, the 1/f-like behavior of the unlocked power spectrum in Fig. 6-2 is absent in Fig. 6-3. This is because the input noise in the simulations was white noise.

The model of Wiesenfeld and Satija attributes the noise suppression during mode-locking to the relatively short relaxation times that occur in the mode-locked state. Similar arguments may be made for the many degree-of-freedom models, although none of these has been solved in the presence of external noise for the mode-locked case. DC driven many degree-of-freedom models of CDW conduction are known to show long transients with 1/f-like power spectra that eventually relax to a noiseless steady state[5]. In contrast, when the many degree-of-freedom models are driven by a train of periodic pulses, the solutions relax to a mode-locked steady state after only a short transient[6]. The relaxation

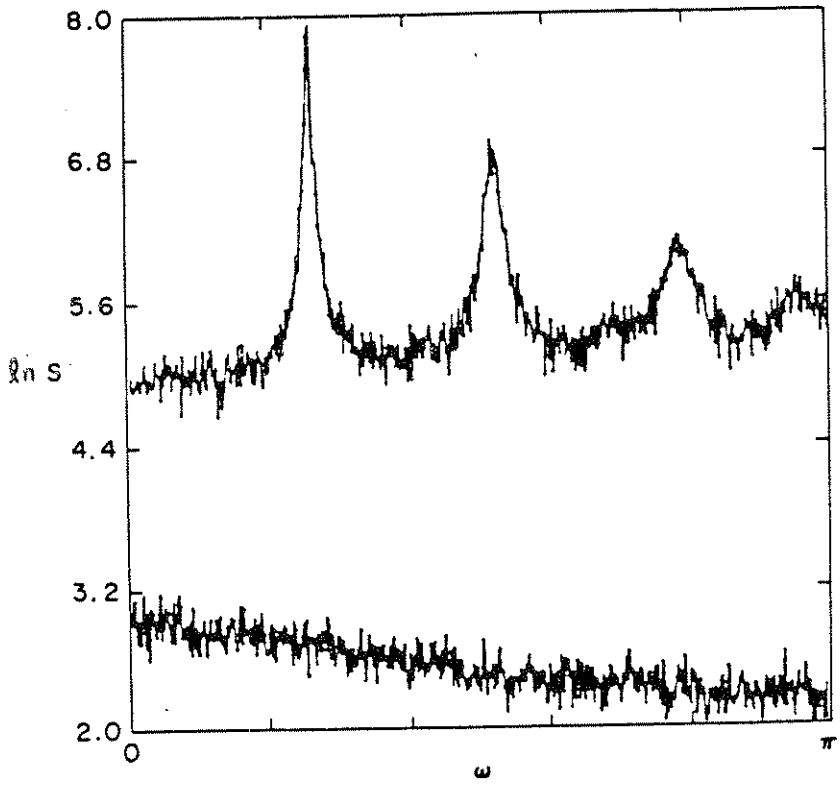

Fig. 6-3: Results of digital simulations of Eq. 6-1. Power spectrum (logarithmic units) vs. frequency for unlocked and locked period-1 cases having the same level of input noise. K=0.8, Ω=0.06 (locked), Ω=0.18 (unlocked), $\langle\xi^2\rangle=1.3\times10^{-4}$. (from Ref. 4)

times to steady state sliding may be orders of magnitude shorter for a train of pulses than for a dc driving configuration . A suppression of noise in the mode-locked state relative to the dc sliding state is plausibly attributed to the vast difference in the relevant relaxation times. Since the length of a transient to the dc sliding state grows with the number of degrees of freedom used, noise suppression in the many degree-of-freedom case is expected to be much larger than in the few degree-of-freedom models, or in the sine circle map.

In summary, we have demonstrated complete mode-locking in the CDW state of $NbSe_3$. The mode-locked state is highly coherent and well-described by a single coordinate. In the language of dynamical systems, the phase space trajectory of a mode-locked CDW lies in a nearly one-dimensional subspace of a high-dimensional phase space. The unlocked or dc sliding trajectories lie in higher-dimensional subspaces. The low dimension of the mode-locked trajectories is attributed to an insensitivity to external noise caused by short relaxation times to the steady state.

References

[1] R. M. Fleming and C. C. Grimes, Phys. Rev. Lett. **42**, 1423 (1979)

[2] J. Richard, P. Monceau and M. Renard, Phys. Rev. B **25**, 948 (1982)

[3] J. Richard, P. Monceau, M. Papoular, and M. Renard, J. Phys. C **15**, 7157 (1982)

[4] K. Wiesenfeld and I. Satija, Phys. Rev. B **36**, 2483 (1987)

[5] P. B. Littlewood, CDWs: a Numerical Study

[6] S. N. Coppersmith and P. B. Littlewood, Phys. Rev. Lett. **57**, 1927 (1986); S. N. Coppersmith and P. B. Littlewood, The Pulse Duration Memeory Effect.

7. Mode-locking and chaos in switching $NbSe_3$.

7.1. Introduction

In typical crystals, CDWs depin smoothly as the electric field is increased above a threshold field[1]. Successful models of such "nonswitching" CDW conduction treat the amplitude of the CDW as rigid and assign degrees of freedom only to the phase of the CDW. However, some CDWs "switch" abruptly and hysteretically from a low conductivity pinned state to a high conductivity depinned state. To successfully model switching CDW conduction, it is necessary to include degrees of freedom for both the amplitude and the phase of the CDW[2]. Switching CDW crystals are thus a unique system in which to study the amplitude dynamics of CDWs. This chapter explores the response of switching CDWs to combined ac and dc electric fields. Recent advances in the theory of nonlinear dynamical systems are essential to understanding the highly nonlinear dynamics of switching CDWs.

Experimental[2,3] and theoretical[4] studies of the response of switching crystals of $NbSe_3$ to dc and small amplitude ac electric fields have been reported elsewhere. The dc response of switching crystals is distinguished from that of nonswitching crystals by the presence of bulk discontinuities in CDW current[5] and by large amounts of CDW polarization below the switching threshold. A CDW velocity discontinuity implies a local, periodic collapse of the CDW amplitude at a phase slip center. It is suggested that switching CDWs are pinned by a sparse distribution of "ultrastrong" impurity pinning centers in addition to the usual weak impurities found in nonswitching crystals.

The small amplitude ac response of switching CDWs is distinguished from that of nonswitching crystals by "motion-dependent inertia." Like the ac conductivity of pinned nonswitching CDWs, the ac conductivity of pinned switching CDWs is overdamped[6]. However, in contrast to the ac conductivity of depinned nonswitching CDWs, the ac conductivity of depinned switching CDWs is underdamped[4]. The underdamped nature of

the sliding state of switching CDW conduction implies a motion-dependent inertia. It is argued that such pseudo-inertia arises naturally in a phase slip model of switching CDW conduction.

This chapter shall explore a series of electronic instabilities that occur only in switching CDWs in the presence of strong combined ac and dc electric fields. The response of nonswitching CDWs to combined ac and dc electric fields has in recent years been the subject of many experimental[7-12] and theoretical[13,14] investigations. The external ac electric field interferes with an internal frequency generated by a CDW as it slides through a periodic impurity pinning potential. When the internal frequency locks to the external frequency (mode-locking), CDW transport becomes highly coherent[10]. The number of degrees of freedom active in nonswitching CDW transport is reduced during mode-locking.

The response of switching CDWs to combined ac and dc electric fields is more complex. For driving frequencies less than 1 MHz, we report the first observation of a characteristic power spectrum which we call "ac switching noise". The power spectrum of ac switching noise consists of a broad band component which is superimposed on sharp peaks at the drive frequency and its harmonics. The broad band component decreases monotonically as a function of increasing frequency and is as much as 10 dB larger than the broad band noise associated with sliding CDW conduction in the same sample. AC switching noise occurs when a sample is driven at low frequency repeatedly through the switch in the I-V curve. No comparable instability is observed in nonswitching samples. AC switching noise is attributed to the unpredictability of the depinning process in switching samples.

For driving frequencies greater than 5 MHz, the phase slip centers[2,5] created during switching CDW conduction appear to synchronize and a qualitatively different regime occurs. The switching CDW mode locks to the radio frequency field, and on each mode-locked step a period doubling route to chaos[15] or related instability is observed. No comparable instabilities are observed in nonswitching CDWs. The period doubling route to

chaos is viewed as the frustrated response of a pseudo-inertial switching CDW which is strongly entrained by the radio frequency electric field.

The period doubling route to chaos is characteristic of systems with few active degrees of freedom[16]. Thus it is reasonable to compare experimental results for mode-locked switching CDWs with the behavior of low-dimensional nonlinear dynamical systems (nonlinear mathematical models with few degrees of freedom). The structure of mode-locking and associated instabilities in switching CDWs are in qualitative and quantitative agreement with the predictions of the one-dimensional sine circle map[17,18]. The period doubling route to chaos in switching CDWs is consistent with the predictions of the logistic map with added noise[19]. Other instabilities are consistent with the theory of "noisy precursors" of dynamical instabilities[20,21]. The agreement between the mode-locking behavior of switching CDWs and the behavior of low-dimensional nonlinear dynamical systems indicates that, as in nonswitching CDWs, the mode-locked state in switching CDWs involves few active degrees of freedom.

The remainder of the chapter is organized as follows. Section 7.2 describes experimental techniques. Section 7.3 describes experimental results on the response of switching CDWs to combined large amplitude ac and dc electric fields. Section 7.4 analyzes the experimental results in terms of the phase slip picture of switching and the modern theory of nonlinear dynamical systems. The chapter concludes in section 7.5 and future directions for this work are discussed.

7.2. Experimental techniques

Three different samples of undoped $NbSe_3$ were used in this study. The samples are numbered #1-#3 The samples were grown by direct reaction of the elements. Samples #2 and #3 were virgin samples which switched without any treatment. Switching was induced in sample #1 by etching in hot, concentrated sulfuric acid[2].

Samples were mounted in a standard two probe configuration with silver paint contacts. Sample #3 was driven in a standard constant-current configuration. Samples #1 and #2 were driven in a constant voltage configuration as shown in Fig. 7-1. In the constant-voltage configuration, all voltages to the sample were buffered by a high-speed voltage follower (Burr-Brown 3553) with a bandwidth of 300 MHz and an output impedance of less than 1 Ohm. The sample response was determined by measuring the voltage across a small resistor R_I in series with the sample ($R_I < R_S/20$, where R_S is the dc resistance of the sample). In all measurements, combined dc and rf voltages were applied to the sample. For differential conductance measurements, a small, low-frequency (≈200Hz) modulation was added to the dc and rf voltages, and detected with a lock-in amplifier. The differential conductance dI/dV was proportional to the output of the lock-in amplifier. Power spectra for frequencies less than 25 kHz were measured with a HP 3582A (FFT) spectrum analyzer. Power spectra for frequencies greater than 0.5 MHz were measured with a HP 8558B (sweeping filter) spectrum analyzer.

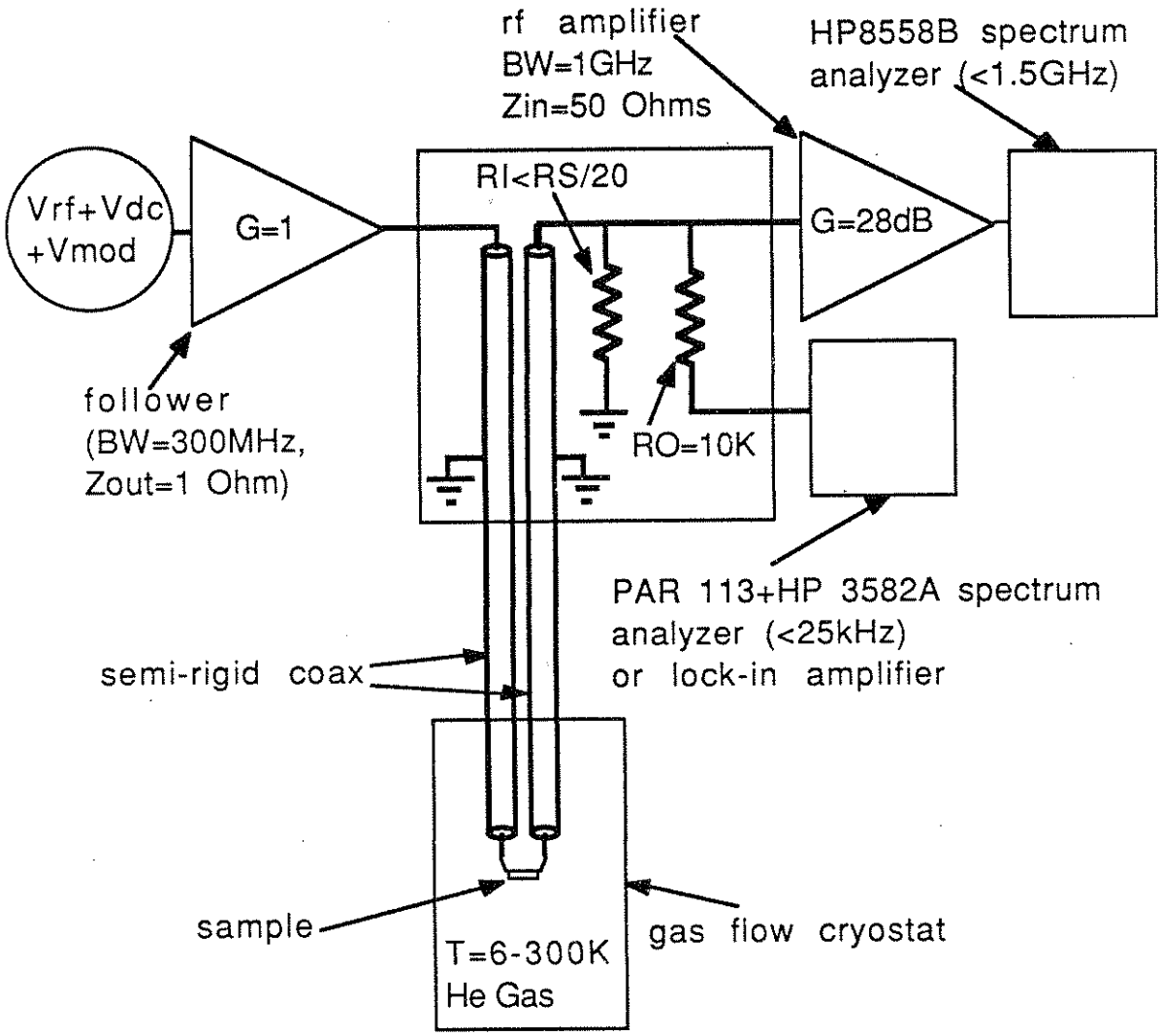

Fig. 7-1- Experimental arrangement for performing a voltage-controlled experiment on $NbSe_3$. The dc resistance of the sample is R_S. The voltage across the small resistor R_I (≈10 Ohms) is proportional to the current through the sample. High-frequency signals are amplified by feeding the voltage across R_I through a short cable directly into a 50 Ohm rf amplifier. Low frequency signals (<100 kHz) are buffered by a 10 K resistor before being fed into a high-impedance lock-in amplifier (for dI/dV measurements) or into a spectrum analyzer through high-impedance preamplifier.

7.3. Experimental results

This section describes the response of switching CDWs to combined ac and dc electric fields. Unless otherwise noted, experiments were performed in a voltage-driven configuration. Section 7.3.1 describes the ac switching noise which occurs for drive frequencies less than 1 MHz. AC switching noise is attributed to an avalanche depinning process. For rf driving frequencies between 1 MHz and 5 MHz, a crossover takes place to a qualitatively different regime of switching CDW dynamics. Section 7.3.2 describes the high frequency regime in which the dynamics are dominated by mode-locking and associated period doubling instabilities. The dynamics in the high frequency regime are attributed to the phase slip process.

7.3.1. AC switching noise

A characteristic power spectrum which we call "ac switching noise" occurs when dc electric fields are combined with low frequency (<1MHz) ac electric fields to drive a sample repeatedly through the switch in the dc I-V curve (The ac and dc electric fields must satisfy the condition V_{ac}-V_{dc}< V_C < V_{ac}+V_{dc}). The power spectrum defined as ac switching noise consists of a broad band component superimposed on sharp peaks which appear at the driving frequency and its harmonics. The broad band component decreases monotonically as a function of increasing frequency. At a given frequency, the noise power of the ac switching noise is as much as 10 dB larger than the noise power of the conventional broad band noise associated with dc sliding CDW conduction in the same sample. The transition from the quiet state to the noisy state is abrupt. There are no precursors such as the period doubling cascade that occurs at higher frequencies in switching NbSe3. AC switching noise is seen for driving frequencies as low as 100 Hz. AC switching noise disappears above the switching onset temperature. Details of the power spectrum of the ac switching noise are shown in Figs. 7-2 and 7-3.

Fig. 7-2 compares on a log-log plot the power spectra of the ac switching noise (top trace) and the conventional broad band noise (bottom trace) in the frequency range 25 Hz to 25 kHz. The traces are not offset. The top trace was recorded for $V_{dc}=V_C$, $V_{ac}=0.37V_C$ and f=0.5 MHz. The noise power in the top trace decreases with increasing frequency. These data are not well fit by a power law. For frequencies between 25 Hz and 250 Hz, the noise power decreases as roughly $1/f^{0.6}$, while between 2.5 kHz and 25 kHz, the noise power decreases more steeply, roughly as 1/f. The bottom trace was recorded under identical conditions as the top trace, except that V_{ac} was set to 0 and V_{dc} was increased 10 % to 1.1 V_C. The ac switching noise in this frequency range is on the average 5 dB larger than the conventional broad band noise for this set of parameters.

Fig. 7-3 compares on a log-linear plot the ac switching noise and the conventional broad band noise between 0.5 MHz to 2 MHz, frequencies comparable to the rf drive frequency. The experimental conditions are identical to those for the power spectra in Fig. 7-2. The magnitude of the noise in the rf driven state is roughly 10 dB higher than conventional broad band noise in this frequency range for this set of parameters.

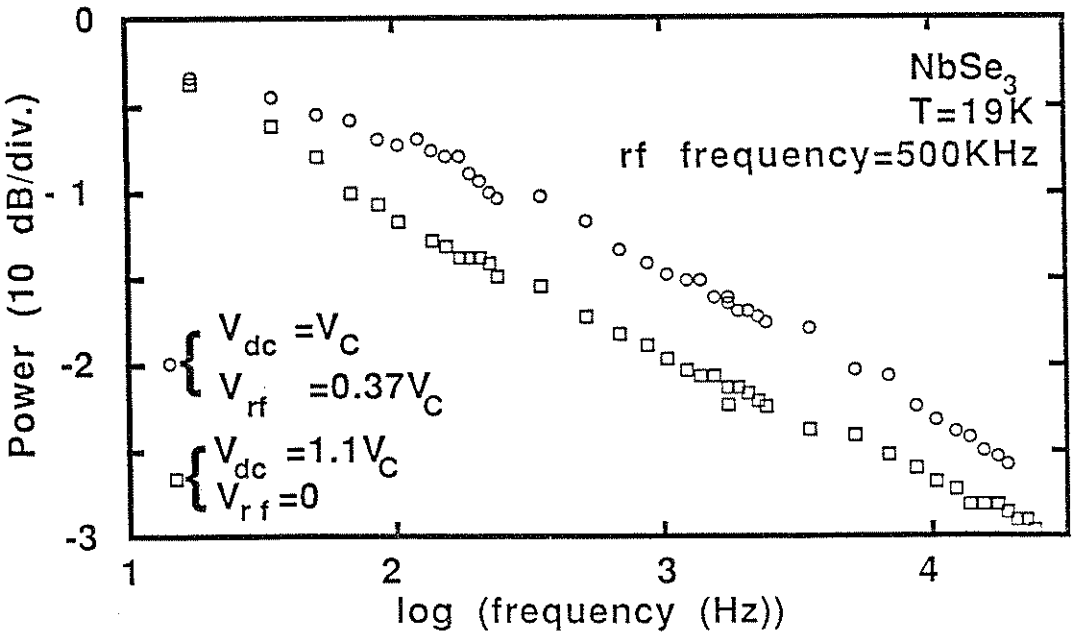

Fig. 7-2- Power spectrum of the current response in sample #1 for frequencies 25 Hz to 25 kHz: ac switching noise (circles) which is an average of 5 dB larger than the conventional broad band noise (squares). AC switching noise occurs when a sample is driven repeatedly through the switch in the dc I-V curve by combined dc and low frequency ac electric fields.

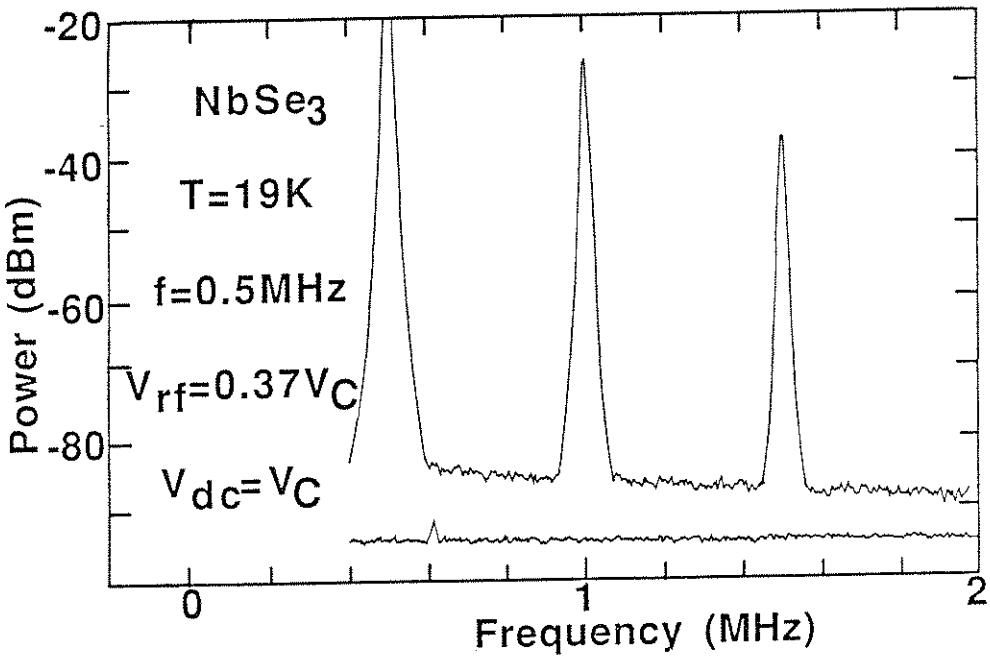

Fig. 7-3- Power spectrum of the current response in sample #1 for frequencies 0.5 MHz to 2 MHz: ac switching noise (upper trace) and conventional broad band noise (lower trace). The experimental conditions are identical to those of Fig. 3. The large peaks in the upper trace at 0.5 MHz , 1 MHz and 1.5 MHz are at the rf drive frequency and its 1st and 2nd harmonics. The width of the peaks is instrumental.

7.3.2. Mode-locking in switching CDWs

This section describes mode-locking and associated instabilities which occur for driving frequencies greater than 1 MHz. Section 7.3.2.1 describes the structure of mode-locking. Section 7.3.2.2 describes the instabilities that occur during mode-locking at temperatures well below the switching transition temperature. Section 7.3.2.3 describes the location of the instabilities in parameter space. Section 7.3.2.4 describes the evolution of the instabilities and of the structure of mode-locking as the temperature rises above the switching transition.

7.3.2.1. The structure of mode-locking

The structure of mode-locking in switching samples is radically different from that of nonswitching samples. In CDW systems driven by combined rf and dc electric fields, mode-locking occurs when the "washboard" frequency (generated as the CDW slides through the periodic impurity pinning potential) is a rational multiple of the rf frequency[7-12]. When a CDW is mode-locked, the I-V curve shows a step, and the dV/dI curve shows a peak. The structure of mode-locking in nonswitching CDWs is illustrated in Ref. 11. For low rf driving amplitudes, the mode-locked steps in nonswitching CDWs are relatively narrow. As the rf amplitude is increased, the width of the mode-locked regions first increases, and then decreases. For any value of rf amplitude, mode-locked peaks in the graph of dV/dI vs. I are separated by wide regions in which the CDW is unlocked and dV/dI is low.

Fig. 7-4 shows a series of I-V curves for a switching CDW sample with a clean, strong switch. As the ac amplitude is increased, steps appear in the I-V curve. On each step, the slope of the curve is approximately equal to the slope of the I-V curve below the switching threshold, indicating that the CDW phase velocity is locked to the frequency of the ac drive and the CDW is on a Shapiro step. For instance, the decreasing dc bias curve for V_{rf}=21 mV shows that the CDW is always mode-locked in the region from about 15 to 30 mV of dc bias. When the dc bias reaches the end of a Shapiro step, the system jumps to the next

step. The jump is hysteretic--it occurs at different values of the dc bias for sweeps of increasing or decreasing dc bias. For a range of values of rf and dc bias, there are no values of dc bias for which the CDW is not locked. This is even more clear in the top traces of Fig. 7-5, in which the (voltage driven) differential conductance is plotted for a different sample in a similar region of parameter space. Mode-locked regions correspond to peaks in differential resistance and hence to troughs in differential conductance. In Fig. 7-5, sharp spikes in the differential conductance curves mark the boundaries between Shapiro steps. However, except for the spikes, the differential conductance for moderate dc bias values above the switching threshold field is always close to the differential conductance for a pinned CDW indicating that the system is always at least partially mode-locked[22].

The lower traces of Fig. 7-4 show that the mode-locked steps take up a smaller fraction of parameter space as rf amplitude or dc bias are increased sufficiently. The Shapiro steps (regions of low differential conductance) are clearly separated by regions in which the CDW is not mode-locked and the differential conductance is higher. The structure of mode-locking in Fig. 7-5 at high values of rf amplitude is reminiscent of that seen in non-switching CDWs at higher temperatures, in which Shapiro steps are always separated by unlocked states. The similarity with higher temperature data is not a heating effect since the average differential conductance is independent of dc bias for all but the highest rf amplitudes.

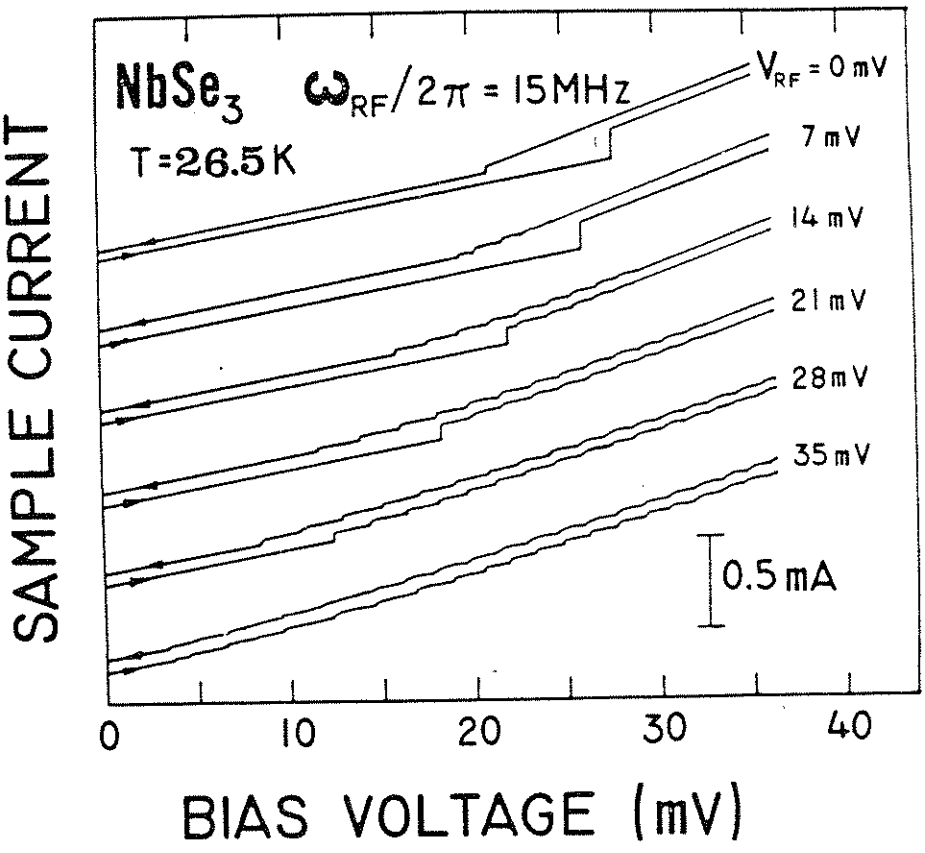

Fig. 7-4- I-V curves for sample #2 in the switching regime. An rf field induces broad, hysteretic Shapiro steps.

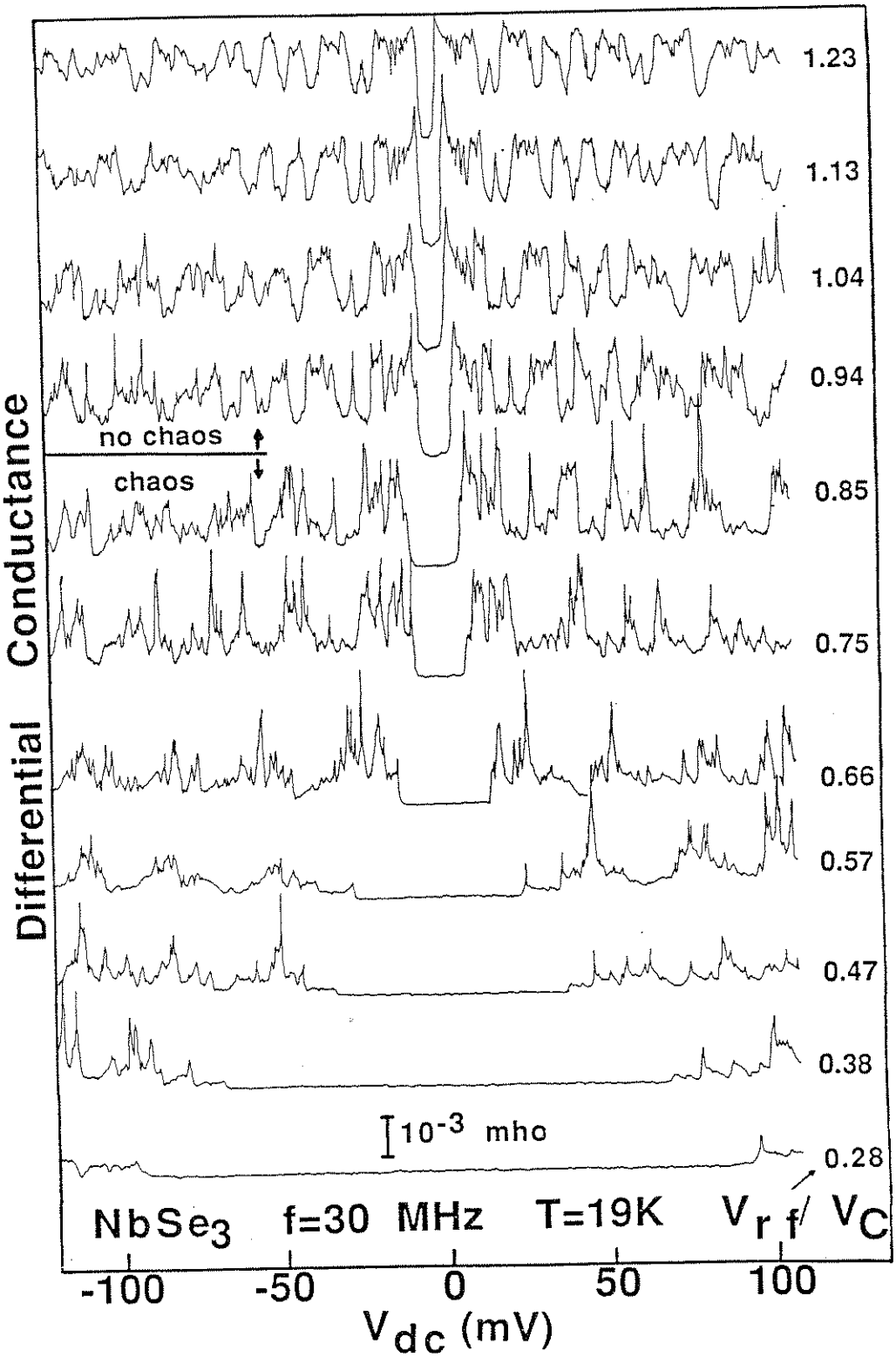

Fig. 7-5- Differential conductance for sample #1 in the switching regime. Arrows parallel to the differential conductance curves indicate the directions of the voltage sweeps. For low rf electric fields, the differential conductance is always close to the V_{dc}=0 value, indicating that the most of the sample is mode-locked for all values of V_{dc}. Sharp spikes indicate transitions from one mode-locked region to the next. For high rf electric fields, mode-locked regions of low differential conductance are separated by unlocked regions of high differential conductance.

7.3.2.2. Instabilities in mode-locking for switching CDWs

In mode-locked nonswitching CDWs, velocity fluctuations with frequency much less than the rf frequency are frozen out during mode-locking[10]. The broad band noise level at frequencies between harmonics of the rf frequency differs little in mode-locked and unlocked cases[12]. In mode-locked switching CDWs, the power spectrum of the CDW velocity for a constant dc bias may show unusual structure between harmonics of the rf frequency. Section 7.3.2.2.1 describes a sequence of power spectra which occur as dc bias is swept along n:1 mode-locked steps. This sequence is interpreted as a period doubling route to chaos. The sequence is nearly periodic in dc bias. Section 7.3.2.2.2 describes other sequences of power spectra, which are also nearly periodic in dc bias. The latter sequences are explained in section IV in terms of the theory of noisy precursors. Section 7.3.2.2.3 describes power spectra characteristic of simple mixing between the rf frequency and the narrow band noise.

7.3.2.2.1. Period doubling route to chaos

The sequence of power spectra identified as a period doubling route to chaos is shown in figure 7a. The temperature, rf frequency and rf amplitude are identical in all these spectra. Only the dc bias was changed within a single Shapiro step. The first spectrum shows only the fundamental of the rf drive frequency f, and harmonics due to the nonlinearity of the system. In the second spectrum, peaks appear at f/2 and its odd harmonics, indicating the first period doubling bifurcation in the period doubling cascade. The third spectrum shows a generally elevated noise level with additional peaks at f/4 and its odd harmonics. In the final spectrum broad peaks centered at f/2 and odd harmonics are 20 dB above the original noise baseline. We identify the latter spectrum as chaos.

In Fig. 7-6b the dc bias dependence of the power spectrum is mapped out for constant rf amplitude and frequency. Near the end of a given Shapiro step the signal is periodic as in Fig. 7-6a.1 (Since there is essentially no space between Shapiro steps and the periodic

spectrum occurs over only a small range of dc bias, it was difficult to determine whether this spectrum occurred at the end of one step or the beginning of the next). The periodic spectrum was followed by relatively narrow regions of period-2 and period-4 spectra and a broad region of chaotic spectra as shown in Fig. 7-6a.4. At the end of a chaotic region, the spectrum again became periodic and the entire sequence repeated itself on the next Shapiro step. The period doubling cascade is thus periodic in dc bias over a large range of dc bias. If the dc bias is increased sufficiently, the mode-locking and period doubling cascades become weaker and eventually evolve into different spectra presented below. The period doubling route to chaos can also be achieved by varying rf amplitude for fixed rf frequency and dc bias.

Not all switching samples exhibit the period doubling route to chaos as clearly as the one shown in Fig. 7-6 (sample #2). For instance, in sample #1, a period 1 spectrum (Fig. 7-6a.1) was unattainable in the range of parameters in which period doubling cascades occurred. At the beginning of a Shapiro step the power spectrum was biperiodic as in Fig. 7-6a.2 and evolved into chaos as dc bias was increased. As dc bias was increased further, the system jumped onto the next step where the spectrum was again period two. Apparently, the hysteretic jump always bypassed the region in which the system was period one.

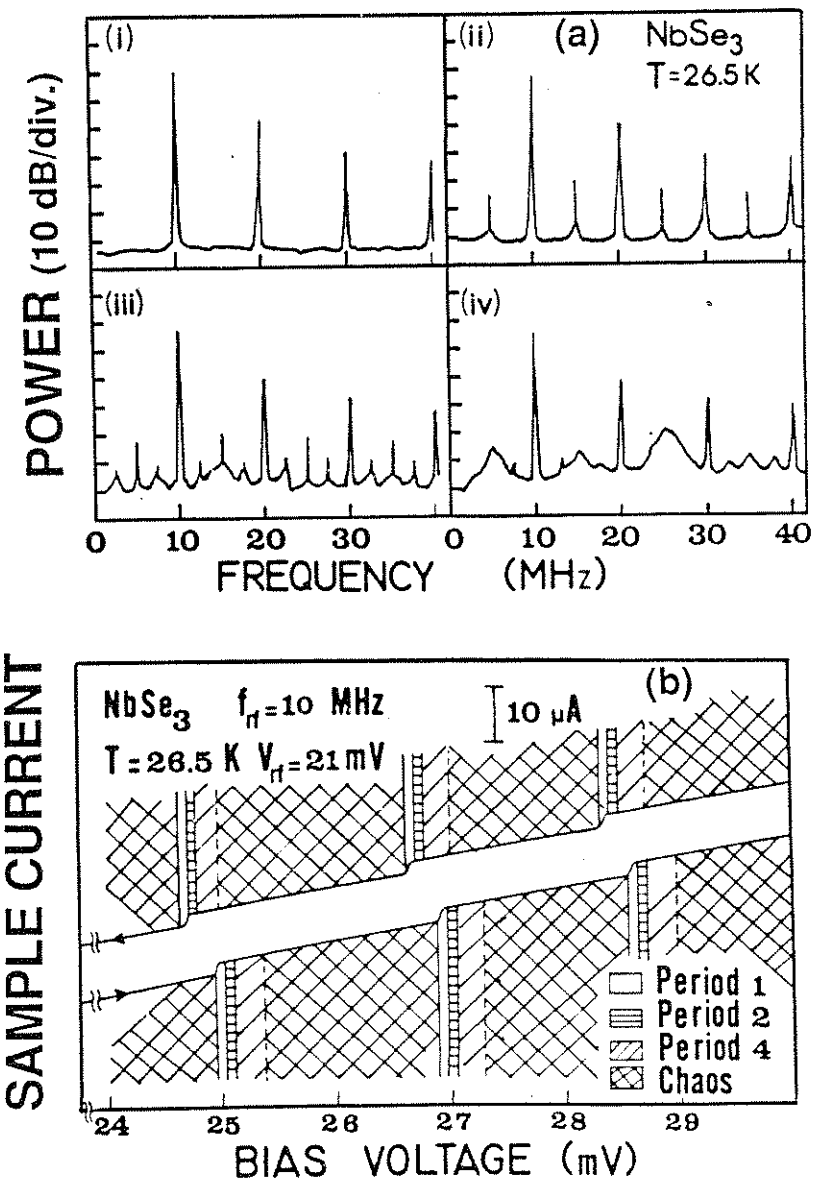

Fig. 7-6. (a)- Power spectra of the current response in the Shapiro step region of sample #2. External rf drive frequency and amplitude as in (b). (i) V_{dc}=25 mV, period 1; (ii) V_{dc}=25.1 mV, period 2; (iii) V_{dc}=25.2 mV, period 4; (iv) V_{dc}=25.5 mV, chaos.(b)- Schematic representation of the periodicity of the current response in the Shapiro-step region for sample #2, for forward- and reverse-bias voltage sweeps.

7.3.2.2.2. Noisy precursors

In addition to the familiar period doubling route to chaos, a number of more unusual sequences of power spectra also occur in switching $NbSe_3$ crystals. In all spectra shown here the dc bias exceeds the switching threshold, and the rf frequency and amplitude are fixed. One characteristic sequence is shown in Fig. 7-7. We identify this sequence as an example of the Virtual Hopf Phenomenon[21] (see Section 7.4.2.1.3). For the lowest dc bias shown (top trace) the spectrum is relatively featureless. As dc bias is increased broad "bumps" appear symmetrically about f/2=10 MHz. These bumps move symmetrically toward 10 MHz, until they become sharp peaks located at approximately f/3 and 2f/3. These peaks broaden again as they move closer to f/2 and finally coalesce into a sharp peak at f/2. For a finite range of dc bias, the power spectrum does not change. Then the f/2 peak suddenly jumps to a lower amplitude and again bumps appear symmetrically about f/2. These bumps now move symmetrically away from f/2 and eventually disappear. As dc bias is increased further, the identical sequence repeats itself. As in the period doubling cascade, the sequence of power spectra is nearly periodic in dc bias.

A related sequence of power spectra is shown in Fig. 7-8. We call this sequence "period two with excess noise". In this series the bottom trace represents the smallest value of dc bias. The spectrum for the bottom trace shows only a sharp peak at f/2=10 MHz. As dc bias is increased, the amplitude of this peak shrinks continuously until the spectrum changes discontinuously to that shown in the third trace from the bottom, where the peak at f/2 has grown by 23 dB and broad symmetric structure appears on the flanks of the f/2 peak as well as near the sides of the trace. As the dc bias is increased further, the symmetric structure first smoothly increases and then decreases in magnitude while remaining at the same frequency. Finally, the spectrum changes discontinuously to that of the top trace of Fig. 7-8, which is virtually identical to the bottom trace. Like the sequence in Fig. 7-7, this sequence is nearly periodic in dc bias over a broad range of dc bias for constant rf amplitude and frequency.

In the course of sweeping through the large parameter space available in this experiment, spectra such as those depicted in Fig. 7-9 occurred occasionally. Fig. 7-9a shows a power spectrum with a sharp peak at f/2=5 MHz and broad peaks symmetrically located at intervals of f/8 about the central peak. Fig. 7-9b shows a power spectrum with broad peaks at intervals of f/6.

7.3.2.2.3. Mixing

There are also V_{rf}-f combinations for which none of the above instabilities occur. In these regions of parameter space, only a weak mixing between the narrow band noise and the rf field is observed. At a given dc bias, peaks occur at the narrow band noise frequency f_{nbn}, at the rf frequency f and its harmonics, and at the sum and difference frequencies $nf \pm f_{nbn}$ (n an integer). As dc bias is swept, the narrow band noise and sum and difference frequencies move through the spectrum but no behavior obviously different than simple mixing is observed. (For a more extensive description of mixing in CDWs, see Ref. 23)

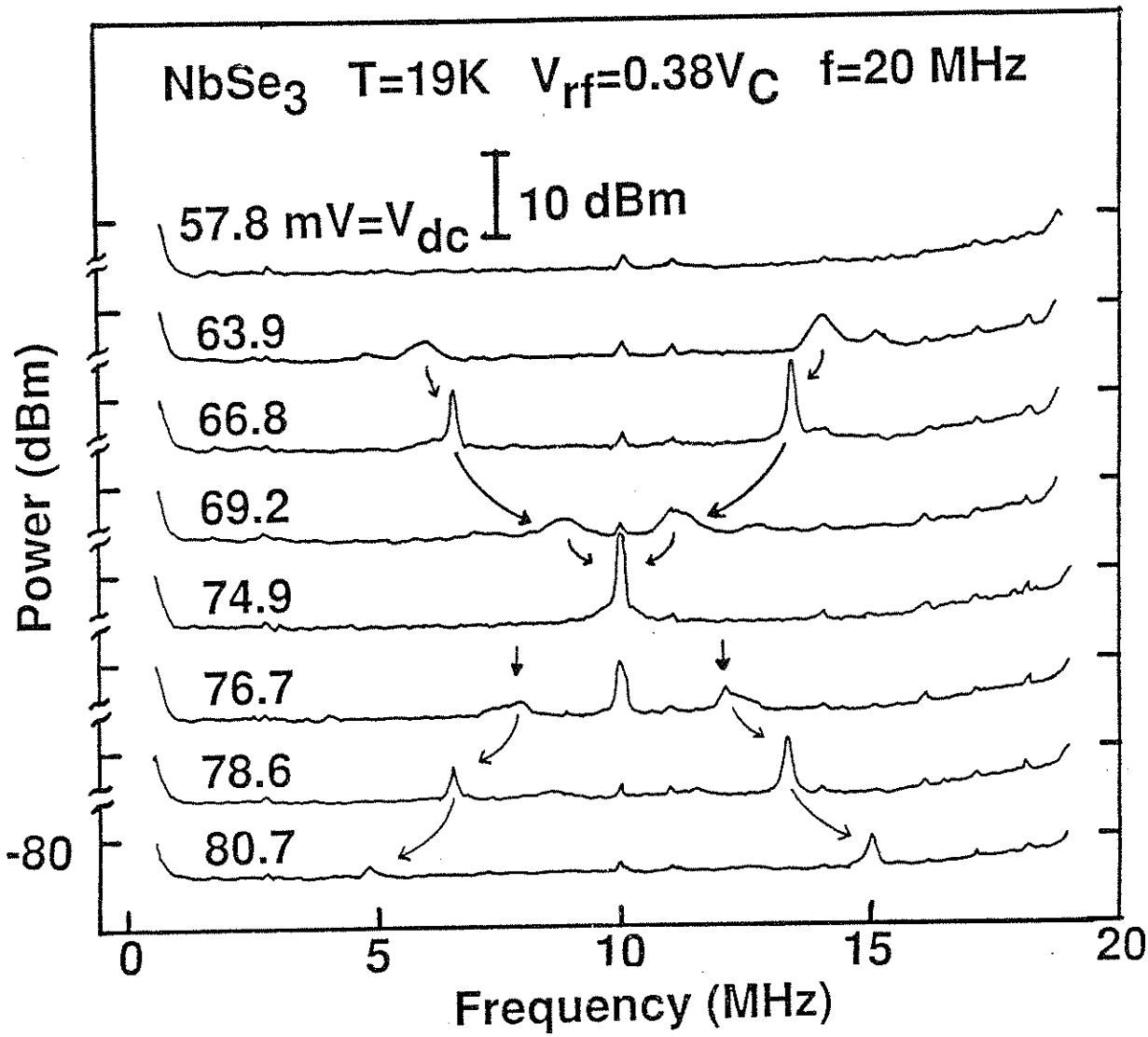

Fig. 7-7- Sequence of power spectra of the current response of sample #1 for different dc biases at fixed rf amplitude and frequency. The dc bias increases from the top trace to the bottom trace. This sequence is nearly periodic in dc bias. This sequence is identified as an example of the "Virtual Hopf phenomenon" (see text, sections 7.3.2.2.2, 7.4.2.1.3). The power spectra are offset, and each "tic" on the vertical axis is at -80 dBm. The critical field V_C for this sample was 150mV. The power levels in Figs. 8-10 may be compared with one another as they were recorded for identical amplifier gains and spectrum analyzer bandwidths.

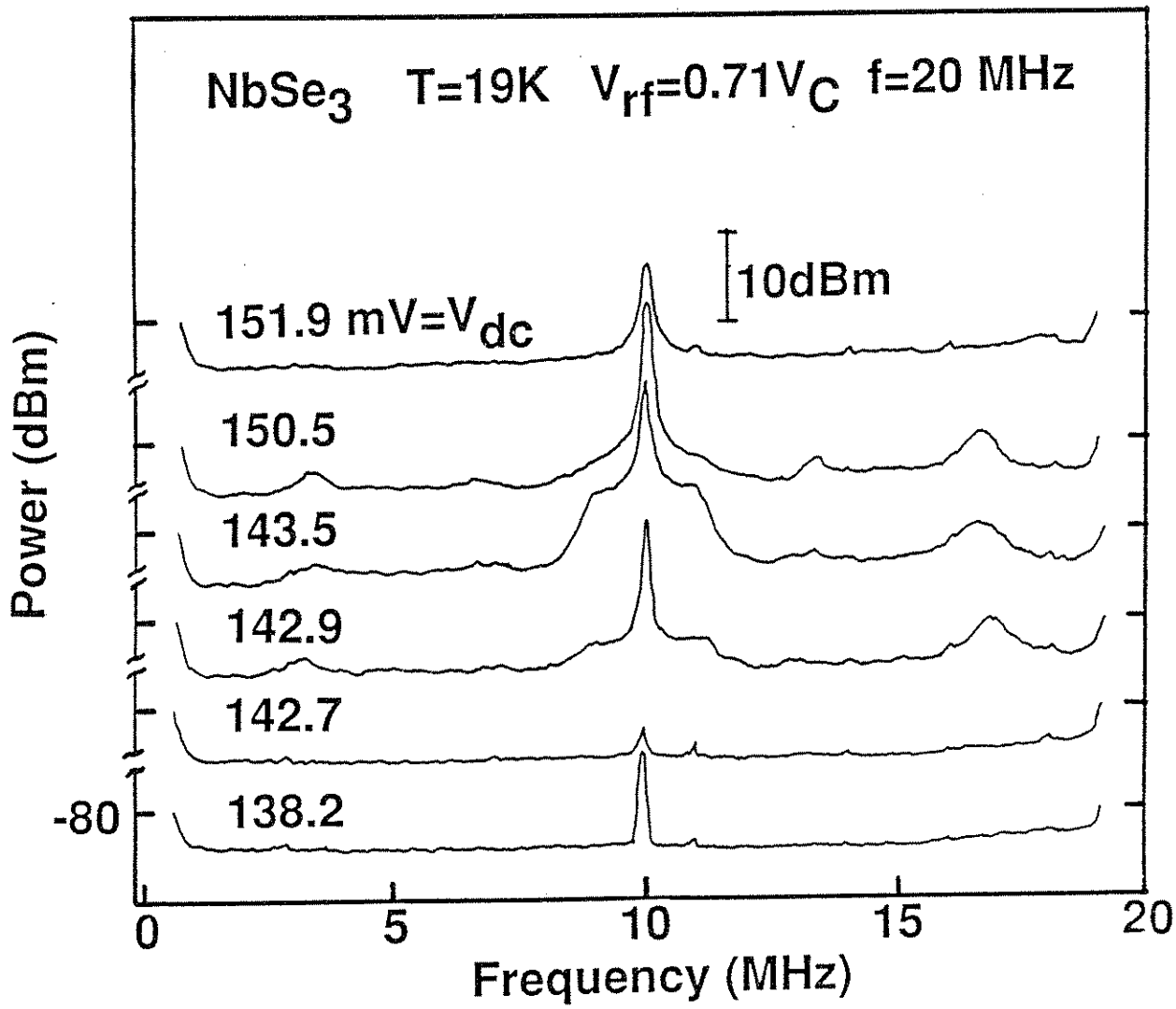

Fig. 7-8- Sequence of power spectra of the current response of sample #1 for different dc biases at fixed rf amplitude and frequency. The dc bias increases from the bottom trace to the top trace. This sequence, like the sequence in Fig. 8, is nearly periodic in dc bias. We call this sequence "period two with excess noise".

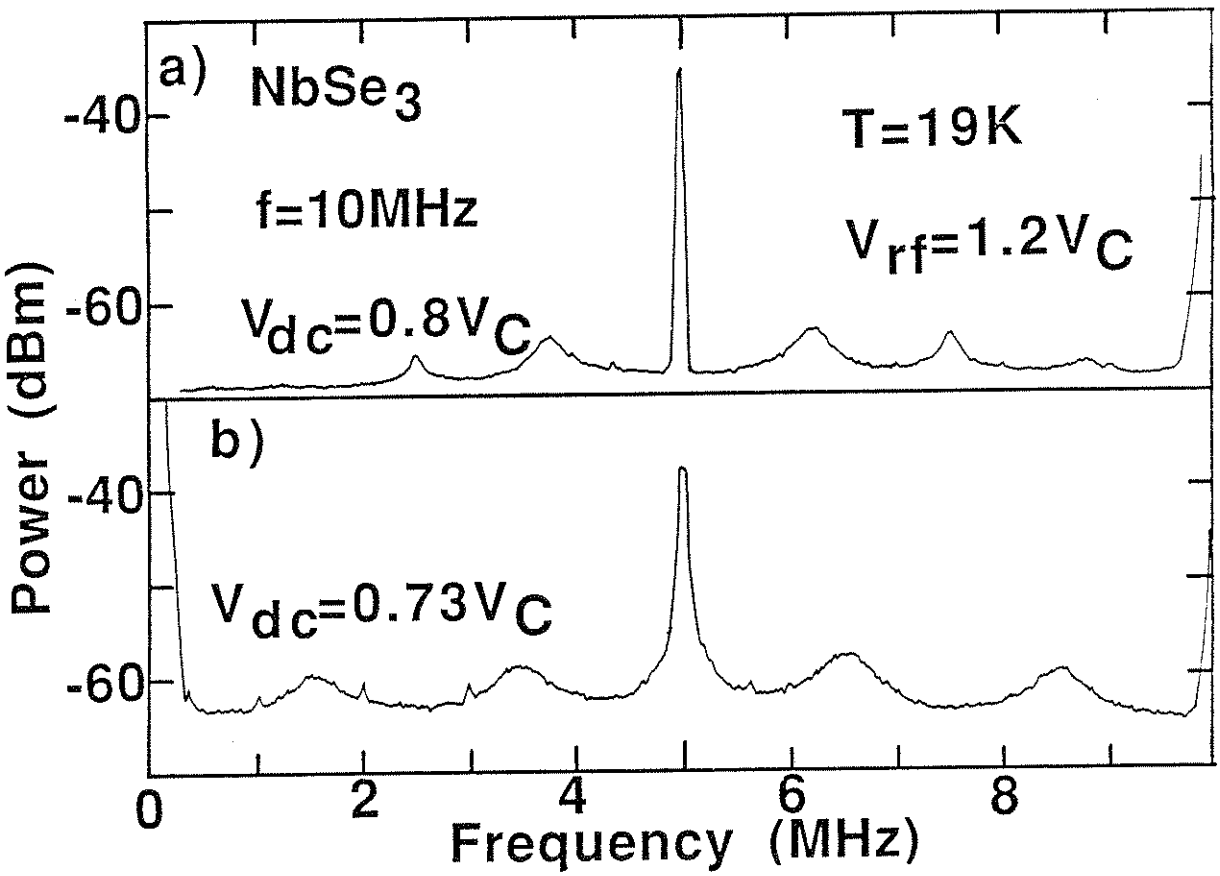

Fig. 7-9 - Power spectra of the current response of sample #1. (a) period 6. (b) period 8. These power spectra are observed occasionally and do not fit into any clear sequence.

7.3.2.3. Location of the period doubling and noisy precursor instabilities in parameter space.

This section describes the location in parameter space of the period doubling and noisy precursor phenomena. The boundaries of the instabilities described above are convoluted two-dimensional surfaces in a three dimensional parameter space. We present projections of these surfaces into three different two dimensional parameter planes.

Fig. 7-10 maps out a region in which period doubling occurs in the rf amplitude-dc bias plane. For these experiments, sample #3 was current-driven and the driving frequency was held constant at 35 MHz. The boundaries of this plot were determined by sweeping dc bias at constant rf frequency and amplitude and marking the onset and disappearance of the first period doubling instability . Because of the relatively high temperature at which these experiments were conducted, the period doubling cascade never developed into chaos. Fig. 7-10 shows a threshold rf amplitude above which period doubling is possible. As rf amplitude is increased, the dc threshold for the first period doubling instability decreases. On application of a strong rf electric field, a similar suppression of the CDW depinning threshold occurs in nonswitching samples[24]. A substantial suppression of V_C is also evident in Figs. 5, 6 and 15. The shape of boundary in Fig. 7-10 is similar for all of the instabilities that are periodic in V_{dc} (i. e. , the instabilities described in Section 7.3.2.2). The only qualitative difference is that for some parameter ranges there is an attainable upper Vrf threshold above which the instability no longer occurs. The shape of the boundary is also similar for voltage and current driven cases.

Fig. 7-11 maps out a region in which period doubling occurs (again, in current-driven experiments on sample #3) in the rf frequency-dc bias plane. Fig. 7-11 was constructed in exactly the same manner as Fig. 7-10, except that here the rf amplitude was held constant at $I_{rf}/I_C = 0.71I_C$. In this case the period doubling boundary closes on itself, and there are upper and lower limits in dc bias and rf frequency for the first period doubling instability. As the rf frequency is increased, the lower dc bias threshold for period doubling increases.

A similar trend is also seen in the study of ac-dc interference in nonswitching CDWs. As the rf frequency increases for constant rf amplitude, higher narrow band noise frequencies are required for mode-locking to occur and a given n:m mode-locked step moves to higher dc bias values.

The most revealing way in which to map the parameter dependence of the instabilities in mode-locking is as a function of rf amplitude and frequency, as is done in Fig. 7-12. By varying the dc bias at fixed rf amplitude and frequency it is possible to observe a number of different power spectra, as shown in section 7.3.2.2. We define a ranking of the observed power spectra in order of proximity to the chaotic state:

1) mixing

2) Virtual Hopf (Fig. 7-7)

3) period two (Fig. 7-6a.2)

4) period two with excess noise (Fig. 7-8)

5) period four (Fig. 7-6a.iii)

6) chaos (Fig. 7-6a.iv).

In order to generate Fig. 7-12, rf frequency and amplitude were fixed and dc bias was swept until the power spectrum closest to chaos (as defined in the above ranking scheme) was observed. Consider the system at a point in the frequency-amplitude plane such that the period doubling route to chaos depicted in Fig. 7-6 is possible. That point is marked chaotic in Fig.7-12, even though period one, two and four behavior as well as chaos are observed for some values of dc bias. The boundaries drawn in this plot are only approximate, as the instabilities evolve continuously from one type to another.

The behavior of switching CDWs at low temperatures may be summarized using Fig. 7-12 as a guide.

1. For driving frequencies less than 1 MHz, on the left-hand edge of the figure, ac switching noise occurs for $V_{dc}-V_{ac}<V_C<V_{dc}+V_{ac}$. Note the power spectrum we call ac switching noise (Fig. 7-3) is qualitatively different than the power spectrum we call

chaos (Fig. 7-6a.iv). The power spectrum of ac switching noise decreases monotonically between harmonics of the ac driving frequency. The power spectrum of chaos shows broad bumps centered half way between harmonics of the ac driving frequency.

2. For frequencies between 1 MHz and 5 MHz ac switching noise becomes mixed with a period doubling route to chaos. AC switching noise is not observed for frequencies greater than 5 MHz.

3. For frequencies between 5 MHz and 30 MHz, a full period doubling route to chaos may occur for sufficient rf amplitude. The first simple period doubling instability occurs for rf amplitudes greater than approximately $V_C/10$. As rf amplitude is increased further, period two with excess noise (Fig. 7-8) occurs. For yet higher rf amplitude a period 4 instability occurs. Finally, for rf amplitudes greater than $0.4V_C$ the full period doubling route to chaos is observed . For frequencies between 5 and 15 MHz, a period doubling route to chaos is observed for the highest rf amplitudes that will not damage the sample. For frequencies between 15 MHz and 30 MHz, increasing the rf amplitude causes the system to exit the region in which the full period doubling route to chaos occurs. As rf amplitude is increased further, the system first enters a region with only a Virtual Hopf sequence. Finally, the system enters a region where only mixing occurs.

4. Above 30 MHz, the period doubling route to chaos is no longer observed for any rf amplitude. Between 30 and 70 MHz, the most nonlinear behavior is the Virtual Hopf behavior sequence of Fig. 7-7.

5. Above 70 MHz, only mixing observed.

Fig. 7-12 was constructed for sample #1, but the shape of this plot is similar for different switching CDW samples.

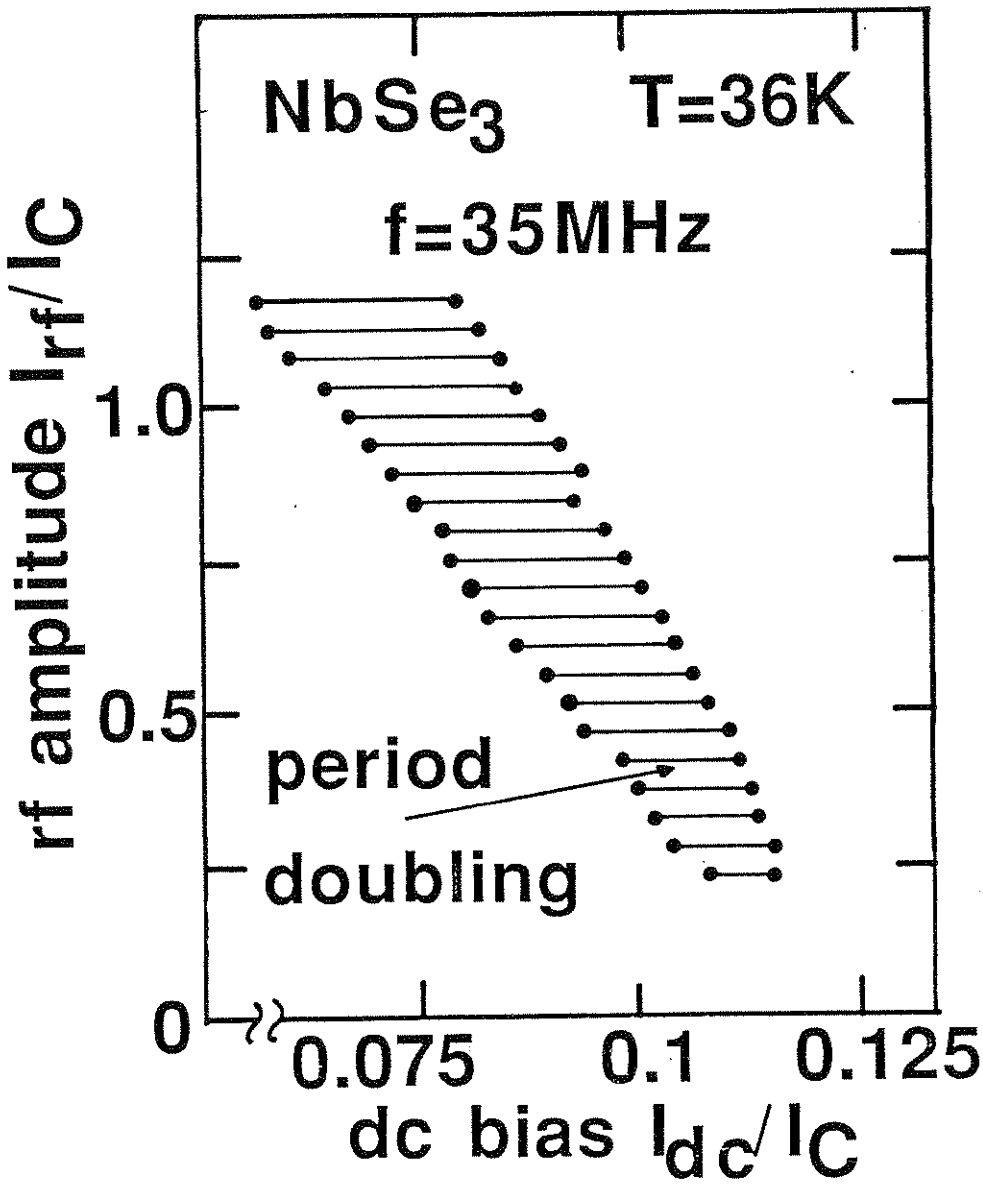

Fig. 7-10- First period doubling region in the dc bias- rf amplitude plane for sample #3. The figure was constructed by sweeping dc bias forward for rf frequency f=35 MHz and various rf amplitudes. The filled circles mark the sudden appearance and disappearance of a strong peak at f/2 in the power spectrum.

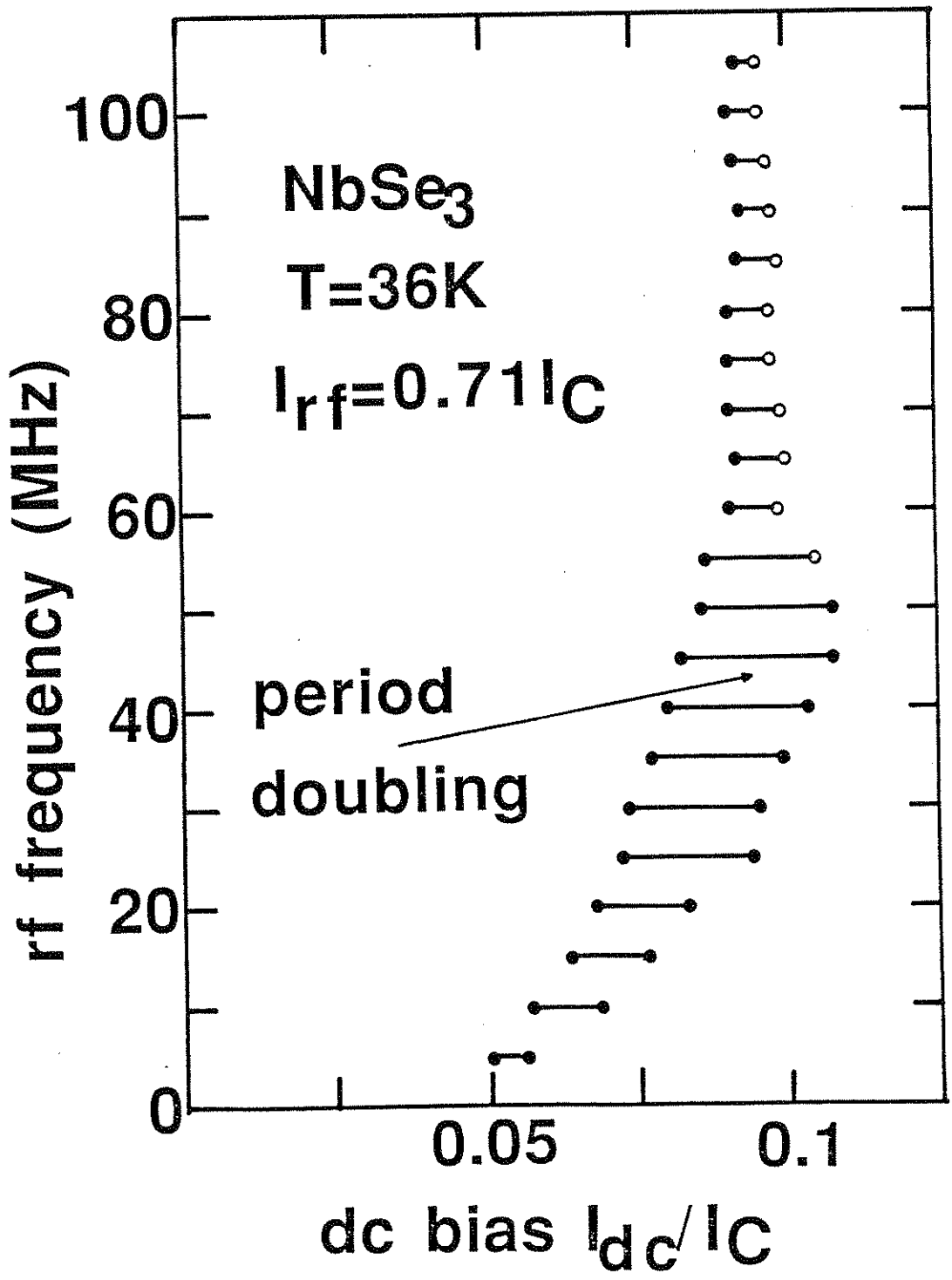

Fig. 7-11- First period doubling region in the dc bias-rf frequency plane for sample #3. The figure was constructed by sweeping dc bias forward for rf amplitude $I_{rf}=0.71I_C$ and various rf frequencies. The filled circles mark the sudden appearance and disappearance of a strong peak at f/2 in the power spectrum. For high values of the rf frequency, the f/2 peak was not much above the instrumental noise level. The open circles mark the dc biases at which the f/2 peak gradually faded into the instrumental noise.

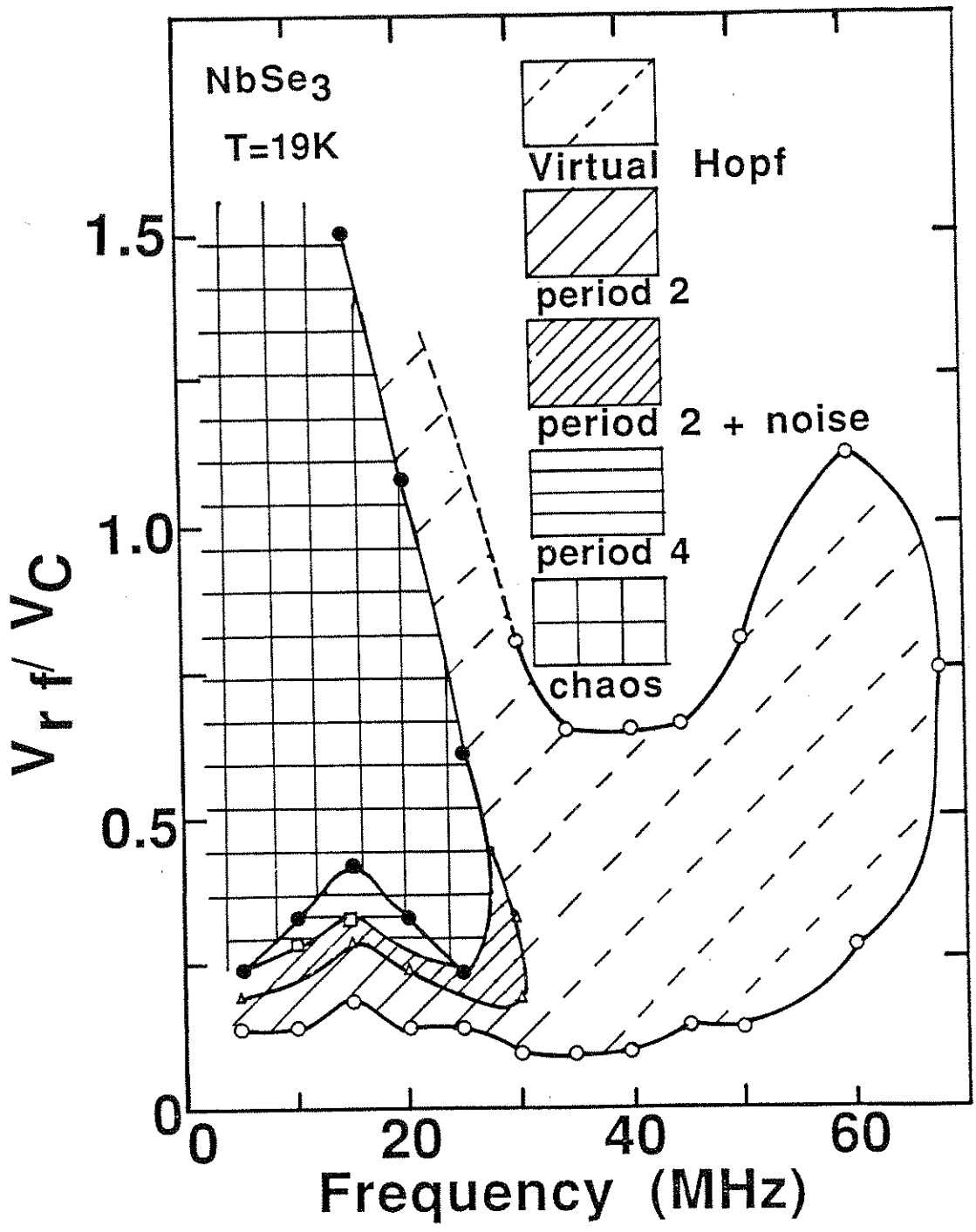

Fig. 7-12- Location of the instabilities described in Figs. 7-6 to 7-8in the rf-frequency - rf-amplitude plane for sample #1 for $T < T_{switch}$. The symbols are spaced at 5 MHz intervals and mark the values of rf amplitude at which one type of instability is replaced by another. The lines are guides to the eye.

7.3.3. Instabilities for T>Tswitch

Just above the switching onset temperature, a number of instabilities disappear. The ac switching noise, which is directly associated with a low frequency rf field driving the CDW repeatedly through the switch, is no longer present. Neither is a full period doubling route to chaos observed. However, period 2 and period 4 instabilities, as well as the virtual Hopf (Fig. 7-7) and period two with excess noise (Fig. 7-8) are still observed. Fig. 7-13 locates these instabilities in rf frequency-rf amplitude space. Fig. 7-13 was constructed in the same manner as Fig. 7-12, but for T = 37K instead of T = 19K. The boundaries in Fig. 7-13 are similar to those in Fig 7-12, except that certain instabilities no longer appear.

The differential conductance at 37K for a series of rf amplitudes for rf frequency 50 MHz is shown in Fig. 7-14. This figure should be compared with Fig. 7-5. For V_{rf}=0, simple CDW depinning is observed. As V_{rf} is increased, troughs develop in the differential conductance, signifying the onset of mode-locking. As V_{rf} is increased further, period doubling instabilities are observed. The mode-locked regions become broad for intermediate values of V_{rf}, filling most of the available range of dc bias at $V_{rf}\approx 0.1V_C$. As V_{rf} is increased further, the mode-locked regions become narrower and period doubling occurs less frequently. Finally, for $V_{rf} \approx 0.4V_C$, the differential conductance is high over most of the available range of dc bias, and period doubling occurs not at all. There are two sets of interference troughs in this sample (most clearly visible in the high V_{rf} data), indicating the presence of two domains with different velocities.

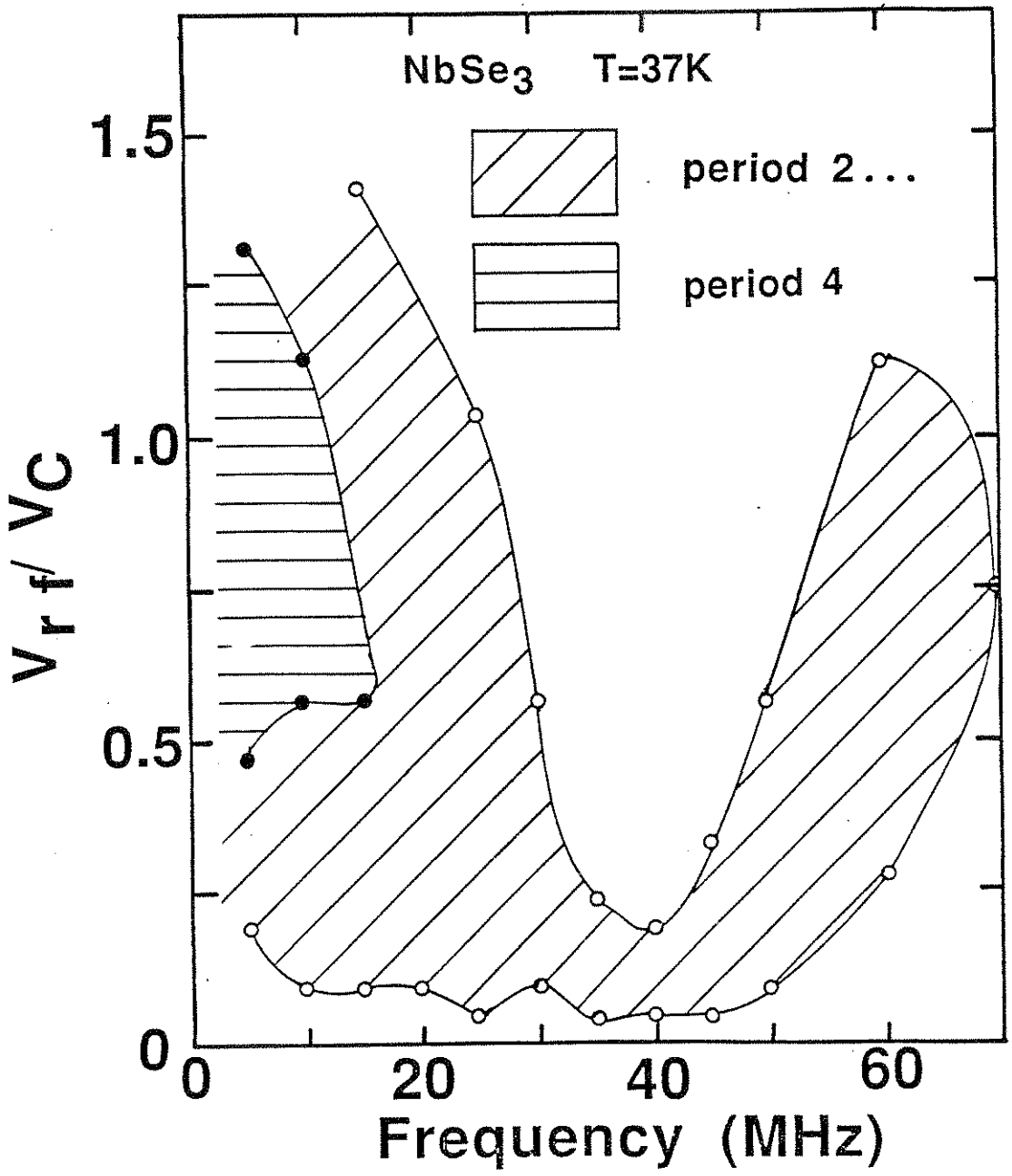

Fig. 7-13- Location of the instabilities described in Figs. 7-9 in the rf-frequency - rf-amplitude plane for sample #1 for $T > T_{switch}$. The region marked "period 2 . . ." exhibited period two, period two with excess noise and Virtual Hopf behaviors.

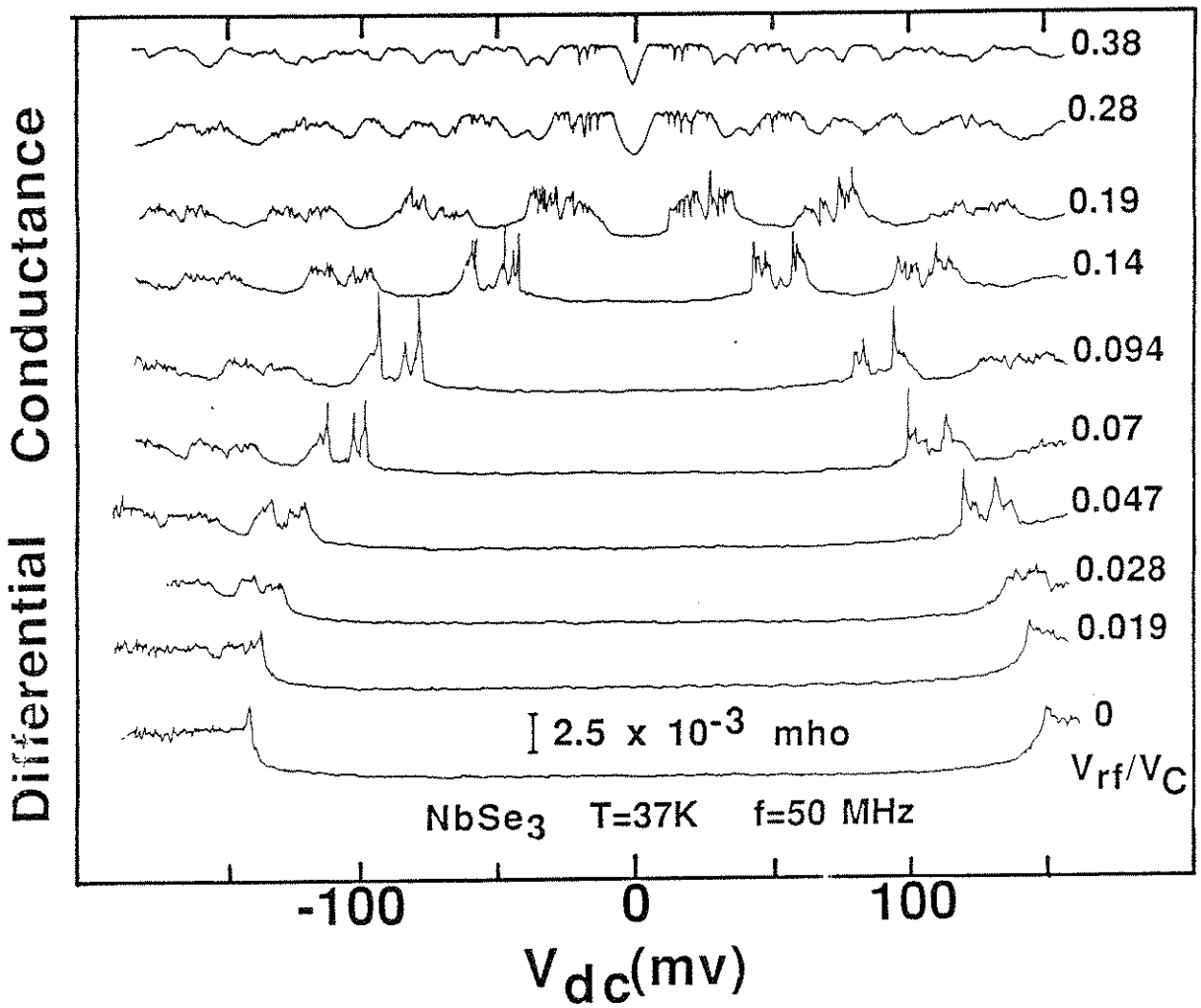

Fig. 7-14- Differential conductance vs. dc bias for sample #1 for $T > T_{switch}$. All voltage sweeps are from left to right.

7.4. Analysis

The Results section of this chapter has described a number of unusual instabilities that occur only in switching crystals of $NbSe_3$. In this section these instabilities are analyzed in terms of the phase slip picture of switching, using simple mathematical models borrowed from the modern theory of nonlinear dynamical systems. A phase slip model of switching was proposed in Ref. 2. Anomalies in the ac conductivity of switching CDWs are explained in terms of a phase slip model in Ref. 3. Theoretical details of a phase slip model, and extensive simulations of a differential equation proposed to describe the phase slip process, are to be found in Ref. 4.

According to the phase slip picture of switching[1,4,25], in crystals which show switching at low temperatures, the CDW is pinned by sparsely distributed ultrastrong-pinning centers as well as conventional, weaker impurities. For electric fields below a critical electric field E_C, the CDW becomes heavily polarized, but the ultrastrong-pinning centers prevent it from sliding . The CDW switches and begins to slide only when the polarization energy is sufficiently large to cause the CDW amplitude to collapse at the strongest pinning centers. When the amplitude collapses, the CDW phase advances by a multiple of 2π, partially relieving the CDW polarization and allowing the CDW amplitude to increase again from zero. However, the CDW polarization rapidly builds up again, causing another amplitude collapse and phase slip. Once the critical field has been exceeded, the CDW advances by periodic slips of the CDW phase. The average pinning force due to the ultrastrong pinning centers collapses as the electric field is increased above the critical value. Thus, once it depins, the CDW slides with a rapid velocity, comparable to that it would have for the same electric field in the absence of strong pinning centers.

The instabilities observed in switching samples of $NbSe_3$ can be divided into low- and high-frequency categories. The low-frequency instabilities are the large 1/f noise and intermittency associated with negative differential resistance [26,27], and ac switching noise

(analyzed in section 7.4.1). The low frequency instabilities are attributed not to the details of the phase slip process, but to the complex dynamics of many asynchronous phase-slipping domains. The high-frequency instabilities are the period doubling and related instabilities associated with mode-locking (analyzed in section 7.4.2). The high frequency instabilities are attributed to the dynamics of synchronized phase-slipping domains. The mathematical formalism used to describe the instabilities in mode-locking is the sine circle map, which has been used in recent years as a paradigm of mode-locked systems (Section 7.4.2.1). The physical basis for the observation of period doubling and related instabilities in mode-locked switching CDWs is the motion-dependent inertia associated with the phase slip process (Section 7.4.2.2).

7.4.1. AC switching noise

AC switching noise occurs when a sample is driven through the switch in the dc I-V curve at frequencies less than 1 MHz. These frequencies are low on the scale of typical narrow band noise frequencies (1-100 MHz), and on the scale of the crossover frequency in the ac conductivity (50 MHz). It is thus reasonable to model ac switching noise in the dc limit, ignoring dynamical effects such as entrainment or motion-dependent inertia. In the dc limit, there are two possible contributions to an increase in the broad band noise level when the sample is repeatedly driven through the switch in the I-V curve. If the sample is repeatedly depinned by a sinusoidal voltage, the power spectrum of the CDW current must include a broad band component due to the ordinary broad band noise associated with sliding CDW conduction. However, the ac switching noise of Fig. 7-3 is as much as 10 dB larger than the broad band noise associated with sliding CDW conduction. We propose that ac switching noise arises because the switching process itself is unpredictable.

Consider the current through a switching sample driven by a sinusoidal voltage. If the switch occurs instantaneously at exactly the same voltage for each cycle of the sinusoidal drive, then (ignoring broad band noise associated with sliding CDW conduction) the CDW current will be a perfectly periodic function of time. Only harmonics will appear in the

power spectrum of the CDW current. However, if the switch occurs at a slightly different voltage each cycle of the ac drive, or if the switch itself takes finite time to occur and is irregular, then the CDW current will not be a perfectly periodic function of time. The power spectrum of the CDW current will contain harmonics plus a broad band component. Thus the observation of ac switching noise supports the notion that switching is an unpredictable process.

The conclusion that switching is unpredictable is consistent with previous observations of Zettl and Grüner[28]. Current pulses with $I>I_C$ were applied to a switching sample. The CDW remained pinned for a time τ_{wait} after the beginning of the pulse and then depinned in a shorter time τ_{switch}. The waiting time was a random variable, distributed about its mean with a Lorentzian probability distribution. The mean τ_{wait} and the width of the distribution were found to decrease as the height of the pulse I above threshold increased. For pulse height $I=1.01\ I_C$, the average τ_{wait} was 100 μsec. The switching time τ_{switch} was of the order of 1 μsec.

For a switch to occur, a large fraction of the CDW must depin. This means that the domains associated with many ultra-strong pinning centers must begin to slide at nearly the same time. An appealing picture of the onset of CDW conduction in a switching sample is that, when a critical electric field is exceeded, an avalanche of the ultra-strongly pinned domains occurs. The results of Zettl and Grüner have been modeled by Joos and Murray[29] as arising from such an avalanche-like process. The CDW is treated as a two-dimensional ribbon of identical domains (the physical origins of the domains and their couplings are not specified in this model). When an electric field exceeding threshold is applied to the crystal, each domain is assigned a probability per unit time of depinning. Once a single domain is depinned, it can trigger depinning of neighboring domains, thus setting off a "depinning wave", or avalanche. The model reproduces the waiting and switching times reported by Zettl and Grüner[28]. It is likely that the Joos-Murray model sinusoidally driven through threshold at frequencies less than $1/\tau_{switch}$ will result in power spectra similar to

those for ac switching noise (a broad band component plus spikes at the drive frequency and its harmonics).

In attributing ac switching noise to a repeated avalanche process, we are invoking a many-degree of freedom explanation. An avalanche takes a finite amount of time to occur, as observed in switching CDWs by Zettl and Grüner. When a switching CDW is driven at frequencies greater than $1/\tau_{switch}$ ($\approx$1MHz), the avalanche will not have time to occur. A qualitatively different regime of switching CDW dynamics ensues, and is described in the next section

7.4.2. Mode-locking

It is crucial to include many degrees of freedom in order to understand most aspects of the dynamics of nonswitching samples [14,15,34,35]. In switching samples, many degree of freedom pictures have been invoked to explain depinning, the instabilities associated with negative differential resistance, and ac switching noise. Thus it is surprising that the simplest route to chaos, the period doubling route, occurs in switching CDWs. This route to chaos occurs in systems with a small number of active degrees of freedom. Evidently, the many-body dynamics of switching CDWs "collapses" during mode-locking to a state in which only a few degrees of freedom are important. This collapse is similar to the broad band noise suppression observed during mode-locking in nonswitching CDWs[10]. Thus, even though the dynamics of the mode-locked states in switching CDWs are more complicated than those of nonswitching CDWs, in both cases the dynamics are characterized by few degrees of freedom

Given the low-dimensional dynamics of the mode-locked switching CDW system, it is appropriate to analyze our results mathematically in terms of low-dimensional maps and differential equations. In section 7.4.2.1, mode-locking in switching CDWs is examined in light of dynamical systems theory. In 7.4.2.1.1 the structure of mode-locking in switching CDWs is shown to be consistent with the simplest mathematical realization of a mode-locking system, the two-parameter sine circle map. For parameters appropriate to

our experiments, the sine circle map predicts a period doubling route to chaos which may be modeled by the even simpler one-parameter logistic map. In 7.4.2.1.2, the period doubling route to chaos is compared to the period doubling cascade in the presence of noise studied by Huberman and Crutchfield[20]. In 7.4.2.1.3, the instabilities of Figs. 8-10 are compared with predictions of Wiesenfeld[20,21] for noisy precursors of co-dimension one bifurcations. In section 7.4.2.2 the physical mechanisms for mode-locking in switching CDWs are explored

7.4.2.1. Dynamical systems analysis

7.4.2.1.1. The sine circle map and the structure of mode-locking

The sine circle map is a discrete mapping that has been studied extensively as a paradigm of natural systems with two competing periodicities[17,18,32-34]. Natural systems evolve in continuous time. However, all the information contained in continuous time orbits is superfluous to an understanding of many aspects of the dynamics. Consider a periodically driven system like the ac+dc driven damped pendulum[31]

$$\beta\frac{d^2\theta}{dt^2} + \frac{d\theta}{dt} + \sin(\theta) = f_{dc} + f_{ac}\sin(\omega t) \qquad (7\text{-}1)$$

The equation is written in dimensionless form. θ is the phase of the pendulum, β is a parameter quantifying the inertia of the pendulum, f_{dc} and f_{ac} are respectively the dc and ac torque on the pendulum, and ω is the dimensionless frequency of the ac torque. To determine the time average phase velocity $d\theta/dt$ or the frequency of the pendulum's orbit relative to the frequency of the ac drive, it is necessary to sample the phase only once each cycle of the ac drive at $\theta_n=\theta(t=nT)$, where n is an integer and $T=2\pi/\omega$. It has been shown for certain parameter values that Eq. 7-1 may be modeled by a one-dimensional mapping of the circle (θ) onto itself[32]. The most studied member of this class of mappings is the sine circle map

$$\theta_{n+1} = \theta_n + \Omega + \frac{K}{2\pi}\sin(2\pi\theta_n) \qquad (7\text{-}2)$$

The solutions to Eq. 7-2 have a rich structure which has been investigated in detail by many authors[17,18,32-34]. Particular attention has been devoted to the universal scaling behavior of high order mode-locked states near the quasiperiodic transition to chaos at K=1. We find that, for switching CDWs, Eq. 7-2 has predictive power for even the low order 0:1, 1:2 and 1:1 mode-locked states.

The structure of mode-locking predicted by the circle map for the 0:1, 1:1 and 1:2 mode-locked steps is shown in Fig. 7-15, for $0<K<3.5$. Since θ is a mod 1 variable, the structure of mode-locking is perfectly periodic in Ω, repeating itself with a periodicity 1. A detailed calculation of the structure of mode-locking for $0<K<1.5$ has been performed[33]. We have added a calculation of the boundaries of the 0:1, 1:2 and 1:1 mode-locked regions for values of K up to 3.5. The boundaries of the 0:1 and 1:1 steps were determined by a simple linear stability analysis. The boundaries of the 1:2 step were calculated by iterating the circle map on a computer in the neighborhood of the boundary until the 1:2 behavior lost stability to an unlocked state.

For $K<1$, the sine circle map is a monotonically increasing function of θ. The fraction of the Ω axis occupied by mode-locked regions is a small but increasing function of K for $K<1$. When the solution is inside the 0:1 or 1:1 region, θ is at a period 1 fixed point and returns to the same value each iteration of the map. The winding number $W= \lim (\theta_N-\theta_0)/N$ is 0(mod 1), independent of Ω. If the solution is in the 1:2 region, the winding number is 1/2 independent of Ω and q is at a period 2 fixed point. In between the 0:1 and 1:1 steps the system alternates between higher order mode-locked states and unlocked (quasiperiodic) states.

At K=1, the sine circle map develops an inflection point and the power spectrum develops broad band noise. This is the quasi periodic transition to chaos, which is distinct from the period doubling route to chaos we have observed. At K=1, it has been shown for the sine circle map that the space between mode-locked steps is a fractal with dimension 0.87[17]. This prediction has been verified in several physical systems[35].

Above K=1, the circle map has a local maximum, and the possible states of the system are different[33,34]. At the edges the (n:1, n:2) regions shown in Fig. 7-15, the solutions are mode-locked as for K<1, with W=(0,1/2) and periodicity (1,2). As Ω is swept toward the center of the mode-locked regions, the solutions maintain their winding number but undergo period doubling instabilities[18]. For sufficiently high K, the solutions near the centers of the mode-locked regions become unlocked and chaotic. The first period doubled states occur inside the n:1 locked regions for K>2 [18], and at lower values of K for higher order mode-locked states. For K>π, the 0:1 and 1:1 steps begin to overlap. As Ω is swept, the system jumps hysteretically from one step to the next. For K near π, as Ω is swept from the edge of a step towards the middle, a period doubling route to chaos is observed[36]. This is consistent with experiment (see Fig. 7-6).

It is not straightforward to make a one-to-one correspondence between the parameters of our experiment and the parameters of the circle map. The winding number W is defined as the large N limit of $(\theta_N - \theta_0)/N$. W is proportional to the average phase velocity of the pendulum, or in our experiment to the dc velocity of the CDW. In the absence of nonlinearity (K=0), W=Ω. In the high dc field limit, V_{dc} is proportional to the CDW velocity. Since depinned switching CDWs are in the high field limit[2], it is reasonable to make a correspondence between W and V_{dc} over small ranges of dc bias. The strength of the nonlinearity K is most closely related to the experimental parameter V_{rf}. However, changing V_{rf} changes both the strength of the nonlinearity and the threshold for depinning a CDW. Thus changing V_{rf} in an experiment corresponds to changing both Ω and K in the circle map. In our comparison with the circle map, we assume that, for fixed V_{rf}, changing the dc bias between the 0th and 1st mode-locked steps corresponds to changing Ω at constant K in the circle map.

Fig. 7-16 shows the structure of mode-locking for sample #1 at T=19K driven by a 30 MHz rf field. The regions of 0:1 (pinned), 1:2 and 1:1 mode-locking are plotted in the V_{dc}-V_{rf} plane[37]. At the lowest values of V_{rf} (top of this figure), there is a hysteretic transition

between the 0:1 and 1:1 steps, and the 1:2 step is eclipsed. There is no space between the 0:1 and 1:1 steps. The period doubling route to chaos is most strongly developed in this region of most hysteretic mode-locking. For higher values of V_{rf} (lower in the figure) the 1:2 step emerges and a smaller fraction of parameter space is occupied by the mode-locked regions shown. Period doubling instabilities persist, but the period doubling cascade is not so fully developed as in the highly hysteretic region. Below the critical line drawn in this figure, the period doubling and other instabilities are no longer observed, and the 1:2 mode-locked region takes up a smaller and smaller fraction of the space between the 0:1 and 1:1 mode-locked regions.

Fig. 7-17 shows the 0:1, 1:1 and 1:2 mode-locked steps (also for sample #1) for f=50 MHz and T=37K, just above the switching onset temperature. For these parameters, period two, period four, and Virtual Hopf behavior were observed, but fully developed chaos was not observed. Unlike in the low temperature case, the 1:2 mode-locked step is always visible for this set of parameters. For low values of V_{rf}, no period doubling instabilities are observed and the 1:2 step occupies a relatively small fraction of the space between the 0:1 and 1:1 steps. As V_{rf} is increased, the fraction first increases and then decreases. Period doubling instabilities are observed in the intermediate range of V_{rf}. For the highest values of V_{rf}, the fraction occupied by the 1:2 step shrinks to a very small value and no period doubling instabilities are observed.

Figs. 16 and 17 demonstrate that the fraction of parameter space which is mode-locked is positively correlated with the presence of dynamical instabilities. This behavior is consistent with Fig. 7-15, calculated from the sine circle map. However, Figs. 16 and 17 show a surprising correspondence between the parameter K in the circle map and the experimental parameter V_{rf}. At T=19K, V_{rf} is negatively correlated with K: small (large) values of Vrf correspond to large (small) values of K. At T=37K, K appears to first increase and then decrease as V_{rf} is monotonically increased. The dependence of the strength of the nonlinearity on V_{rf} will be discussed in section 7.4.2.2.

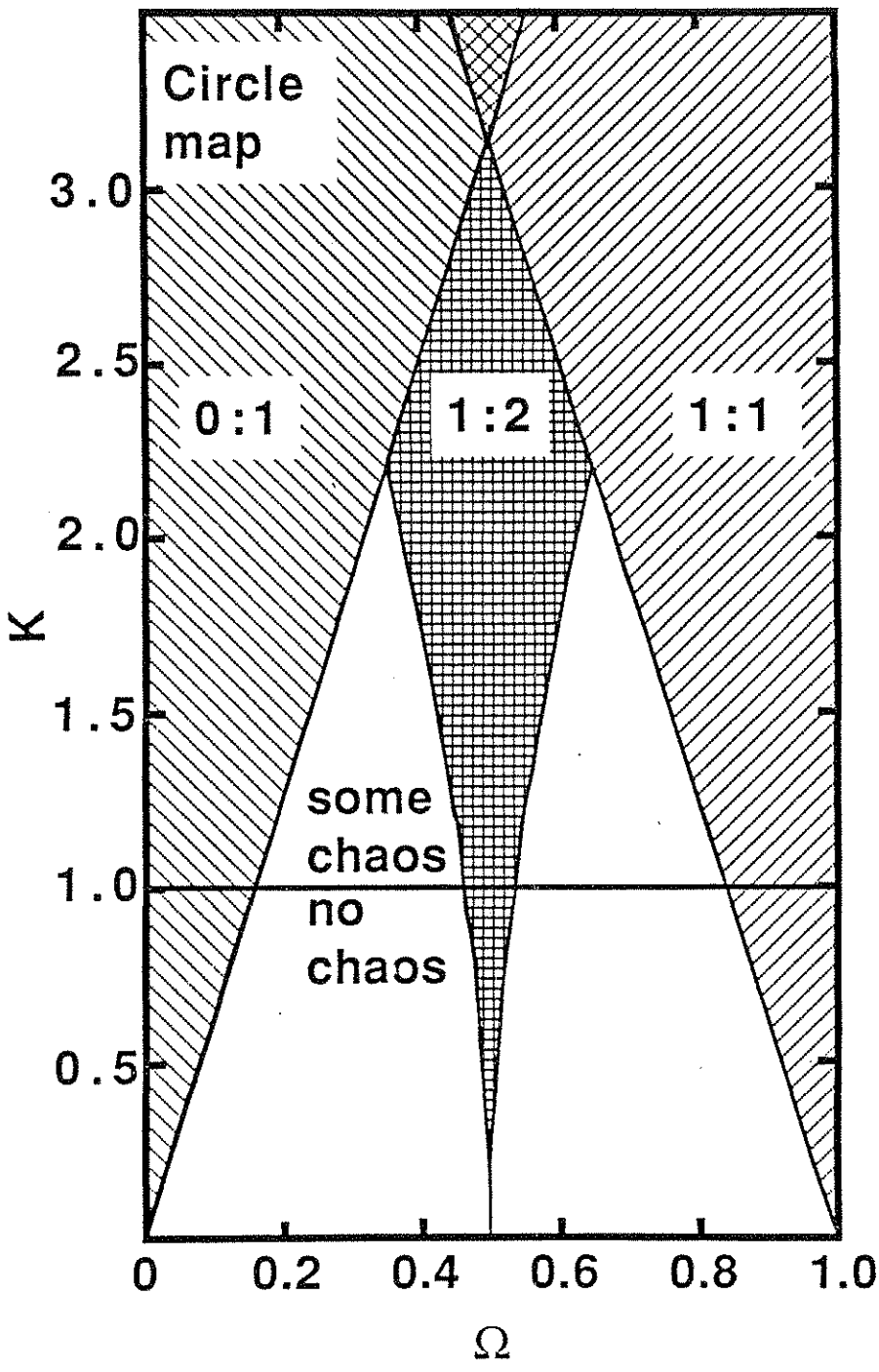

Fig. 7-15- 0:1, 1:2 and 1:1 mode-locked regions for the sine circle map (After Refs. 18,19,35,40). Period doubling and chaos are observed only above the solid line.

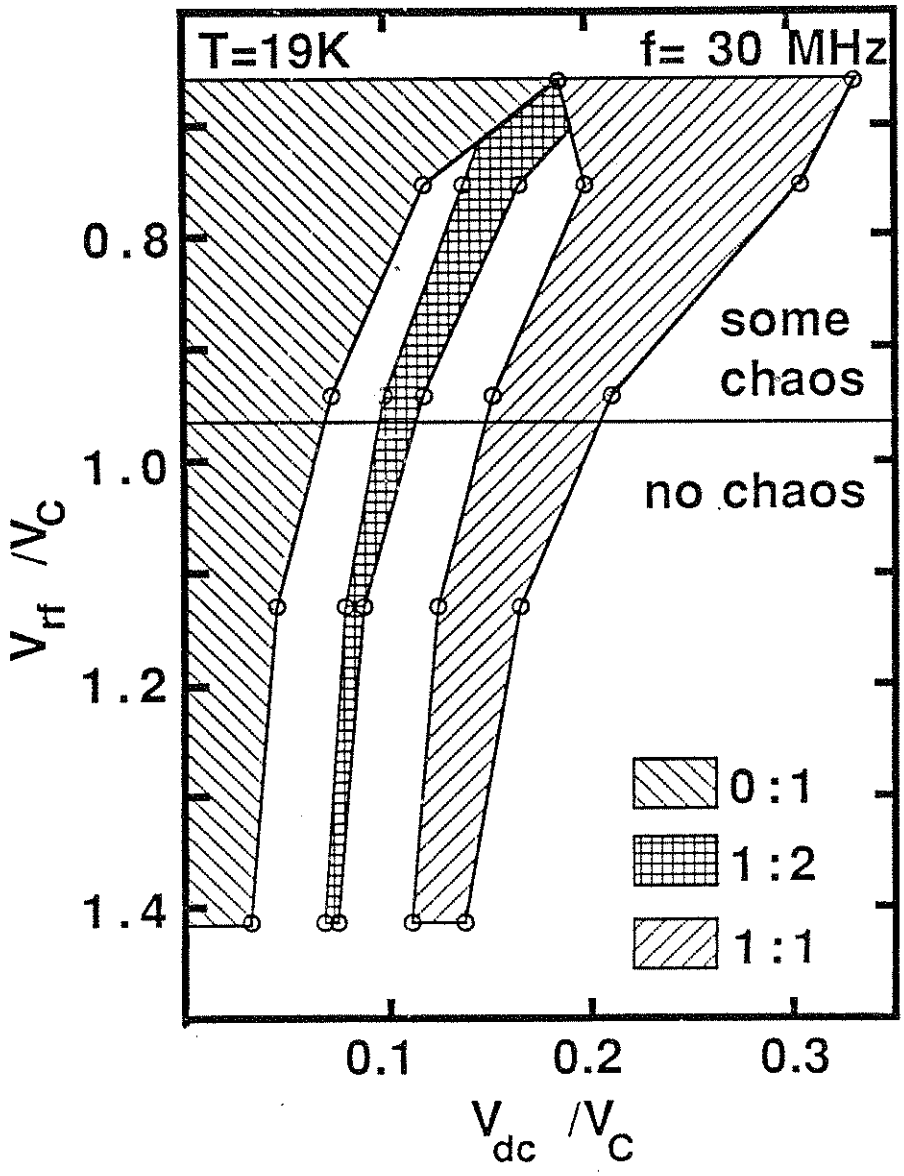

Fig. 7-16- 0:1, 1:1 and 1:2 mode-locked regions of sample #1 for a temperature well below the switching transition temperature. Period doubling and chaos are observed only above the solid line.

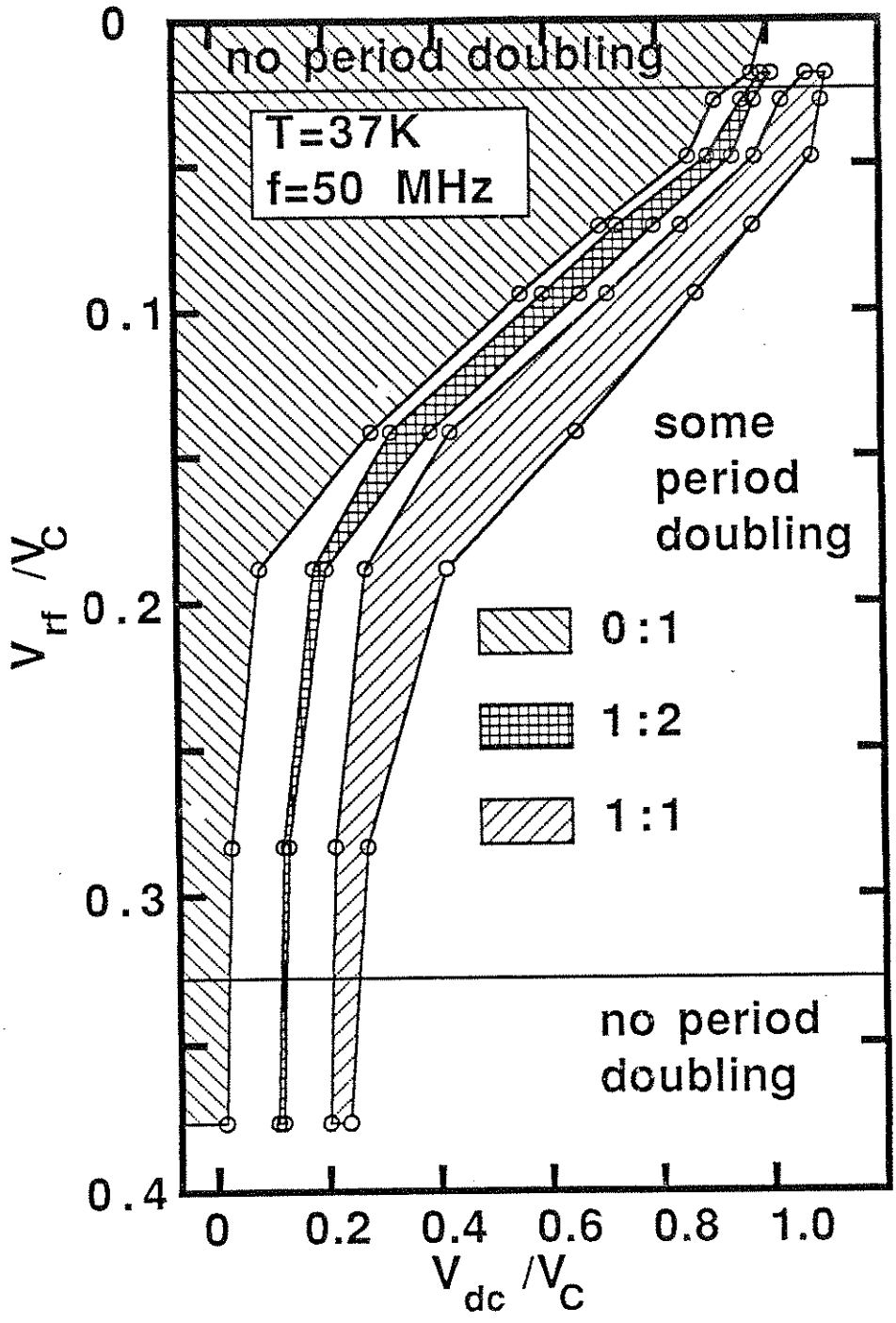

Fig. 7-17- 0:1, 1:2 and 1:1 mode-locked regions of sample #1 for temperature just above the switching temperature. Period doubling is observed only between the solid lines.

The period doubling route to chaos and the structure of mode-locking are both nearly periodic in dc bias over a certain range of dc bias. For instance, the 1:1, 3:2, and 2:1 mode-locked regions could have been plotted in Figs. 15-17 instead of the 0:1, 1:2 and 1:1 regions. The dependence of the widths of the mode-locked regions on V_{rf} is similar. The major difference is that the 1:1 region is narrower than the 0:1 region.

The circle map's best known prediction[17] is that the fractal dimension of the space between mode-locked steps is 0.87 at the critical line K=1. The critical line is usually identified in physical systems by a sudden onset of broad band noise signalling the quasiperiodic transition to chaos. An attempt was made to verify this prediction in nonswitching CDWs, but the critical line was not located[9]. The fractal dimension of the space between mode-locked steps in nonswitching CDWs has been measured for various rf amplitudes, and it was found that the fractal dimension was less than 0.87 for all values of the applied rf amplitude[38]. Thus it appears that, in the language of the circle map, mode-locking in nonswitching CDWs is always subcritical (described by the circle map with K<1)[39].

The observation of period doubling in mode-locked switching CDWs indicates that mode-locking in this system can be supercritical (period doubling occurs in the sine circle map for K>1). Thus it is possible to test some scaling predictions of the circle map. The critical lines in Figs. 16 and 17 separate regions in which period doubling is and is not observed in a switching CDW sample. The "dimension" of the unlocked space along these lines should be a lower bound[40] to the dimension predicted by the circle map at the quasiperiodic transition to chaos. We find[40] d=0.85±.05 at the lower critical lines in Figs. 16 and 17. This lower bound on d is in agreement with the predictions of the circle map.

The structure of mode-locking in switching CDWs is seen to be consistent with the predictions of the circle map in nontrivial ways. 1) The presence of dynamical instabilities is correlated with the width of mode-locked steps. 2) The structure of mode-locking and the period doubling route to chaos are periodic in dc bias. 3) The period doubling cascade

occurs as the system is pushed from the edge of mode-locked regions toward the middle. 4) The dimension of the space between mode-locked steps at the critical line is within experimental error of the prediction of the circle map.

7.4.2.1.2. Period doubling route to chaos

The circle map has a quadratic local maximum for K>1. The presence of the local maximum leads to the period doubling route to chaos, which may be described in terms of an even simpler discrete map, the 1-parameter logistic map[16,41]

$$x_{n+1}=bx_n(1-x_n) \qquad (7\text{-}3)$$

X is between 0 and 1 and b is between 0 and 4. As the bifurcation parameter b is increased from 0, the steady state orbits undergo an infinite sequence of period doubling bifurcations which accumulate geometrically at some critical parameter b_c. For $b>b_c$, the orbits are chaotic and fall in attractors with 2^m bands. As b is increased beyond b_c, these bands merge pairwise until there is only a single chaotic band. Hence there is an apparent symmetry about $b=b_c$: for $b<b_c$, the orbits are periodic with period 2^n. For $b>b_c$, the orbits are chaotic but they lie in attractors with 2^m bands and hence their power spectra look like noisy versions of 2^m periodic orbits. Huberman and Crutchfield[19] studied Eq. 7-3 in the presence of external noise. They showed that for a given noise level, the period doubling cascade is truncated at some 2^m periodic orbit and the system goes into a 2^m band attractor. All the states with period greater than 2^m and all the attractors with more than 2^m bands are washed out by the noise. The absence of high order periodic orbits in the presence of noise has been called the "bifurcation gap".

The bifurcation gap is evident in the sequence of power spectra in Fig. 7-6. The period doubling sequence is truncated at period 4. The spectrum in Fig. 7-6a.iii has significant noisy flanks on the sides of the period 4 subharmonics, indicating that this spectrum is between period 4 and a 4 band attractor. Fig. 7-6a.iv, with its noise peak centered around f/2, is the spectrum of a 2-band attractor. This sequence of spectra is a period doubling

route to chaos with all of the states between the period 4 orbit and the 4 band attractor removed.

7.4.2.1.3. Noisy precursors

The observation of the bifurcation gap dramatizes the importance of taking into account the effects of noise in explaining our experimental results. An elegant theory of the effect of noise on codimension one bifurcations of dynamical systems has been developed by K. Wiesenfeld[20]. The theory is based on the fact that a dynamical system that is near a bifurcation is almost unstable and hence is more susceptible to noise than one that is far from a bifurcation. Thus power spectra of dynamical systems near codimension one bifurcations exhibit bumps near the frequency at which an instability is about to occur. For instance, when a system driven at frequency f is near a period doubling bifurcation, the theory of noisy precursors predicts that a broad bump at f/2 will appear before one actually observes the sharp peak at f/2 that signifies that the period doubling bifurcation is complete. Another type of codimension one bifurcation of a periodic orbit is a Hopf bifurcation. In a Hopf bifurcation, a periodic orbit whose power spectrum has only a single frequency and its harmonics becomes unstable to a quasiperiodic orbit in which two incommensurate frequencies appear.

The noisy precursor phenomenon most closely related to our observations is the Virtual Hopf Phenomenon[21]. The sequence of power spectra characteristic of this phenomenon is shown in Fig. 7-18. In the top trace of Fig. 7-18, the power spectra show bumps symmetrically located about half the driving frequency. These are the precursors to a Hopf bifurcation. However, as the bifurcation parameter is tuned,the bumps move towards f/2 and the spectra evolve into the precursors for a period doubling instability. In the third trace of Fig. 7-18, the system has undergone a period doubling bifurcation. The height and width of the noisy precursor peaks are related to the rate at which the system relaxes to a limit cycle after it has been kicked off the limit cycle by a perturbation. The width of the noisy precursor peak is a measure of the longest relaxation time of the system. It has been

argued that this phenomenon should be common in dynamical systems exhibiting a period doubling instability.

Sequence of power spectra presented in Fig. 7-7 resembles very closely the sequence characteristic of the virtual Hopf phenomenon. Fig. 7-8 is not identical to the Virtual Hopf Phenomenon, but the appearance and disappearance of broad bumps in the power spectrum is strongly suggestive of a noisy precursor explanation. From the 1 MHz width of the broad bumps in both figs. 8 and 9, we extract a relaxation time of the order of 1 μsec. The spectra in Fig. 7-9 may also have a noisy precursor explanation.

An alternate explanation of the spectra in Fig. 7-7 is possible. The spectra in this figure look very much like spectra observed during mode-locking of ordinary nonwswitching samples[12]. The broad bumps that travel through the spectrum could be interpreted as narrow band noise peaks which become mode-locked on subharmonic steps when the peaks sharpen into period three and period two. This explanation is problematic because the appearance of a strong peak at f/2 did not necessarily coincide with the observation of a n:2 step in the differential resistance. This matter requires further investigation. There is no easy explanation for the spectra in Fig. 7-8 as arising from narrow band noise in conventional mode-locking.

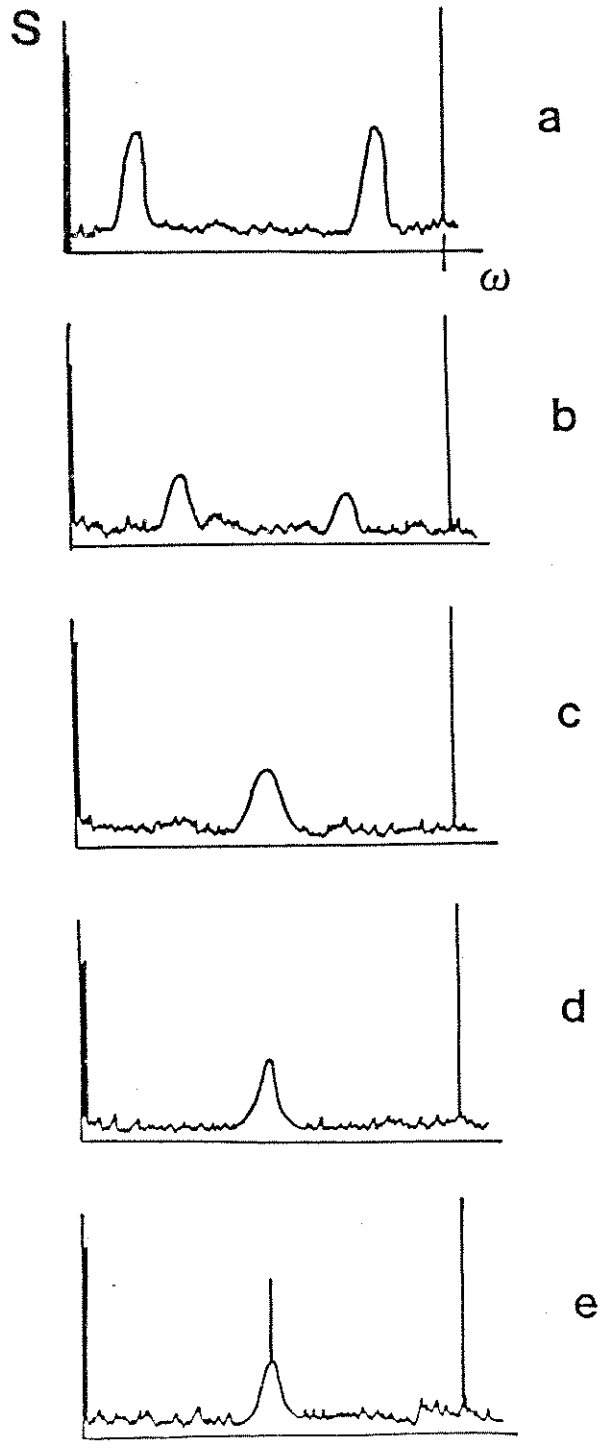

Fig. 7-18- Sequence of power spectra characteristic of the Virtual Hopf Phenomenon (Reprinted from ref. 21).

7.4.2.2. Physical mechanisms of mode-locking and period doubling

Section 7.4.2.1 classified certain aspects of mode-locking in switching CDWs as manifestations of behavior common in simple nonlinear dynamical systems. This section examines mode-locking in ac-dc driven switching CDWs in terms of the underlying physical processes. Period doubling and chaos in switching CDWs are explained as the frustrated response of a strongly entrained system with a motion-dependent inertia[3,4]. Period doubling and chaos occur over a limited range of driving frequencies, driving amplitudes and dc biases. These boundaries for nonlinear behavior are qualitatively explained and it is suggested that switching CDWs depolarize on a time of the order of 1 μsec. The physical relevance of the circle map nonlinearity parameter K is discussed.

Inertia does not appear to play any role in nonswitching CDW transport[1]. In contrast, mode-locking in switching CDWs has many characteristics of an inertial, underdamped response[15]. The symptoms of nonnegligible inertia are hysteresis in the dc I-V curve, and the inductive ac conductivity observed in switching CDWs biased past threshold[3,6]. The simplest differential equation which incorporates inertia and exhibits mode-locking is the much studied pendulum equation (Eq. 7-1). The solutions to this equation share many of the features of the experimentally observed behavior of mode-locked switching CDWs. For b>1 (underdamped), the solutions to the pendulum equation exhibit hysteretic Shapiro steps, and a period doubling route to chaos is observed on some of these Shapiro steps[43-45]. We conclude that some "pseudo-inertia" plays a significant role in switching CDW transport.

The underdamped pendulum equation does not agree in detail with the behavior of switching CDWs[3,4,6]. The ac conductivity of a switching CDW with no applied dc field appears overdamped. This is contrary to the prediction of Eq. 7-1, and indicates that the pseudo-inertia is only effective when the CDW is in motion [3,4]. Equation 6 predicts a chaotic response[43] only for drive frequencies $\beta-1<\omega<\beta-1/2$. This is a much narrower range than observed in switching CDWs. Finally, the period doubling route to chaos in

Eq. 7-1 is not periodic in dc bias as it is in CDWs[43]. The period doubling route may occur on one step, then skip the next step. In fact, as dc bias is increased in Eq. 7-1, mode-locked steps are not necessarily visited in order of increasing winding number[43]. In switching CDWs, these steps are always visited in order of increasing winding number (e. g., the CDW current increases monotonically with dc bias).

The phase slip process gives rise to a motion dependent inertia which can qualitatively account for the chaotic response of a switching CDW[3,4]. The phase slip process requires a macroscopic polarization of the CDW prior to the collapse of the CDW amplitude. After the amplitude collapse, it takes a finite time τ for the CDW to depolarize and slide. This lag in the response is equivalent to inertia (in inertial systems, the response lags the force). When the phase slip process is entrained at a frequency of order $1/\tau$, the CDWs tendency to follow the external forcing may compete with its requirement to "remember" its previous polarization state. This competition leads to a frustrated subharmonic or chaotic response. Period doubling occurs both just above and below the switching onset temperature. The period doubling observed just above the switching onset temperature can also be attributed to the polarization-induced inertia, because at these temperatures significant polarization may occur without a hysteretic switch.

The longest depolarization time provides a natural lower bound on the rf frequency required to produce a frustrated response (There may in principle be many depolarization times in a given sample, and the distribution of these times may depend on driving conditions). Period doubling and chaos occurred in our measurements on sample #1 only for driving frequencies greater than 1 MHz, suggesting that the longest depolarization time in this sample was of the order of 1 μsec. Other experimental results also suggest that the longest depolarization times τ in switching samples are of the order of 1 μsec. The width of a noisy precursor reflects the longest relaxation time of a system. The noisy precursors shown in Figs. 7 and 8 for sample #1 have widths of order 1/1 μsec. The switching time τ_{switch} ascertained from pulsed experiments is also likely related to the depolarization time.

Measurements on a different sample by Zettl and Grüner[28] found τ_{switch} of the order of 1μsec. There are also upper bounds in parameter space for the observability of period doubling and related instabilities. The disappearance of these frustrated responses for large rf amplitude, dc bias or rf frequency can be attributed to a suppression of motion-dependent inertia. If the CDW is forced to move too rapidly, the polarization and depolarization which are inherent to the phase slip process do not have time to occur. The motion-dependent inertia is suppressed. In the absence of motion-dependent inertia, the switching samples should behave like nonswitching samples. This similarity is borne out in Figs. 5 and 14. For the rf amplitudes above which period doubling instabilities are observed, the differential conductance curves look similar to those for nonswitching CDWs. As a function of dc bias, there is a relatively small ratio of locked to unlocked space these high rf amplitudes.

It is now possible to make a physical interpretation of the nonlinearity parameter K in the circle map, at least for switching samples. Period doubling and chaos in switching CDWs occur for large values of K (small space between mode-locked steps). However, K *decreases* as rf amplitude is increased to large values. It was argued above that motion-dependent inertia also should decrease as rf amplitude is increased. Thus it appears that K is correlated with the motion-dependent inertia of the switching CDW system.

There is a more general mathematical argument for the presence of an upper boundary on the region in which period doubling instabilities are observed. When a nonlinear differential equation is forced sufficiently strongly, the nonlinearity becomes a mere perturbation on a linear system [13,14]. The dimensionless overdamped pendulum equation (Equation 6 with $\beta = 0$)illustrates the reduction of the effective nonlinearity of a system by strong forcing.

$$\frac{d\theta}{dt} + \sin\theta = e_{dc} + e_{ac}\sin(\omega t) \qquad (7\text{-}4)$$

Consider the limits: $e_{dc}>>1$, $e_{rf}\approx1$, $\omega\approx1$, $e_{rf}>>1$, $e_{dc}\approx1$, $\omega\approx1$ and $e_{dc}\approx1$, $e_{rf}\approx1$ and $\omega>>1$. In the limit of large (e_{dc}, e_{ac}, ω), $d\theta/dt$ is of the order of (e_{dc} , e_{ac}, ω), while the nonlinear term $\sin\theta$ is much smaller, of order 1. For large driving parameters, the effective nonlinearity of the overdamped pendulum equation becomes small. A similar analysis for the pendulum equation with finite mass is more complicated. However, it is expected that for large driving parameters, the effective nonlinearity of underdamped pendulum equation will also be reduced. The upper boundaries in V_{dc}, V_{rf} and ω can be attributed to the decreased effective nonlinearity of the switching CDW system for large driving parameters. The argument also explains why the widths of Shapiro steps in nonswitching samples decreases at high values of V_{rf}[14].

7.5. Conclusion

The dynamical instabilities observed in switching CDWs can be divided into two categories. Instabilities in the first category occur for low driving frequencies. These instabilities include the 1/f noise and intermittency observed for current driven switching CDW's in an NDR region, and the ac switching noise observed for combined low frequency dc and ac electric fields. The low frequency instabilities are attributed to the many degree-of-freedom dynamics many phase-slipping domains. The instabilities in the second category occur for high frequency (>1 MHz) driving electric fields. The high frequency instabilities are the period doubling route to chaos and related instabilities. For high driving frequencies, the independent switching CDW domains are synchronized by the rf electric field, causing the many-degree of freedom dynamics of the switching CDW system to collapse onto a subsystem with few dynamical variables. The collapsed dynamical system undergoes the period doubling route to chaos, which is characteristic of systems with few degrees of freedom. The one-dimensional circle map, the logistic map and the theory of noisy precursors explain many details of the second category of instabilities. Physically, period doubling in this case may be viewed as the frustrated

response of an inertial CDW which is strongly entrained by a radio frequency electric field. The CDW inertia arises naturally from the phase slip process.

This chapter has for the first time presented and classified a rich and varied assortment of instabilities observed in switching CDWs. This chapter represents the most successful application of the modern theory of nonlinear dynamical systems to the study of CDW systems. There is much room for further application of the tools of nonlinear dynamics to the study of this rich system. For instance, the theory of nonlinear dynamical systems provides a quantitative method for estimating the number of degrees of freedom involved in a chaotic process. The required procedure is to calculate the Hausdorff dimension of a chaotic attractor from a chaotic time series. This procedure is difficult to implement in switching CDWs because of the high frequencies involved. It would be useful to directly determine the number of degrees of freedom involved in the chaotic dynamics of switching CDWs by measuring the Hausdorf dimension of the instabilities of switching CDWs.

References

[1] For a review of nonswitching CDW conduction, see G. Grüner and A. Zettl, Phys. Rep. **119**, 117 (1985)

[2] R. P. Hall, M. F. Hundley and A. Zettl, to be published

[3] R. P. Hall and A. Zettl, to be published

[4] M. Inui, R. P. Hall, S. Doniach and A. Zettl, to be published

[5] R. P. Hall, M. F. Hundley and A. Zettl, Phys. Rev. Lett. **56**, 2399 (1986)

[6] R. P. Hall and A. Zettl, Solid State Commun. **50**, 813 (1984).

[7] P. Monceau, J. Richard, and M Renard, Phys. Rev. Lett. **45**, 43 (1980)

[8] A. Zettl and G. Grüner, Solid State Commun. **46**, 501 (1983)

[9] S. E. Brown, G. Mozurkewich, and G. Grüner, Phys. Rev. Lett. **54**, 2272 (1984)

[10] M. S. Sherwin and A. Zettl, Phys. Rev. B **32**, 5536 (1985)

[11] R. P. Hall and A. Zettl, Phys. Rev. B **30**, 2279 (1984)

[12] S. Bhattacharya, J. P. Stokes, M. J. Higgins and R. A. Klemm, Phys. Rev. Lett. **59**, 1849 (1987)

[13] L. Sneddon, M. C. Cross and D. S. Fisher, Phys. Rev. Lett. **49**, 292 (1982)

[14] S. N. Coppersmith and P. B. Littlewood, Phys. Rev. Lett. **57**, 1927 (1986)

[15] R. P. Hall, M. S. Sherwin and A. Zettl, Phys. Rev. B **29**, 7076 (1984)

[16] See for example, J. M. T. Thompson and H. B. Stewart, *Nonlinear Dynamics and Chaos* (John Wiley and Sons, Somerset, NJ, 1986)

[17] M. H. Jensen, P. Bak, and T. Bohr, Phys. Rev. Lett. **50**, 1637 (1983)

[18] L. Glass and R. Perez, Phys. Rev. Lett. **48**, 1772 (1983)

[19] J. P. Crutchfield and B. A. Huberman, Phys. Lett. **77A**, 407 (1980)

[20] K. Wiesenfeld, J. Stat. Phys. **38**, 1071 (1985)

[21] K. Wiesenfeld, Phys. Rev. A **32**, 1744 (1985)

[22] R. P. Hall, M. F. Hundley and A. Zettl, Syn. Met. **19**, 813 (1987)

[23] J. P. Stokes, S. Bhattacharya and A. N. Bloch, Phys. Rev. B **34**, 8944 (1986)

24 A. Zettl and G. Grüner, Phys. Rev. B **29**, 755 (1984)

25 R. P. Hall, M. F. Hundley and A. Zettl, Physica **143B**, 152-154 (1986)

26 R. P. Hall, M. S. Sherwin and A. Zettl, Phys. Rev. Lett. **52**, 2293 (1984)

27 M. S. Sherwin, R. P. Hall and A. Zettl, to be published

28 A. Zettl and G. Grüner, Phys. Rev. B **26**, 2298 (1982)

29 B. Joos and D. Murray, Phys. Rev. B **29**, 1094 (1984)

30 R. M. Fleming and L. F. Schneemeyer, Phys. Rev. B **33**, 2930 (1986); S. E. Brown, G. Grüner and L. Mihaly, Solid State Commun. **57**, 165 (1986)

31 C. Tang, K. Wiesenfeld, P. Bak, S. Coppersmith and P. B. Littlewood, Phys. Rev. Lett. **58**, 1161 (1987)

32 T. Bohr, P. Bak and M. H. Jensen, Phys. Rev. A. **30**, 1970 (1984)

33 M. H. Jensen, P. Bak and T. Bohr, Phys. Rev. A **30**, 1960 (1984); P. Bak, Physics Today **39**, 38 (1986)

34 T. Bohr and G. Gunaratne, Phys. Lett. A **113**, 55 (1985)

35 J. Stavans, F. Heslot, and A. Libchaber, Phys. Rev. Lett. **55**, 596 (1985); E. G. Gwinn and R. M. Westervelt, Phys. Rev. Lett. **59**, 157 (1987); S. Martin and W. Martienssen, Phys. Rev. Lett. **56**, 1522 (1986)

36 M. S. Sherwin, unpublished

37 We have defined the boundary of a mode-locked region as the point at which the differential conductance begins to drop from the high (unlocked) value. At high rf amplitudes, where there were two sets of interference peaks corresponding to two domains with different narrow band noise frequencies, only the mode-locked regions corresponding to the lower velocity NBN domain are recorded.

38 A. Zettl, Physica **23D**, 155 (1986)

39 Coppersmith and Littlewood have argued that subharmonic mode-locking in nonswitching CDWs is intrinsically a many degree of freedom effect, and that hence the predictions of the circle map are not relevant to mode-locking in nonswitching CDWs. We

do not address here the relevance of the circle map to mode-locking in nonswitching CDWs. If we assume that a circle map description is valid, then mode-locking in nonswitching CDWs appears subcritical (based on the scaling of the space between mode-locked steps) and is consistent with the absence of period doubling or chaos.

40 We have calculated the dimension d from the space between the 0:1, 1:2, and 1:1 mode-locked steps using an algorithm proposed by P. Cvitanovic, M. H. Jensen, L. P. Kadanoff and I. Procaccia (Phys. Rev. Lett. **55**, 343 (1985)). They have shown empirically that the fractal dimension may be calculated to within 1% accuracy by considering only the space between three relatively high order mode-locked steps that are neighbors in a branch of a Farey tree: steps with winding number p/q, p'/q' and (p+p')/(q+q'). The dimension is given by

$$\left(\frac{s_1}{S}\right)^d + \left(\frac{s_2}{S}\right)^d = 1 \qquad (7\text{-}5)$$

where S is the space between steps p/q and p'/q', and s1 and s2 are respectively the space between p/q and p+p'/q+q' and between p+p'/q+q' and p'/q'. We tested the accuracy of Eq. 7-5 for low order mode-locked states. A value d = 0.875 was calculated using Eq. 7-5 and the space between the 0:1, 1:1 and 1:2 mode-locked steps predicted by the circle map at K=1. This is within 1% of the value d=0.868 calculated using scaling arguments with many high order mode-locked steps18.

In switching CDWs, a quasiperiodic transition to chaos was not directly observed (perhaps it was obscured by the conduction noise associated with sliding CDW conduction). However, a line was observed (Figs. 7-16, 7-17) which separates regions of parameter space in which period doubling is observed from regions in which it is not. The sine circle map predicts that the onset of period doubling occurs at higher K values (wider mode-locked steps) than the quasiperiodic transition to chaos. Thus the dimension of the

unlocked space along the lines drawn in Figs. 7-16 and 7-17 represents a lower bound on the dimension of the complete Devil's staircase which occurs in the circle map at K=1.

41 R. H. May, Nature **261**, 459 (1976)); M. J. Feigenbaum, J. Stat. Phys. **19**, 25 (1978)

42. Codimension-one bifurcations are those that are achieved by changing only one parameter: saddle-node, transcritical, pitchfork, period doubling and Hopf bifurcations. see for instance, Guckenheimer and Holmes, Nonlinear Oscillations, Dynamical Systems and Bifurcations of Vector Fields (Springer-Verlag, New York, 1983), pp. 145-156.

43 R. L. Kautz, App. Phys. Lett. **52**, 6241 (1981)

44 D. D'Humières, M. R. Beasley, B. A. Huberman, and A. Libchaber, Phys. Rev. A **26**, 3483 (1982)

45 A. H. MacDonald and M. Plischke, Phys. Rev. B **27**, 201 (1983)

8. Electro-elastic coupling in charge density wave media

8.1. Introduction

Chapters 6 and 7 explored some aspects of mode-locking between the electronic degrees of freedom in a CDW and externally applied ac and dc electric fields. One conclusion of chapters 6 and 7 is that the number of electronic degrees of freedom active in CDW transport is drastically reduced during mode-locking[1]. This chapter explores the effect of mode-locking on the elastic properties of CDW conductors. A model of CDW elasticity is presented and solved for the cases of a CDW driven by dc, ac and combined ac and dc electric fields[2]. It is shown that mode-locking stiffens a CDW crystal by freezing out some of the degrees of freedom in the coupled lattice-CDW system.

Brill and Roark[3], and Mozurkewich et al.[4], first demonstrated that the elastic response of CDW crystals is highly sensitive to applied electric fields. In particular, the crystal Young's modulus Y strongly decreases and internal friction δ strongly increases when the CDW is depinned by a dc electric field E_{dc} exceeding the threshold field E_T. More recent experiments by Bourne et al.[5] show striking anomalies in Y and δ when the CDW is excited by combined dc and ac electric fields which induce electronic mode-locking.

The single- and many-degree-of-freedom models [6-9] reviewed in Chapter 5 assign degrees of freedom only to the CDW phase and not to the impurities or the lattice. Thus these models make no predictions about the response of the lattice to a sliding CDW. In the first attempt to calculate the elastic properties of CDW crystals, Coppersmith and Varma[10] considered a rigid CDW sliding through a deformable lattice. Although an anisotropy was found for the velocity of sound, the predicted effects were orders of magnitude smaller than the experimentally observed changes in Y and δ due to CDW depinning.

8.2. The model

This chapter proposes a model for CDW dynamics and elasticity in which degrees of freedom are assigned to *both* the lattice and the CDW. The model is an extension of

models based on the Fukuyama-Lee Hamiltonian Eq. 5-2. Elasticity is incorporated into the underlying lattice by a discretization which breaks the lattice and associated pinning potential into rigid units of mass M coupled harmonically by springs with spring constant K. The CDW is represented by discrete particles of mass m coupled harmonically to nearest neighbors by spring constant κ. The mechanical analog of this model is shown schematically in Fig. 1. The model can describe both commensurate and incommensurate cases, and it can also be extended to the random pinning case. Eqs. 8-1 to 8-3 are for the commensurate case, in which the wavelength of the sinusoidal potential is equal to the equilibrium length of the springs connecting adjacent lattice or CDW particles.

Assuming only nearest neighbor interactions, the potential energy function is

$$V=\sum_{j=1}^{N}\frac{\kappa}{2}(r_j-r_{j-1})^2+\frac{K}{2}(x_j-x_{j-1})^2+V(1-\cos[Q(r_j-x_j)]) \tag{8-1}$$

where r_j and x_j are respectively the (laboratory frame) positions of the jth CDW mass and jth lattice unit, V is the strength of the impurity pinning potential, and $Q = 2\pi/\lambda$ with λ the CDW wavelength, and N the total number of lattice (and CDW mass) units. Applying Lagrange's equations (and adding internal friction and external forcing) yields equations of motion

$$m\frac{d^2r_j}{dt^2}+\gamma\frac{d(r_j-x_j)}{dt}+\kappa(2r_j-r_{j+1}-r_{j-1})+QV\sin[Q(r_j-x_j)]=f_j(t) \tag{8-2}$$

$$M\frac{d^2x_j}{dt^2}+\Gamma\frac{d(2x_j-x_{j-1}-x_{j+1})}{dt}+\gamma\frac{d(x_j-r_j)}{dt}+\kappa(2x_j-x_{j+1}-x_{j-1})+QV\sin[Q(x_j-r_j)]=F_j(t) \tag{8-3}$$

where Γ is the internal friction of the lattice and γ is a frictional coupling between the CDW and lattice. $f_j(t)$ is the force applied to the jth charged CDW particles by external electric fields, and $F_j(t)$ is the external mechanical force applied to the jth lattice unit. In the limit

K--> ∞ (rigid pinning potential), Eqs. 8-3 become trivial and Eqs. 8-2 reduce to the driven Frenkel-Kontorova model[9].

In a typical experimental situation, screening by normal (uncondensed) electrons in the CDW crystal insures a relative uniformity of the applied field E throughout the crystal. Thus, in Eq. 8-2, we set $f_j(t) = f(t)$. For a general forcing term $f(t) = E_{dc} + E_{ac}\cos(wt)$, with E_{ac} the ac electric field amplitude, Eqs. 8-2 and 8-3 are analytically intractable, except if one considers small amplitude excitations and linearizes them. We here reduce the infinite set of equations 8-2 and 8-3 to the smallest set of equations that retain the essential physics of an elastic CDW interacting with an elastic lattice. The infinite chain of lattice units and CDW particles is truncated to three units. With clamped-clamped boundary conditions, the lattice is reduced to a single (renormalized) unit with its nearest neighbors fixed to the laboratory frame. The CDW is represented by a single (renormalized) particle whose neighbors are fixed to the CDW center of mass frame. The resulting equations of motion are

$$m^*\frac{d^2r}{dt^2} + \gamma_C\frac{d(r-x)}{dt} + k_C(r-v_{com}t) + eE_T\sin[2k_F(r-x)] = e[E_{dc}+E_{ac}\cos(\omega t)] \qquad (8\text{-}4)$$

$$M\frac{d^2x}{dt^2} + \gamma_C\frac{d(x-r)}{dt} + \Gamma_L\frac{dx}{dt} + K_Lx + eE_T\sin[2k_F(x-r)] = F\cos(\omega_r t) \qquad (8\text{-}5)$$

where r and x are respectively the laboratory positions of the CDW center of mass and lattice. m* is the total CDW effective mass in the crystal, e the total charge of the CDW, M_L the lattice mass, γ_C and Γ_L respectively the total CDW damping and internal lattice friction, and k_F is the Fermi wavevector. k_C and K_L parameterize respectively the total elasticity of the CDW and underlying lattice. $F\cos(\omega_r t)$ is the mechanical force applied to the lattice, the response to which determines the elastic properties of the system. The dc velocity of the CDW center of mass is v_{com}. Subtracting the position of the CDW center of mass $v_{com}t$ from the variable r in the third term of Eq. 8-4 ensures that the CDW may slide

continuously through the lattice, with k_c responding only to ac excitations (see Appendix C for details).

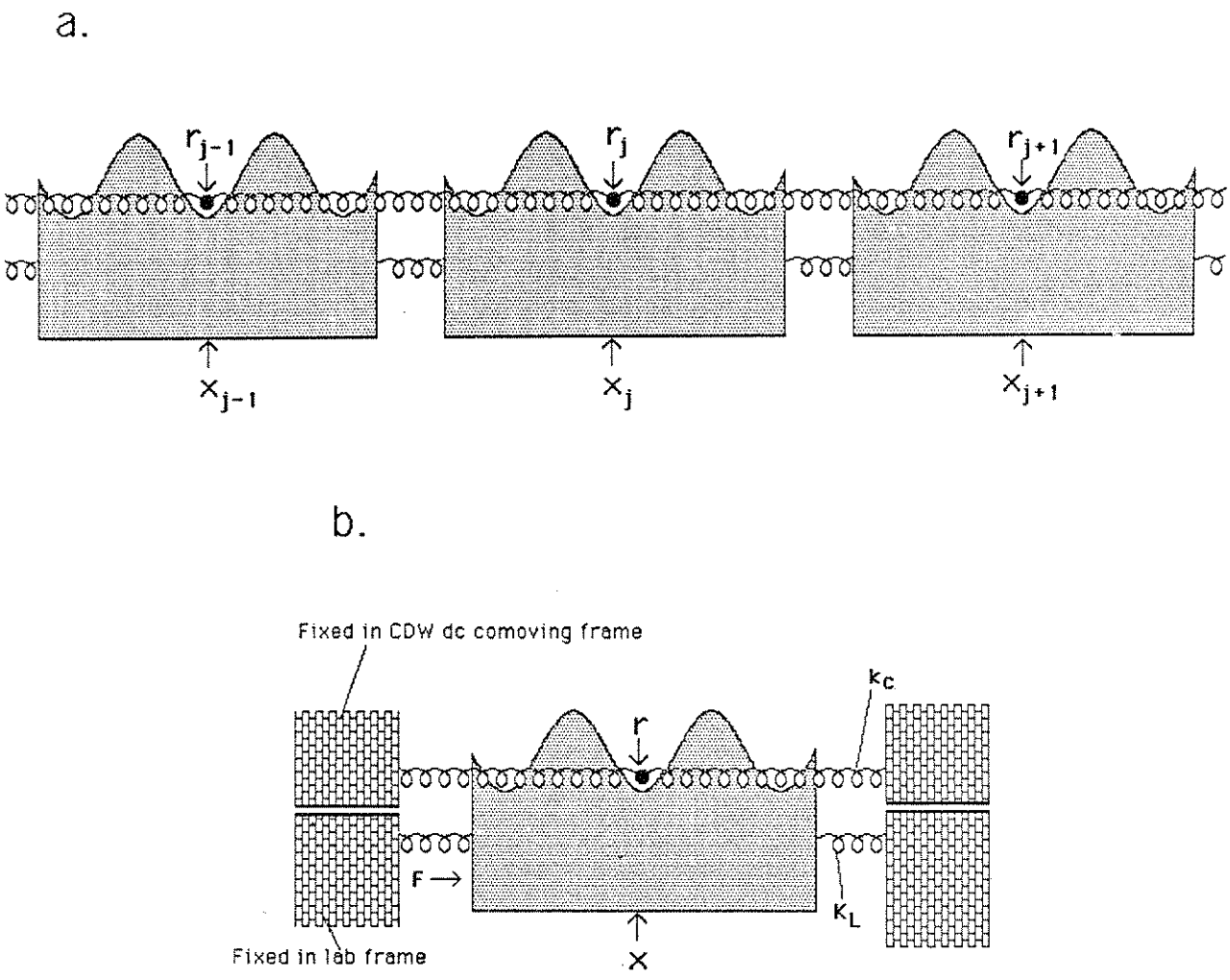

Fig. 8-1: Mechanical analog of the model of CDW elasticity, (a) for the infinite case (Equations 8-2 and 8-3), and (b) showing the boundary conditions applied to reduce the infinite case to equations 8-4 and 8-5. The "walls" to which the CDW spring is attached in (b) move with the steady state (dc) velocity of the CDW center of mass. Y and δ are determined from the resonant frequency and amplitude of the response of x to the mechanical force F.

8.3. Solution

We have solved Eqs. 8-4 and 8-5 , for a variety of dc and/or ac electric field drives, on an analog electronic computer built in our laboratory (see Appendix C). The mechanical force F in Eq. 8-5 was kept small. The Young's modulus and internal friction are determined from the resonant frequency and amplitude of the response of x to the mechanical force F ($Y \alpha (\omega_r)^2$ and $\delta \alpha \delta^{-1}(\omega_r)$). This procedure for determining Y and δ is analogous to that used in the actual vibrating reed experiments[3-5]. For all calculations discussed here, the parameters used are (in relative units) $eE_T=0.76\times10^{-3}$, $2k_F=6.28\times10^4$, $k_C=2.85$, $K_L=29.4$, $\gamma_C=0.95\times10^{-3}$, $\Gamma_L=10^{-3}$, $m^*=4\times10^{-11}$, $M_L=2\times10^{-5}$, and $\omega_r/2\pi\approx200$.

We consider separately three different electric field drive situations: E_{dc}=finite with E_{ac}=0; E_{ac}=finite with E_{dc}=0, and combined finite E_{dc} and E_{ac}. Fig. 8-2a shows the results of our simulation with E_{ac}=0. For $E_{dc} < E_T$, Y and δ are only weakly field dependent. For $E_{dc} >> E_T$, Y saturates at a value smaller that that corresponding to the pinned state, and δ saturates at a value larger than that corresponding to the pinned state. The bottom trace in Fig. 8-2a corresponds to the differential resistance dV/dI of the system, where an ohmic resistance representing normal carriers is assumed in parallel with the CDW condensate. With notable exception to the divergent behavior near threshold, the calculated behaviors of Y, δ, and dV/dI are in agreement with experimental results on $NbSe_3$ and TaS_3 in the presence of dc electric fields (Fig. 8-2b). Furthermore, the model predicts a "tracking" between the Y and dV/dI behavior (i.e. the Y and dV/dI curves are nearly identical in form); similar tracking is observed experimentally in $NbSe_3$ and TaS_3 [3-5]. The divergence in dV/dI near threshold (not observed experimentally) is endemic to finite-size classical models[11]; it is thus not surprising that Y and γ display similar divergent critical behavior near E_T. In the thermodynamic limit (e.g. Eqs. 8-2 and 8-3, with large N), we expect such divergences to be removed in dV/dI, and similarly in Y and δ[12].

In the range of finite E_{ac}, with E_{dc}=0, we have solved Eqs. 8-4 and 8-5 with ω/ω_r= 20. The results are displayed in the inset to Fig. 8-2a. Increasing E_{ac} from zero results in a smooth decrease in Y, and, within computational resolution, no detectable change in δ for very low E_{ac}. These results are in agreement with experimental results for TaS_3 under similar drive conditions, shown in the inset to Fig. 8-2b. In TaS_3, the crystal lattice was found to soften under application of ac electric fields, even with $E_{ac} < E_T$.

In the presence of combined dc and ac electric fields, CDW conductors display electronic "Shapiro step" mode-locking, where the internal narrow-band noise frequency ω_{NBN} of the CDW (proportional to CDW drift velocity) interferes with the external ac frequency ω. Such interference occurs in general whenever $\omega_{NBN}/\omega = p/q = n$, with p and q integers. Experiments on $NbSe_3$ and TaS_3 have demonstrated that, in the electronically mode-locked regions, both Y and δ tend to values characteristic of the pinned, E_{dc}=0 state.

As shown in the lower dV/dI trace of Fig. 8-3a, Eqs. 8-4 and 8-5 predict, in the presence of combined dc and ac electric fields, complete Shapiro step electronic locking[13]. The steps are identified with corresponding values of n. These calculations were performed with $E_{ac}/E_T = 3$. Also shown in Fig. 8-3a are Y and δ, calculated for the same set of drive parameters. It is clear that Shapiro step in the electronic response corresponds in the model to striking anomalies in the elastic constants. In the Shapiro step region, both Y and δ tend to their respective values measured with $E_{dc} = 0$, as observed in the experimental data of Fig. 8-3b. We also note the presence of harmonic (n = 2,3,...) and subharmonic (non-integral n) structure in the calculated and experimentally measured Y and δ.

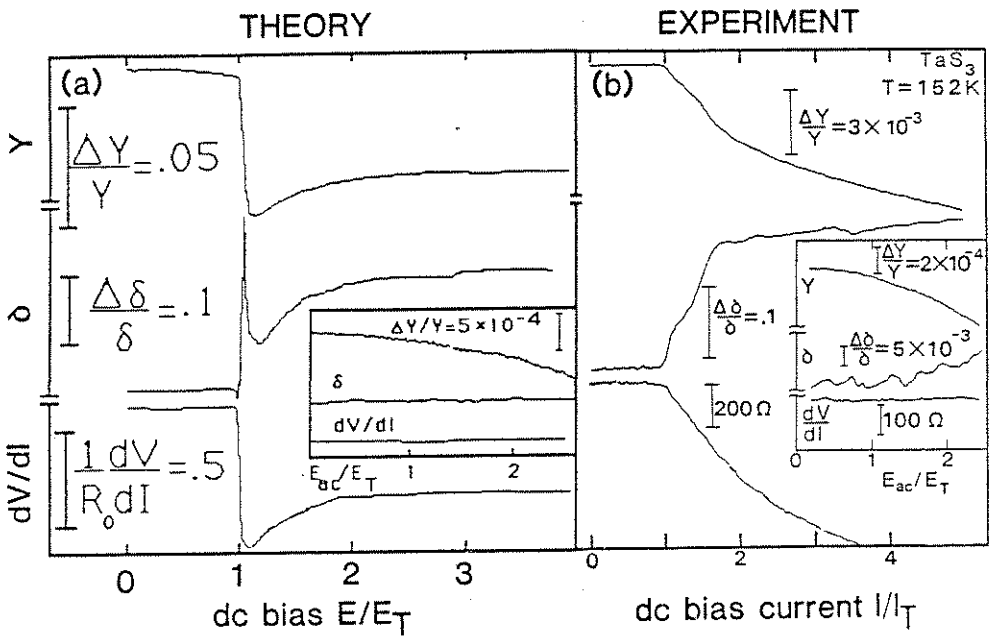

Fig. 8-2: Y, δ and dV/dI as functions of dc bias for E_{ac}=0. Insets: Y, δ and dV/dI as functions of ac amplitude for E_{dc}=0. (a) calculated from Eqs. 8-4 and 8-5. (b) measured in experiments[5].

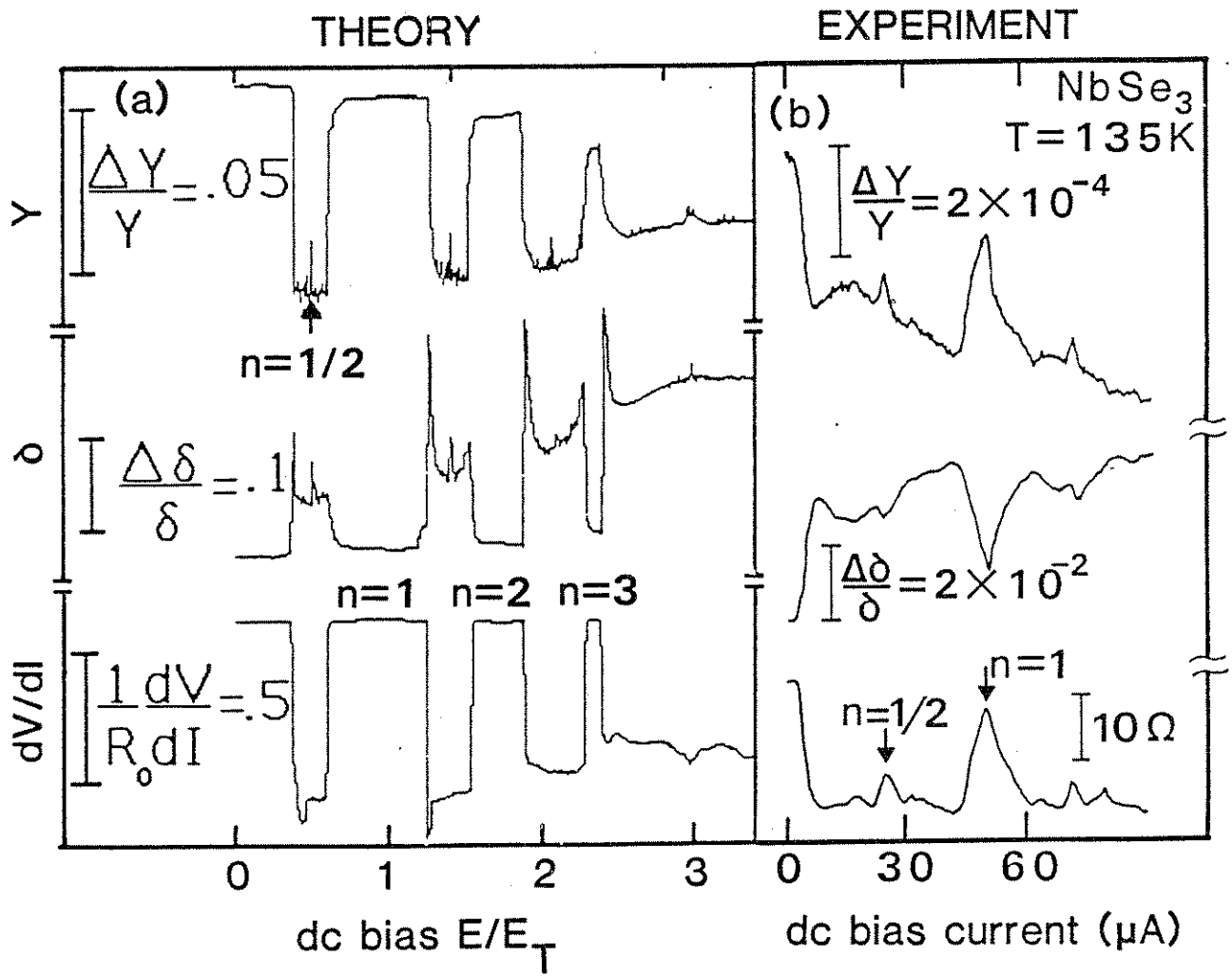

Fig. 8-3: Y, δ and dV/dI as functions of dc bias, (a) as calculated from Eqs. 8-4 and 8-5 with $E_{ac}/E_T=3$, $\omega/\omega_r=20$, and (b) measured in experiments[5]. The arrows identify interference structure.

8.4. Analytic treatment and quantitative comparison with experiment

The parameters used in the simulation are a compromise between those appropriate for a real CDW and those accessible to the analog computer. An analytic treatment of linearized versions of Eqs. 8-4 and 8-5 in low- and high-field limits facilitates intuitive understanding and enables quantitative comparison of the predictions of the model with experimental results. This section shows that, for $E_{dc}=0$, the sinusoidal potential in Eqs. 8-4 and 8-5 is sufficiently strong to freeze the lattice and CDW coordinates into a single effective degree of freedom. The effective stiffness in this case is the sum of the CDW and lattice stiffnesses. It is argued that mode-locking also freezes the lattice and CDW degrees of freedom into one. However, it is shown that in case of a sliding CDW which is not mode-locked, the CDW and lattice degrees of freedom are independent and the effective stiffness is the stiffness of the lattice alone. The difference between the stiffness in the pinned and sliding cases predicted by the model is roughly consistent with experiment.

To determine the elastic constants in the pinned case, the equations of motion 8-4 and 8-5 are linearized about the state x=0, r=0. A mechanical analog of this linearized system is shown in Fig. 8-4. By inspection, the effective spring constant felt by the mechanical force F in this mechanical analog is

$$K_{eff} = K_L + \frac{1}{\frac{1}{k_{pin}} + \frac{1}{k_c}} \qquad (8\text{-}6)$$

where K_{eff} is the effective spring constant, K_L is the lattice spring constant, $k_{pin} = 2k_F e E_T$ is the spring constant that arises from the restoring force of the sinusoidal potential, and k_c is the CDW spring constant.

When the CDW is sliding with rapid velocity ($E_{dc} >> E_T$, $E_{ac}=0$), the sinusoidal coupling between the CDW coordinate r and the lattice coordinate x averages to zero (see appendix C). Thus the effective spring constant for the rapidly sliding case is $K_{eff} = K_L$. The difference between the stiffnesses in the pinned and rapidly sliding cases is then

$$\Delta K_{eff} = \frac{1}{\frac{1}{k_{pin}} + \frac{1}{k_c}} \qquad (8\text{-}7)$$

We now make the connection between the parameters of the model and the physical constants of the CDW crystal. Eqs. 8-4 and 8-5 describe the dynamics of a macroscopic crystal. In computing $k_{pin}=2k_F e E_T$, the total charge of e the CDW in the crystal must be used. Thus $k_{pin}=2k_F e_{el}\rho_{el}LAE_T$ where e_{el} is the electronic charge, $2k_F \approx 10^8 cm^{-1}$, $\rho_{el} \approx 5\times10^{21} cm^{-3}$ [ref. 6-1] is the density of condensed electrons, L=0.1cm is the length of the crystal, A is the cross-sectional area and E_T=0.1V/cm. The spring constant K is related to the Young's modulus Y roughly by the relation Y=kL/A. From mean field theory, the contribution to Y of the CDW[3,4] has been estimated to be $10^9 dynes/cm^2 = k_c L/A$. Using these parameters, we find the ratio $\frac{k_c}{k_{pin}} \approx 10^{-8}$. For the above (typical) parameters, the coupling between the CDW and the lattice for E_{dc}=0 is so strong that the CDW and lattice truly act as a single degree of freedom for low frequency mechanical forcing. To a very good approximation, for parameters appropriate to a real CDW, $K_{eff}(E_{dc}=0) - K_{eff}(E_{dc}>>E_T) \approx k_c$.

Fig. 8-3 demonstrates that the elastic constants predicted by Eqs. 8-4 and 8-5 are virtually identical in the pinned and mode-locked cases. In the pinned case, the CDW phase is constrained at low frequencies to follow the minimum of the pinning potential . In the mode-locked case, the CDW phase is constrained to move at a fixed dc velocity relative to the pinning potential. In both pinned and mode-locked cases, the CDW and lattice degrees of freedom are nearly frozen together for low frequency excitations and the stiffness of the CDW adds to that of the lattice. In both pinned and mode-locked cases, the constraint on the CDW phase also precludes any friction at low frequencies between CDW and lattice.

Mozurkewich et al.[4] and Brill et al.[3] have demonstrated for several CDW materials that the changes in Y due to CDW depinning are of order $Y_{CDW}/Y_{Total} \approx 10^{-2}$-$10^{-3}$, where

Y_{CDW} and Y_{Total} are respectively the CDW and total crystal Young's moduli. In the calculations of Mozurkewich et. al. and Brill et. al., the phase elasticity in the Fukuyama-Lee Hamiltonian[15] (Eq. 5-2) is used to estimate the CDW elasticity, and experimentally determined values are used for the lattice elasticity. Our model predicts changes of order $k_c/(k_c+K_L) = Y_{CDW}/Y_{Total}$. This is the first dynamical model of CDW elasticity to correctly predict the magnitude of the elasticity changes.

The interaction of the CDW with the lattice is an area that requires further investigation. In our model the electronically induced mode-locking strongly couples all the internal degrees of freedom. This may have implications for other coupled systems which exhibit mode-locking. Finally, the Frenkel-Kontorova model has been applied to many condensed matter systems, notably superionic conductors, adsorbates on surfaces, and 1-D magnetism[16]. In all of these systems, the assumption of a fully rigid substrate potential is unrealistic. Our extension of the Frenkel-Kontorova model or discretized Sine-Gordon equation is thus relevant to a wide variety of systems[17].

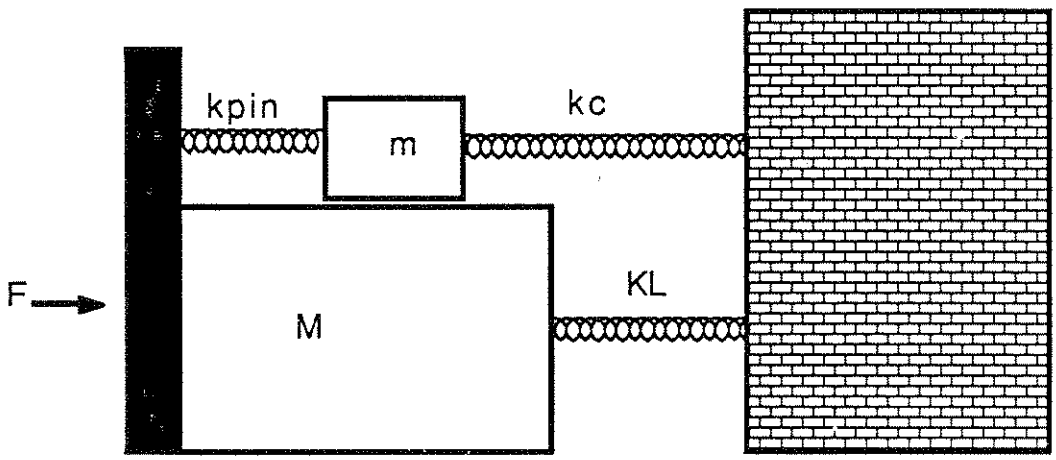

Fig. 8-4: Mechanical analog of equations 8-4 and 8-5 linearized about the $E_{dc}=0$ equilibrium. k_c and K_L are respectively the CDW and lattice spring constants, and $k_{pin}=2k_FeE_T$ represents the restoring force due to the sinusoidal potential. F is a mechanical force applied to the lattice.

References

[1] M. S. Sherwin and A. Zettl, Phys. Rev. B **32**, 5536 (1985)

[2] M. S. Sherwin and A. Zettl, Physica **23D**, 62 (1986)

[3] J. W. Brill and W. Roark, Phys. Rev. Lett. **53**, 846 (1984)

[4] G. Mozurkewich, P. M. Chaikin, W. G. Clark, and G. Grüner, Solid State Comm. **56**, 421 (1985); G. Mozurkewich, P. M. Chaikin, W. G. Clark, and G. Grüner Charge Density Waves in Solids, Gy. Hutiray and J. Solyom, eds. (Springer, New York, 1985) p. 353

[5] L. C. Bourne, M. S. Sherwin and A. Zettl, Phys. Rev. Lett. **56**, 1952 (1986); L. C. Bourne and A. Zettl, Phys. Rev. B **36**, 2626 (1987)

[6] J. Bardeen and J. R. Tucker, Charge Density Waves in Solids, Gy. Hutiray and J. Solyom, eds. (Springer, New York, 1985) p. 155; J. Bardeen, Phys. Rev. Lett. **42**, 1498 (1979)

[7] G. Grüner, A. Zawadowski and P. M. Chaikin, Phys. Rev. Lett. **46**, 511(1981)

[8] J. E. Sacco and J.B. Sokoloff, Phys. Rev. B **18**, 6549 (1985); S. Coppersmith, Phys. Rev. B **30**, 410 (1984); L. Sneddon, Phys. Rev. Lett. **52**, 65 (1984)

[9] J. Frenkel and T. Kontorova, Zh. Eksp. Theor. Fiz. **8**, 1340 (1938); J. Phys. (USSR) **1**, 137 (1939)

[10] S. N. Coppersmith and C. M. Varma, Phys. Rev. B **30**, 3566 (1984)

[11] D. S. Fisher, Phys. Rev. Lett. **50**, 1486 (1983)

[12] After completion of this work, we learned that a related model of CDW elasticity, which also considers the CDW and lattice as interacting deformable media, was independently being considered by Sneddon. Sneddon's model has been solved for applied dc electric field E_{dc} , and shows no divergence in the elastic properties at E_T in the thermodynamic limit. (See L. Sneddon, Phys. Rev. Lett. **56**, 1194 (1986))

[13] M. S. Sherwin and A. Zettl, Phys. Rev. B **32**, 5536(1985)

[14] M. S. Sherwin and A. Zettl, unpublished.

[15] H. Fukuyama and P. A. Lee, Phys. Rev. B **17**, 535 (1978)

[16] L. Pietronero and S. Strässler, Solid State Commun. **27**, 1041 (1978); P. Bak, Rep. Prog. Phys. **45**, 587 (1982); A. R. Bishop, J. Phys. A **14**, 883 (1981)

[17] Note that our discretization of the lattice and sinusoidal potential is distinctly different from introducing a deformable substrate into the Frenkel Kontorova model. The latter approach is considered by T. Munakata, J Phys. Soc. Japan **52**, 1635(1983), and T. Ishii, J. Phys. Soc. Japan,**52**, 168(1983).

Appendix A: Numerical integration of the Mattis-Bardeen equations for the temperature-dependent conductivity of a weak-coupling superconductor.

The original Bardeen-Cooper-Schrieffer (BCS) paper[1], published in 1957, discussed the thermodynamics and dc electrodynamics of weak-coupling, phonon-mediated superconductivity. In 1958, D. C. Mattis and J. Bardeen[2] developed a theory of the high-frequency electrodynamics of BCS superconductors. The most important result of MB theory is an integral expression for the finite temperature, complex frequency-dependent conductivity of a BCS superconductor. This appendix first discusses the limits of validity for MB theory. Then a method for numerically evaluating the MB integrals is discussed. The real and imaginary parts of the conductivity of a superconductor at various temperatures for frequencies below 4Δ are graphed and tabulated. Finally, a listing of the program used to evaluate the MB integrals is included.

Although MB theory is an extension of the BCS model, it is valid for a whole class of models. The BCS model was formulated assuming that phonons mediate the weak-coupling between electron pairs in a superconductor. However, the BCS results also hold assuming that non-phonon excitations mediate weak-coupling. The form of the temperature dependence of the order parameter in BCS theory (and hence in MB theory) is entirely a result of the mean field approximation. Thus the MB results are valid for any weak-coupling, pairing theory of superconductivity in the mean field approximation.

In general, the conductivity of a metal (or a superconductor) is a function of both frequency and wave-vector[3]. There are two limits in which the dependences on wave-vector become simple. If the electron mean free path in the normal state and the coherence length in the superconducting state are both very long compared to the penetration depth of the electromagnetic field (called the extreme anomalous limit, or Pippard limit) the conductivity $\sigma(q,w) \propto 1/q$ for both the superconducting and normal states. If the electron mean free path in the normal state and the coherence length in the superconducting state are both short compared with the penetration depth of the electromagnetic field (London limit),

then the q-dependence of the conductivity becomes negligible. In both the London and Pippard limits, the ratio of the conductivity in the superconducting state to the conductivity in the normal state is independent of wave-vector. MB was calculated for the Pippard limit, but the results are also valid in the London limit[4]. High-Tc superconductors have low conductivities, extremely short coherence lengths, and long electromagnetic field penetration depths, so the London limit is appropriate.

Mattis and Bardeen expressed the ratio of the superconducting to normal state conductivity in terms of the following integrals.

$$\frac{\sigma_1}{\sigma_N} = \frac{2}{h\omega}\int_{\varepsilon_0}^{\infty}[f(E)-f(E+h\omega)]g(E)dE + \frac{1}{h\omega}\int_{\varepsilon_0-h\omega}^{-\varepsilon_0}[1-2f(E+h\omega)]g(E)dE \qquad \text{(A-1)}$$

$$\frac{\sigma_2}{\sigma_N} = \frac{1}{h\omega}\int_{\varepsilon_0-h\omega;-\varepsilon_0}^{\varepsilon_0}\frac{[1-2f(E+h\omega)](E^2+\varepsilon_0^2+h\omega E)}{(\varepsilon_0^2-E^2)^{1/2}[(E+h\omega)^2-\varepsilon_0^2]^{1/2}}dE \qquad \text{(A-2)}$$

$$g(E) = \frac{(E^2+\varepsilon_0^2+h\omega E)}{\varepsilon_1\varepsilon_2} \qquad \text{(A-3)}$$

and

$$\varepsilon_1=(E^2-\varepsilon_0^2)^{1/2}, \quad \varepsilon_2=[(E+h\omega)^2-\varepsilon_0^2]^{1/2} \qquad \text{(A-4)}$$

f(E) is the Fermi function

$$f(E) = \frac{1}{1+e^{E/kT}} \qquad \text{(A-5)}$$

where E=0 is at the Fermi level. The notation is that of MB. ε_0 is the energy gap $\Delta(T)$ (NOT $2\Delta(T)$). The second term of Eq. A-1 does not appear unless $h\omega > 2\varepsilon_0$, in which

case the lower limit of the integral in Eq. A-2 is $-\varepsilon_0$ instead of $\varepsilon_0-\hbar\omega$. Signs of the square roots are such that g(E) is positive in both integrals of Eq. A-1. It is possible to express Eqs. 1 and 2 in dimensionless form if the BCS relation $\Delta(T=0) = 1.76k_BT_c$ is used.

These integrals have a closed form solution only for T=0. At finite temperature, the integrals must be performed numerically. The integrals are resistant to simple numerical integration (using, for instance, the trapezoidal rule). The upper limit of the first integral in equation 1 is infinite, and the integrand is singular at the lower limit. The integrands of the other two integrals have a square root singularities at each of their four limits of integration. There exist extremely efficient techniques for performing integrals with square root singularities at the endpoints, and we have used these. Useful discussions of numerical integration techniques are to be found in Numerical Recipes[4]. Many formulas are to be found in Abramowitz and Stegun, *Handbook of Mathematical Functions*[5], pp. 886 ff.

Eq. 1 was integrated using Gaussian quadrature. Eq. 25.4.37 in Ref. 5 enables efficient evaluation of integrals with a square root singularity at the upper boundary:

$$\int_a^b \frac{f(y)}{(b-y)^{1/2}}dy = (b-a)^{1/2}\sum_{i=1}^{n} w_i f(y_i) + R_n \qquad \text{(A-6)}$$

where

$$y_i = a + (b-a)x_i \qquad \text{(A-7)}$$

R_n is the remainder of the series summed to order n, and $x_i=1-\xi_i^2$ where ξ_i is the ith positive zero of the Legendre polynomial $P_{2n}(x)$. The weights w_i are the Gaussian weights of order 2n. The zeroes ξ_i and weights w_i are tabulated to 20 digit accuracy on pp. 916 ff. of Ref. 5. Eq. (A-1) was put into the form of Eq. (A-6) by using the identity

$$\int_a^b f(y)dy = \int_{1/b}^{1/a}\left(\frac{1}{t^2}\right)f\left(\frac{1}{t}\right)dt \qquad \text{(A-8)}$$

The utility of Eq. (A-6) comes from two sources. One is that the square root singularity at the upper limit of integration is removed. The other is that the method is computationally extremely efficient. Because of the high degree of accuracy with which the Gaussian weights and zeroes are tabulated, highly accurate evaluations of the integral are obtained with only a few terms in the series. Thus a Macintosh running a relatively slow, interpreted Basic was able to perform the computations listed in tables A-1 and A-2 in about 2 hours.

The second term of Eq. 1 and the integral in Eq. 2 both have square root singularities at both endpoints. These integrals were evaluated using Eq. 25.4.39 of Ref. 5. The formula is

$$\int_a^b \frac{f(y)}{(y-a)^{1/2}(b-y)^{1/2}}dy = \sum_{i=1}^{n} w_i f(y_i) + R_n \qquad \text{(A-9)}$$

where

$$x_i = \cos\left(\frac{2i-1}{2n}\right)\pi \qquad \text{(A-10)}$$

and $w_i=\pi/n$. R_n is the remainder of the series summed to order n.

The integration routines were all checked by performing integrals with analytic solutions, and checking the numerical results against the analytic solutions. The T = 0 result was checked by comparing it with values calculated for Prof. P. L. Richards by J. Swihart. The finite temperature results show the correct limiting behavior at high and low temperatures.

The real and imaginary parts of the conductivity σ_1/σ_N and σ_2/σ_N are graphed in Fig. A-1 and tabulated in Tables A-1 and A-2 for various values of the reduced temperature T/T_c. For a given value of the reduced temperature, the relative accuracy of values of the conductivity calculated for different frequencies (limited by computational errors) is better

than 0.5%. The absolute accuracy is difficult to gauge. It is limited by the 1% accuracy of the values used for the temperature-dependent energy gap $\Delta(T)$. Since MB theory is based on a mean field approximation, it will not be valid near the phase transition where fluctuations become important.

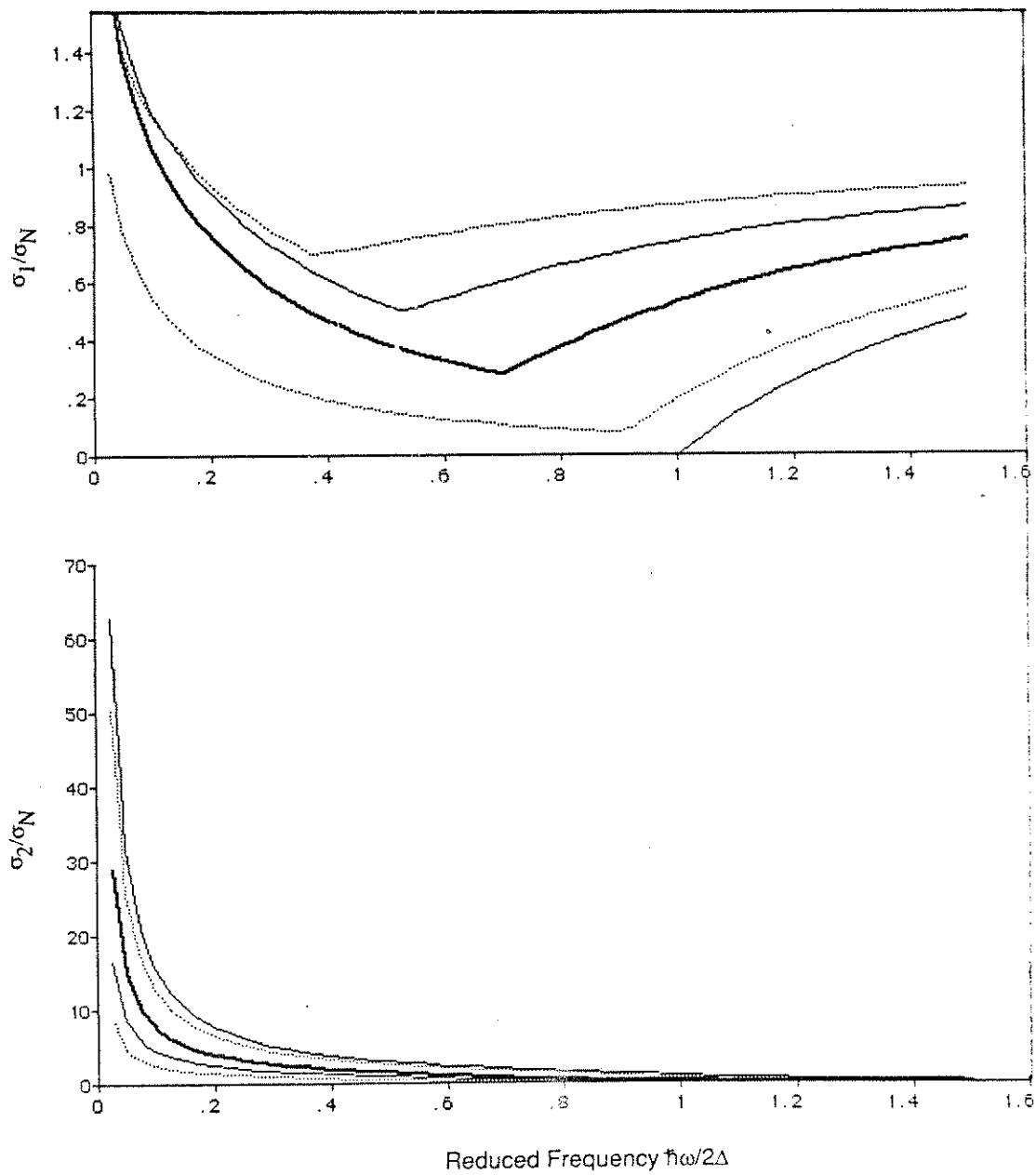

Fig. A-1: Frequency dependent conductivity of a superconductor calculated from Eqs. 1 and 2 at various temperatures. a) Real part of the conductivity σ_1/σ_N vs. reduced frequency $\omega/2\Delta$. b) Imaginary part of the conductivity σ_2/σ_N vs. reduced frequency $\omega/2\Delta$.

Table A-1: Real part of the frequency-dependent conductivity of a superconductor at selected temperatures: $\sigma_1(\omega)/\sigma_N(\omega)$

T/Tc:	0.95	0.9	0.8	0.6	0.2	0.01
Δ(T)/Δ(0):	0.38	0.53	0.7	0.91	1	1
ω/2Δ(0)						
0.025	1.6347	1.7709	1.6903	0.9885	4.595E-03	0
0.05	1.4148	1.4907	1.3793	0.7670	2.966E-03	0
0.075	1.2833	1.3250	1.1972	0.6397	2.134E-03	0
0.1	1.1877	1.2060	1.0681	0.5513	1.624E-03	0
0.125	1.1116	1.1127	0.9682	0.4846	1.283E-03	0
0.15	1.0478	1.0357	0.8870	0.4318	1.043E-03	0
0.175	0.9926	0.9700	0.8187	0.3885	8.675E-04	0
0.2	0.9437	0.9127	0.7601	0.3523	7.352E-04	0
0.225	0.8996	0.8619	0.7089	0.3215	6.330E-04	0
0.25	0.8596	0.8163	0.6637	0.2950	5.524E-04	0
0.275	0.8227	0.7750	0.6233	0.2719	4.877E-04	0
0.3	0.7887	0.7373	0.5871	0.2517	4.349E-04	0
0.325	0.7570	0.7027	0.5543	0.2338	3.913E-04	0
0.350	0.7274	0.6708	0.5244	0.2179	3.548E-04	0
0.375	0.6997	0.6413	0.4972	0.2037	3.239E-04	0
0.400	0.7011	0.6138	0.4722	0.1910	2.974E-04	0
0.425	0.7097	0.5883	0.4492	0.1795	2.746E-04	0
0.450	0.7183	0.5644	0.4280	0.1691	2.547E-04	0
0.475	0.7268	0.5421	0.4084	0.1597	2.373E-04	0
0.500	0.7354	0.5212	0.3903	0.1511	2.219E-04	0
0.525	0.7438	0.5015	0.3734	0.1433	2.082E-04	0
0.550	0.7521	0.5108	0.3577	0.1362	1.960E-04	0
0.575	0.7603	0.5270	0.3431	0.1296	1.851E-04	0
0.600	0.7683	0.5429	0.3294	0.1235	1.752E-04	0
0.625	0.7762	0.5584	0.3167	0.1179	1.662E-04	0
0.650	0.7838	0.5735	0.3047	0.1128	1.580E-04	0
0.675	0.7912	0.5882	0.2935	0.1080	1.506E-04	0
0.700	0.7984	0.6025	0.2829	0.1036	1.438E-04	0
0.725	0.8054	0.6163	0.3086	0.0994	1.375E-04	0
0.750	0.8121	0.6297	0.3334	0.0956	1.317E-04	0
0.775	0.8186	0.6426	0.3574	0.0920	1.264E-04	0
0.800	0.8248	0.6550	0.3804	0.0886	1.214E-04	0
0.825	0.8309	0.6670	0.4026	0.0855	1.168E-04	0
0.850	0.8366	0.6785	0.4239	0.0826	1.125E-04	0
0.875	0.8422	0.6896	0.4444	0.0798	1.085E-04	0
0.900	0.8475	0.7002	0.4640	0.0772	1.048E-04	0
0.925	0.8527	0.7104	0.4827	0.0970	1.013E-04	0
0.950	0.8576	0.7202	0.5007	0.1302	9.796E-05	0
0.975	0.8623	0.7295	0.5179	0.1620	9.486E-05	0
1.000	0.8668	0.7385	0.5343	0.1921	9.194E-05	0
1.025	0.8711	0.7471	0.5500	0.2209	3.816E-02	3.808E-02
1.050	0.8753	0.7553	0.5650	0.2482	7.397E-02	7.390E-02
1.075	0.8792	0.7631	0.5794	0.2742	0.1077	0.1076
1.100	0.8830	0.7707	0.5931	0.2989	0.1395	0.1395
1.125	0.8867	0.7779	0.6061	0.3224	0.1696	0.1695
1.150	0.8902	0.7848	0.6186	0.3448	0.1980	0.1980
1.175	0.8935	0.7914	0.6306	0.3661	0.2249	0.2249
1.200	0.8967	0.7977	0.6420	0.3864	0.2505	0.2504
1.225	0.8998	0.8037	0.6529	0.4057	0.2747	0.2746
1.250	0.9027	0.8095	0.6634	0.4242	0.2976	0.2976
1.275	0.9055	0.8151	0.6734	0.4417	0.3195	0.3195
1.300	0.9082	0.8204	0.6829	0.4585	0.3403	0.3403

$\sigma_1(\omega)/\sigma_N(\omega)$

T/Tc:	0.95	0.9	0.8	0.6	0.2	0.01
Δ(T)/Δ(0):	0.38	0.53	0.7	0.91	1	1
ω/2Δ(0)						
1.325	0.9108	0.8255	0.6921	0.4745	0.3601	0.3601
1.350	0.9133	0.8304	0.7008	0.4898	0.3790	0.3789
1.375	0.9157	0.8351	0.7092	0.5044	0.3970	0.3970
1.400	0.9179	0.8396	0.7173	0.5184	0.4142	0.4142
1.425	0.9201	0.8439	0.7250	0.5318	0.4306	0.4306
1.450	0.9223	0.8481	0.7324	0.5446	0.4464	0.4463
1.475	0.9243	0.8520	0.7395	0.5569	0.4614	0.4614
1.500	0.9262	0.8559	0.7463	0.5687	0.4758	0.4758
1.525	0.9281	0.8596	0.7529	0.5799	0.4896	0.4896
1.550	0.9299	0.8631	0.7591	0.5908	0.5029	0.5028
1.575	0.9317	0.8665	0.7652	0.6012	0.5156	0.5156
1.600	0.9333	0.8698	0.7710	0.6112	0.5278	0.5278
1.625	0.9349	0.8729	0.7763	0.6208	0.5395	0.5395
1.650	0.9365	0.8760	0.7820	0.6300	0.5508	0.5508
1.675	0.9380	0.8789	0.7872	0.6389	0.5616	0.5616
1.700	0.9394	0.8817	0.7922	0.6474	0.5721	0.5720
1.725	0.9408	0.8845	0.7970	0.6557	0.5821	0.5821
1.750	0.9422	0.8871	0.8017	0.6636	0.5918	0.5918
1.775	0.9435	0.8896	0.8061	0.6713	0.6011	0.6011
1.800	0.9447	0.8911	0.8105	0.6787	0.6101	0.6101
1.825	0.9459	0.8945	0.8147	0.6858	0.6188	0.6188
1.850	0.9471	0.8967	0.8187	0.6927	0.6272	0.6272
1.875	0.9482	0.8990	0.8226	0.6993	0.6353	0.6353
1.900	0.9493	0.9011	0.8264	0.7058	0.6431	0.6431
1.925	0.9504	0.9032	0.8300	0.7120	0.6507	0.6507
1.950	0.9514	0.9052	0.8336	0.7180	0.6580	0.6580
1.975	0.9524	0.9071	0.8370	0.7238	0.6651	0.6651
2.000	0.9534	0.9090	0.8403	0.7294	0.6719	0.6719

Table A-2: Imaginary part of the frequency-dependent conductivity of a superconductor at selected temperatures: $\sigma_2(\omega)/\sigma_N(\omega)$

T/Tc:	0.95	0.9	0.8	0.6	0.2	0.01
Δ(T)/Δ(0):	0.38	0.53	0.7	0.91	1	1
ω/2Δ(0)						
0.025	8.5561	16.4784	29.1349	50.2444	62.8067	62.8220
0.050	4.5105	8.5332	14.8857	25.3324	31.3899	31.3963
0.075	3.1546	5.8742	10.1205	17.0099	20.9109	20.9145
0.100	2.4699	4.5360	7.7260	12.8353	15.6663	15.6686
0.125	2.0529	3.7256	6.2797	10.3204	12.5155	12.5171
0.150	1.7689	3.1786	5.3073	8.6356	10.4116	10.4128
0.175	1.5603	2.7817	4.6056	7.4256	8.9059	8.9069
0.200	1.3982	2.4784	4.0731	6.5124	7.7741	7.7748
0.225	1.2665	2.2372	3.6533	5.7973	6.8915	6.8921
0.250	1.1553	2.0392	3.3125	5.2210	6.1833	6.1838
0.275	1.0584	1.8724	3.0290	4.7459	5.6020	5.6024
0.300	0.9714	1.7288	2.7885	4.3466	5.1158	5.1161
0.325	0.8905	1.6028	2.5811	4.0058	4.7026	4.7029
0.350	0.8124	1.4903	2.3996	3.7109	4.3469	4.3472
0.375	0.7302	1.3884	2.2387	3.4529	4.0372	4.0374
0.400	0.6430	1.2946	2.0946	3.2248	3.7646	3.7649
0.425	0.5800	1.2071	1.9643	3.0214	3.5228	3.5230
0.450	0.5274	1.1240	1.8453	2.8385	3.3064	3.3066
0.475	0.4821	1.0438	1.7357	2.6729	3.1115	3.1117
0.500	0.4424	0.9638	1.6340	2.5220	2.9348	2.9349
0.525	0.4072	0.8781	1.5388	2.3837	2.7736	2.7737
0.550	0.3759	0.7863	1.4490	2.2562	2.6258	2.6259
0.575	0.3478	0.7183	1.3636	2.1379	2.4895	2.4896
0.600	0.3225	0.6605	1.2816	2.0278	2.3634	2.3635
0.625	0.2996	0.6099	1.2019	1.9247	2.2460	2.2461
0.650	0.2788	0.5653	1.1231	1.8278	2.1364	2.1364
0.675	0.2600	0.5247	1.0428	1.7362	2.0335	2.0336
0.700	0.2428	0.4885	0.9511	1.6492	1.9366	1.9367
0.725	0.2272	0.4557	0.8643	1.5662	1.8449	1.8450
0.750	0.2128	0.4259	0.7973	1.4865	1.7579	1.7580
0.775	0.1997	0.3987	0.7397	1.4096	1.6749	1.6749
0.800	0.1876	0.3739	0.6887	1.3348	1.5954	1.5954
0.825	0.1766	0.3512	0.6432	1.2613	1.5189	1.5189
0.850	0.1664	0.3304	0.6022	1.1882	1.4448	1.4448
0.875	0.1570	0.3113	0.5650	1.1137	1.3727	1.3727
0.900	0.1483	0.2937	0.5312	1.0336	1.3019	1.3019
0.925	0.1402	0.2775	0.5003	0.9402	1.2316	1.2316
0.950	0.1328	0.2625	0.4720	0.8747	1.1607	1.1607
0.975	0.1259	0.2486	0.4460	0.8132	1.0869	1.0870
1.000	0.1196	0.2358	0.4220	0.7625	0.9999	0.9999
1.025	0.1136	0.2239	0.4000	0.7174	0.9178	0.9178
1.050	0.1081	0.2129	0.3796	0.6768	0.8561	0.8561
1.075	0.1030	0.2026	0.3607	0.6399	0.8036	0.8036
1.100	9.815E-02	0.1930	0.3432	0.6063	0.7573	0.7573
1.125	9.367E-02	0.1841	0.3269	0.5754	0.7160	0.7160
1.150	8.949E-02	0.1758	0.3118	0.5471	0.6786	0.6786
1.175	8.557E-02	0.1680	0.2977	0.5209	0.6445	0.6445
1.200	8.190E-02	0.1607	0.2845	0.4967	0.6133	0.6133
1.225	7.845E-02	0.1539	0.2722	0.4743	0.5846	0.5846
1.250	7.522E-02	0.1475	0.2607	0.4534	0.5580	0.5580
1.275	7.218E-02	0.1415	0.2499	0.4339	0.5334	0.5334
1.300	6.932E-02	0.1358	0.2398	0.4157	0.5105	0.5105

$\sigma_2(\omega)/\sigma_N(\omega)$

T/Tc:	0.95	0.9	0.8	0.6	0.2	0.01
Δ(T)/Δ(0):	0.38	0.53	0.7	0.91	1	1
ω/2Δ(0)						
1.325	6.663E-02	0.1305	0.2303	0.3987	0.4892	0.4892
1.350	6.409E-02	0.1255	0.2213	0.3828	0.4693	0.4693
1.375	6.169E-02	0.1208	0.2129	0.3678	0.4506	0.4506
1.400	5.942E-02	0.1163	0.2050	0.3538	0.4331	0.4331
1.425	5.728E-02	0.1121	0.1975	0.3405	0.4166	0.4166
1.450	5.525E-02	0.1081	0.1904	0.3280	0.4011	0.4011
1.475	5.333E-02	0.1043	0.1836	0.3162	0.3865	0.3865
1.500	5.151E-02	0.1007	0.1773	0.3051	0.3727	0.3727
1.525	4.978E-02	9.735E-02	0.1713	0.2946	0.3597	0.3597
1.550	4.814E-02	9.412E-02	0.1655	0.2846	0.3474	0.3474
1.575	4.657E-02	9.106E-02	0.1601	0.2751	0.3357	0.3357
1.600	4.509E-02	8.814E-02	0.1550	0.2661	0.3246	0.3246
1.625	4.367E-02	8.536E-02	0.1500	0.2575	0.3140	0.3140
1.650	4.232E-02	8.271E-02	0.1454	0.2494	0.3040	0.3040
1.675	4.104E-02	8.019E-02	0.1409	0.2417	0.2945	0.2945
1.700	3.981E-02	7.778E-02	0.1367	0.2343	0.2854	0.2854
1.725	3.863E-02	7.548E-02	0.1326	0.2272	0.2767	0.2767
1.750	3.751E-02	7.329E-02	0.1287	0.2205	0.2685	0.2685
1.775	3.644E-02	7.118E-02	0.1250	0.2141	0.2606	0.2606
1.800	3.541E-02	6.917E-02	0.1215	0.2079	0.2531	0.2531
1.825	3.443E-02	6.725E-02	0.1181	0.2021	0.2459	0.2459
1.850	3.349E-02	6.540E-02	0.1148	0.1964	0.2390	0.2390
1.875	3.258E-02	6.363E-02	0.1117	0.1910	0.2323	0.2323
1.900	3.172E-02	6.193E-02	0.1087	0.1859	0.2260	0.2260
1.925	3.089E-02	6.031E-02	0.1058	0.1809	0.2199	0.2199
1.950	3.009E-02	5.874E-02	0.1031	0.1762	0.2141	0.2141
1.975	2.932E-02	5.724E-02	0.1004	0.1716	0.2085	0.2085
2.000	2.858E-02	5.579E-02	0.0979	0.1672	0.2031	0.2031

Computer program

This program calculates the real and imaginary parts of the temperature dependent conductivity of a weak-coupling superconductor. The program is written in Microsoft Basic and runs on a Macintosh computer. The program integrates the formulas derived by D. C. Mattis and J. Bardeen (formulas 3.9 and 3.10, Phys. Rev. 111, p. 412 (1958)) There are four subroutines and a driver. Each subroutine calculates one term of Eqs. 3.9 and 3.10.

DRIVER PROGRAM

```
DIM TARRAY(6),DEL(6)
```

The reduced temperature T/Tc is stored in the array TARRAY.The reduced gap Δ(T)/Δ(T=0) is stored in the array DEL. Δ(T) was determined to within 1% from the graph of Δ(T) vs. T in Kittel's ISSP, p. 367.

```
TARRAY(1)=.95:TARRAY(2)=.9:TARRAY(3)=.8:TARRAY(4)=.6:
TARRAY(5)=.2: TARRAY(6)=.01
DEL(1)=.38:DEL(2)=.53:DEL(3)=.7:DEL(4)=.91:DEL(5)=1:DEL(6)=1
FOR NUM=1 TO 6
T=TARRAY(NUM)
E0=DEL(NUM)
LPRINT "REDUCED TEMPERATURE",T
LPRINT"REDUCED GAP",E0
```

```
LPRINT "Freq.","SIG1/SIGN","SIG2/SIGN"
```

SIG1 is the real part of the conductivity in the superconducting state.SIG2 is the imaginary part of the conductivity in the superconducting state. SIGN is the real part of the frequency dependent conductivity in the normal state HW is the energy divided by the energy gap DEL (not 2DEL)

```
FOR HW=.05 TO 4 STEP .05

  S11=0: S12=0: S2=0
  IF HW<2*E0 THEN CALL MATBA3(S2,E0,HW,T) ELSE CALL
MATBA4(S2,E0,HW,T)
  CALL MATBA1(S11,E0,HW,T)
  IF HW>2*E0 THEN CALL MATBA2(S12,E0,HW,T)
  LPRINT .5*HW,(2*S11+S12)/HW,S2/HW
NEXT HW
NEXT NUM
END
```

SUBROUTINES

```
SUB MATBA1(S,E0,HW,T) STATIC
```

This subroutine computes the first integral in formula 3.9 of Mattis-Bardeen. The upper bound of this integral is infinite. In order to handle this

with Gaussian quadrature, it is necessary to change variables. The identity:integral from a to b of f(x)= integral from 1/b to 1/a of ((1/t^2)f(1/t))was used. (See William H. Press, Brian P. Flannery, Saul A. Teukolsky and William Vetterling, Numerical Recipes, p. 118).

```
A=E0
S=1E+20
ST=1E-20
FOR B=100*T TO 500*T STEP 50*T
```

This loop calls the integrating routine SQRT1. The upper limit (infinite in the formula of Mattis and Bardeen) is increased with each subroutine call until the difference between the evaluation of the integral on successive calls is less than 0.01%, or until the upper limit reaches 500 times the reduced temperature (reduced temperature and energy gap are related by the BCS relation $\Delta(0)=1.76\ k_B T_C$)

```
  CALL SQRT1(A,B,S,E0,HW,T)
  IF ABS(S-ST)<.0001*ABS(S) THEN GOTO 10
  ST=S
  NEXT B
10 END SUB

SUB SQRT1(AA,BB,S,E0,HW,T) STATIC
```

This subroutine integrates a function with a square root singularity at its upper endpoint by formula 25.4.37 of Abramowitz and Stegun with n=10. The data statement is a tabulation of the 10 positive zeroes and weights (the zeroes and weights alternate) of a n=20 Legendre polynomial (Ibid, p. 916).

```
DATA 7.65265211D-02, .1527533871#, .2277858511#, .1491729864#,
.3737060887#, .1420961093#, .5108670019#, .1316886384#,
.6360536807#, .1181945319#
DATA .7463319064#, .1019301198, .8391169718#, .0832767415,
.9122344282#, .0626720483, .9639719272#, .0406014298, .9931285991#,
.0176140071
    RESTORE
    B=1/AA
    A=1/BB
    S=0
    FOR I=1 TO 10
      READ XI
      READ WI
      X=1-XI^2
      W=2*WI
      Y=A+(B-A)*X
      F=SQR(B*Y)*(1/Y^2)*(1/(EXP(1.76/(T*Y))+1)-
1/(EXP(1.76*(1/Y+HW)/T)+1))*(1/Y^2+E0^2+HW/Y)/(ABS((1/Y+E0)*((1/
Y+HW)^2-E0^2)))^.5
      S=S+(B-A)^.5*W*F
    NEXT I
  END SUB
```

```
SUB MATBA2(S,E0,HW,T) STATIC
```

This subroutine computes the second integral of formula 3.9 of Mattis and Bardeen's paper.

S returns the value of the integral.

```
A=E0-HW
B=-1*E0
NMAX=10
S=1E+20
ST=-1E+20
FOR N=1 TO NMAX
  CALL DBLSQ2(A,B,S,N,T,HW,E0)
  IF ABS(S-ST)<(.0001)*ABS(S) THEN GOTO 20
  ST=S
  NEXT N
20 END SUB
```

```
SUB DBLSQ2(A,B,S,N,T,HW,E0) STATIC
```

This subroutine integrates a function with a square root singularity at both the lower and upper bounds, as described in Abramowitz and Stegun, p. 889, formula 25.4.39

int(f(y)/sqrt((y-a)(b-y))dy)=sum(wi*f(yi))*

```
S=0
  FOR I=1 TO N
  YI=(B+A)/2+((B-A)/2)*COS((2*I-1)*3.14159265#/(2*N))
    S=S + (3.141593/N) * (1-2*(1/(EXP(1.76*(YI+HW)/T)+1)))
*ABS(YI^2+E0^2+HW*YI)/(ABS((YI-E0)*(YI+HW+E0)))^.5
  NEXT I
 END SUB
```

```
SUB MATBA3(S,E0,HW,T) STATIC
```

This subroutine computes the integral of formula 3.10 of Mattis and Bardeen's paper for hw<2E0.(frequency<Δ(T)). S returns the value of the integral.

```
A=E0-HW
B=E0
NMAX=10
S=1E+20
ST=-1E+20
FOR N=1 TO NMAX
```

This loop calls the integrating subroutine. The order of the integration routine is increased until successive calculations of the integral are closer than 0.01%, or until NMAX iterations are performed

```
CALL DBLSQ3(A,B,S,N,T,HW,E0)
```

```
    IF ABS(S-ST)<(.0001)*ABS(S) THEN GOTO 30
    ST=S
    NEXT N
30 END SUB


SUB DBLSQ3(A,B,S,N,T,HW,E0) STATIC
    S=0
```

This subroutine integrates a function with a square root singularity at both the lower and upper bounds, as described in Abramowitz and Stegun, p. 889, formula 25.4.39

int(f(y)/sqrt((y-a)(b-y))dy)=sum(wi*f(yi))*

```
      FOR I=1 TO N
       YI=(B+A)/2+((B-A)/2)*COS((2*I-1)*3.14159265#/(2*N))
         S=S + (3.141593/N) * (1-2*(1/(EXP(1.76*(YI+HW)/T)+1)))
*(YI^2+E0^2+HW*YI)/(ABS((YI+E0)*(YI+HW+E0)))^.5
      NEXT I
    END SUB


SUB MATBA4(S,E0,HW,T) STATIC
```

This subroutine computes the integral of formula 3.10 of Mattis and Bardeen's paper for hw>2E0.(frequency>2Δ) S returns the value of the integral.

```
A=-1*E0
B=E0
NMAX=10
S=1E+20
ST=-1E+20
FOR N=1 TO NMAX
  CALL DBLSQ4(A,B,S,N,T,HW,E0)
  IF ABS(S-ST)<(.0001)*ABS(S) THEN GOTO 40
  ST=S
  NEXT N
40  END SUB

SUB DBLSQ4(A,B,S,N,T,HW,E0) STATIC
```

This subroutine integrates a function with a square root singularity at both the lower and upper bounds, as described in Abramowitz and Stegun, p. 889, formula 25.4.39

int(f(y)/sqrt((y-a)(b-y))dy)=sum(wi*f(yi))*

```
  S=0
    FOR I=1 TO N
    YI=(B+A)/2+((B-A)/2)*COS((2*I-1)*3.14159265#/(2*N))
        S=S + (3.141593/N)* (1-2*(1/(EXP(1.76*(YI+HW)/T)+1)))
*(YI^2+E0^2+HW*YI)/(ABS((YI+HW)^2-E0^2))^.5
    NEXT I
  END SUB
```

References

[1] J. Bardeen, L. N. Cooper and J. R. Schrieffer, Phys. Rev. **108**, 1175 (1957)

[2] D. C. Mattis and J. Bardeen, Phys. Rev. **111**, 412 (1958)

[3] A. B. Pippard, in Advances in Electronics, edited by L. Marton (Academic Press, Inc., New York, 1954), Vol. 6, p. 1

[4] W. H. Press, B. P. Flannery, S. A. Teukolsky and W. T. Vetterling, Numerical Recipes, Cambridge University Press, Cambridge, MA (1986)

[5] M. Abramowitz and I. Stegun, *Handbook of Mathematical Functions*, National Bureau of Standards (U. S.) Applied Mathematics series No. 55 (U.S. GPO, Washington, DC, 1970), formulas 25.4.37 and 25.4.39.

Appendix B: Analog simulations of and analytic approximations to a model of charge-density-wave elasticity

B-1. Analog simulator

We constructed an electronic circuit which has equations of motion isomorphic to Eqs. 8-4 and 8-5. The circuit diagram is shown in Fig. B-1. At the heart of this analog simulator is a circuit that simulates a Josephson Junction (the x in the circuit diagram, a Walker-Gillette Model JA-100). The details of the operation of this kind of Josephson Junction analog simulator are to be found in the Ph. D thesis of Dr. Qing Hu (Harvard, 1986). For our purposes, the JA-100 is a black box which is a perfect analog for a Josephson weak link. The voltage between the two terminals of the JA-100 is given by the equation

$$V = \beta \frac{d(\phi_1 - \phi_2)}{dt} \tag{B-1}$$

The current through the JA-100 is

$$i_{JJ} = i_c \sin(\phi_1 - \phi_2) \tag{B-2}$$

In the language of Josephson Junctions, ϕ_1 and ϕ_2 are the phases of the superconducting wavefunctions on either side of a weak link and i_c is the critical current (variable, <1 mA, in the JA-100). V is the voltage across the JA-100, and β is the proportionality factor relating V to the time derivative of the superconducting phase difference ($1/2\pi\beta = 10^4$Hz/V in the JA-100).

The equations of motion for the circuit pictured in Fig. B-1 are determined by applying Kirchoff's laws. Since the JA-100 is designed to be operated current-biased, the entire circuit is current-biased.

$$i_1 = i_{C1} + i_{R1} + i_{L1} + i_{R2} + i_{JJ} \tag{B-3}$$

$$i_2 = i_{C2} + i_{L2} - i_{R2} - i_{JJ} \tag{B-4}$$

$$i_{L2} = i_{C3} \tag{B-5}$$

i_1 and i_2 are the currents supplied by current sources 1 and 2, and the other currents in eqs. B-3 to B-5 are the currents flowing through the components identified by their subscripts. Expressing the currents flowing through the components in terms of the phase difference across the Josephson Junction simulator (using eqs. B-1 and B-2), we find the following equations of motion:

$$\frac{1}{\beta} i_F \cos(\omega_r t) = C_1 \frac{d\phi_1}{dt^2} + \frac{1}{R_1} \frac{d\phi_1}{dt} + \frac{1}{L_1}\phi_1 + \frac{1}{R_2} \frac{d(\phi_1-\phi_2)}{dt} + \frac{i_c}{\beta}\sin(\phi_1-\phi_2) \tag{B-6}$$

$$\frac{1}{\beta}(i_{dc}+i_{ac}\cos(\omega t)) = C_2 \frac{d^2\phi_2}{dt^2} + \frac{1}{R_2} \frac{d(\phi_2-\phi_1)}{dt} + \frac{1}{L_2}(\phi_2-\phi_3) + \frac{i_c}{\beta}\sin(\phi_2-\phi_1) \tag{B-7}$$

$$\frac{1}{L_2}(\phi_2-\phi_3) = C_3 \frac{d^2\phi_3}{dt^2} \tag{B-8}$$

The components are all defined in Fig. B-1. Eq. B-6 is isomorphic to the lattice equation Eq. 8-5, and B-7 is isomorphic to the CDW equation 8-4. The correspondences between electrical and mechanical components, and the values of the components used in the simulations described in Chapter 8, are listed in Table B-1.

Eq. (B-8) does not appear explicitly in chapter 8. The role of the very large capacitor C_3 is to act as a high pass filter (the heavy wall in fig. 8-1 that moves at the velocity of the CDW center of mass) and thus enforce the boundary condition that the spring k_C (L_2 in the simulator) responds only to ac excitations. The ratio of the impedance of the inductor L_2 to the impedance of the capacitor C_3 goes as $(14\ \text{Hz}/f)^2$, where f is the excitation frequency. The mechanical resonant frequency ω_r in our simulation was roughly 200 Hz. C_3 exerted a negligible influence at this frequency. However, at frequencies much less than 14 Hz, the

impedance of C_3 dominated. The spring k_c (L_2) was not stretched, allowing the CDW to slide.

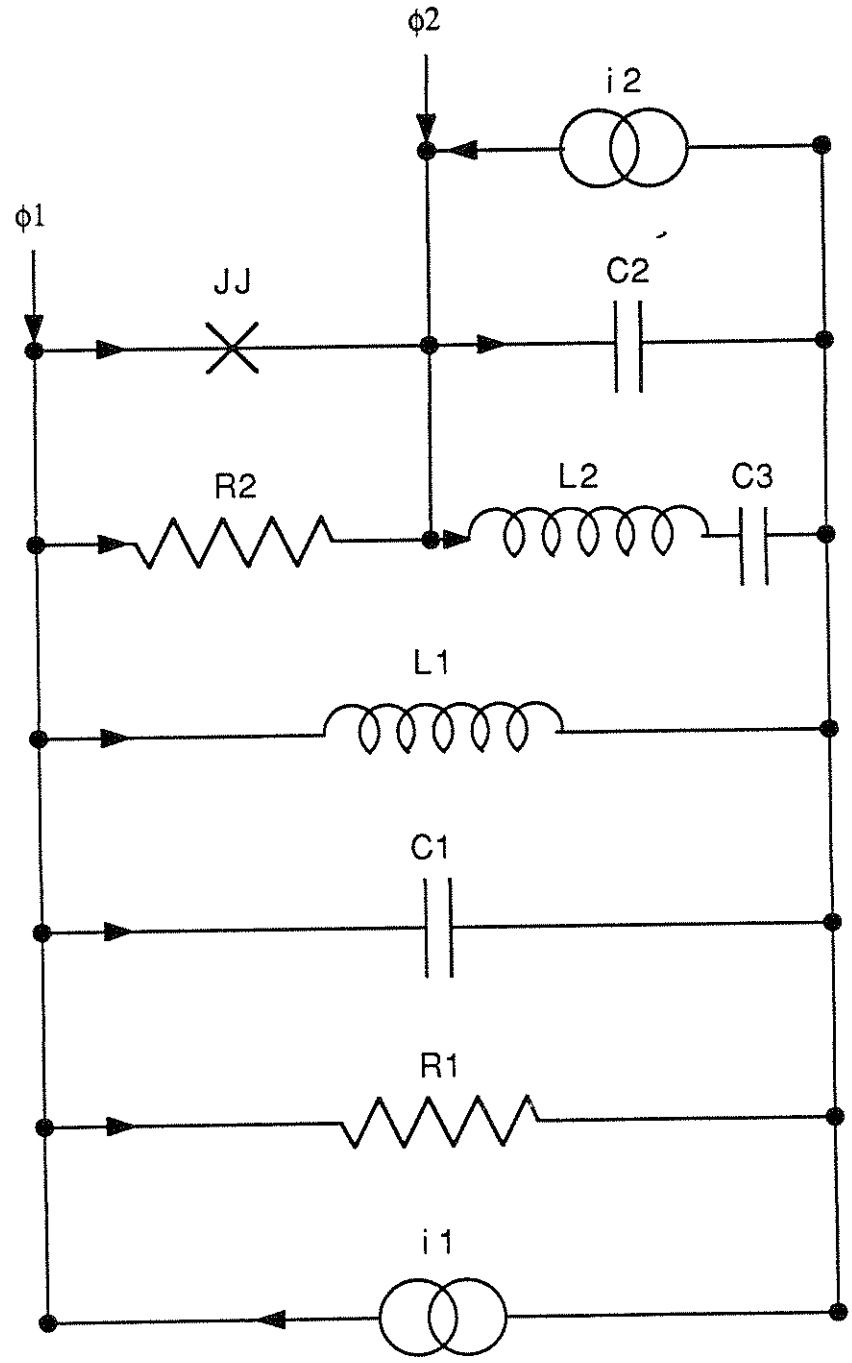

Fig. B-1: Circuit diagram of the analog computer used to model Equations 8-4 and 8-5. The values of the components and the corresponding constants from the CDW equations are listed in Table B-1

B-2. Analytic calculation of K_{eff} in the $E_{dc}>>E_T$ limit

To determine the elastic constants in the high field limit ($E_{dc}>>E_T$, $E_{ac}=0$), we linearize the equations of motion about a state of rapid dc velocity. We will show that the sinusoidal coupling between the CDW and the lattice averages to zero for a rapidly moving CDW. For this calculation, we make the common approximation that the CDW is massless. The equation of motion for the CDW is then

$$eE_{dc} = \gamma\frac{d(r-x)}{dt} + k_c(r - v_{com}t) + eE_T\sin(2k_F(r-x)) \qquad \text{(B-10)}$$

where v_{com} is the dc velocity of the CDW center of mass. For $E_{dc}>>E_T$, the terms eE_{dc} and $\gamma\frac{dr}{dt}$ dominate. The other terms may be treated as perturbations. The solution to the unperturbed equation is then

$$\frac{dr_0}{dt} = \frac{eE_{dc}}{\gamma} = v_{com} \qquad \text{(B-11)}$$

where r_0 is the unperturbed CDW position.

There is a natural separation of time scales in this problem. The period of a narrow band noise oscillation (λ_{CDW}/v_{com})is much faster than the period of the mechanical resonance ($2\pi/\omega_r$). Thus, in order to determine the effective spring constant felt by a mechanical force acting on the system at frequency ω_r, we may average the equations over the fast time scale. We define dimensionless variables $\rho = 2k_Fr$ and $\xi = 2k_Fx$. We then separate the variables ρ and ξ into fast and slow components as follows:

$$\rho(t) = \rho_0 + \rho_{slow}(t) + \rho_{fast}(t) \qquad \text{(B-12)}$$

$$\xi(t) = \xi_{slow}(t) + \xi_{fast}(t) \qquad \text{(B-13)}$$

where ρ_{slow} and ξ_{slow} vary on the time scale of the mechanical resonance and ρ_{fast} and ξ_{fast} vary on the time scale of the narrow band noise frequency. In terms of these fast and slow variables, the equation of motion for the lattice is

$$L(\xi,\rho)+F_T'\sin(\xi_{slow}+\xi_{fast}-\omega_{nbn}t-\rho_{slow}-\rho_{fast}) = F'\cos(\omega_r t) \tag{B-14}$$

where $F_T' = eE_T/2k_F$, $F' = eE/2k_F$, $\omega_{nbn}=2k_F v_{com}$ is the narrow band noise frequency, and $L(\xi,\rho)$ represents the linear part of the equation,

$$L(\xi,\rho) = M\frac{d^2\xi}{dt^2}+\Gamma_L\frac{d\xi}{dt}+\gamma_C\frac{d(\xi-\rho)}{dt}+K_L\xi \tag{B-15}$$

We now concentrate on the nonlinear term in Eq. B-14 and show that it averages to zero in the limit of infinite E_{dc}. The forces acting on the variable ξ are due to the small applied mechanical force $F'\cos(\omega_r t)$ and the small amplitude oscillations of ρ as it slides through the sinusoidal pinning potential. Thus it is safe to assume that ξ is small and go only to linear order in ξ. The variable ρ_{slow} is parametrically excited by the already small ξ_{slow}, so we may neglect ρ_{slow} altogether if we are only carrying out the calculation to first order in ξ_{slow}. Expanding to linear order in ξ, the nonlinear term in Eq. B-14 is

$$-F_T'\sin(\rho_{fast}+\omega_{nbn}t) + F_T'(\xi_{fast}+\xi_{slow})\cos(\omega_{nbn}t+\rho_{fast}) \tag{B-16}$$

We now assume the following form for ρ_{fast} and ξ_{fast}:

$$\rho_{fast} = A_C\cos(\omega_{nbn}t+\theta_C) \tag{B-17}$$

$$\xi_{fast} = A_L\cos(\omega_{nbn}t+\theta_L) \tag{B-18}$$

ρ_{fast} and ξ_{fast} oscillate with frequency ω_{nbn}, the washboard frequency. We assume that higher harmonics of the oscillation frequency are unimportant (reasonable for a high-field

limit calculation). A_L and A_C are the amplitudes of the oscillations, and θ_L and θ_C are the phases. Without loss of generality, we may set θ_C=0 (we are free to choose the point t=0).

The equation of motion for the lattice may now be written

$$L(\xi_{slow}) + F_T' \xi_{slow} \cos(\omega_{nbn}t + \rho_{fast}) = F' \cos(\omega_r t) +$$

$$L(\xi_{fast},\rho_{fast}) - F_T' \sin(\rho_{fast} + \omega_{nbn}t) + F_T' \xi_{fast} \cos(\omega_{nbn}t + \rho_{fast}) \qquad \text{(B-19)}$$

All the terms on the right hand side now appear as driving terms for the linearized differential equation for ξ_{slow}. Only the terms on the left hand side determine the effective spring constant. Expanding the sinusoidal term on the LHS of B-19,

$$\cos(\omega_{nbn}t + A_C\cos(\omega_{nbn}t)) = \cos(\omega_{nbn}t)\cos(A_C\cos(\omega_{nbn}t)) -$$

$$\sin(\omega_{nbn}t)\sin(A_C\cos(\omega_{nbn}t)) \approx \cos(\omega_{nbn}t) - A_C\sin(\omega_{nbn}t)\cos(\omega_{nbn}t) \qquad \text{(B-20)}$$

We now perform the average over the fast time scale and Poof! It all goes to zero. We are left with the equation for the slow variable

$$M\frac{d^2\xi}{dt^2} + \Gamma\frac{d\xi_{slow}}{dt} + K_L\xi_{slow} = F'\cos(\omega_r t) \qquad \text{(B-21)}$$

As advertised, the effective spring constant goes to K_L and the effect of the sinusoidal potential averages to zero.

CDW	Simulator	Value (in simulator)
x	ϕ_1	variable
r	ϕ_2	variable
v_{comt}	ϕ_3	variable
F	i_F/β	small
ω_r	ω_r	≈200 Hz
ω	ω	5 KHz
eE_{ac}	i_{ac}/β	$3i_C;0$
eE_{dc}	i_{dc}/β	varied
eE_T	i_C	0.76 mA
$2k_F$	$1/\beta$	$2\pi\times10^4$ Hz/V
K_L	$1/L_1$	29.4 Henry^{-1}
k_c	$1/L_2$	2.85 Henry^{-1}
M	C_1	20 μF
m	C_2	40 pF
γ_L	$1/R_1$	10^{-3} mho
γ_c	$1/R_2$	0.95×10^{-3} mho
	C_3	4000 μF

Table B-1: Correspondence between components in the electronic analog computer and constants in Equations 8-4 and 8-5. The values of the components used in the simulation are listed in the third column.